



HAL
open science

Multiscale methods in signal processing for adaptive optics

Suman Kumar Maji

► **To cite this version:**

Suman Kumar Maji. Multiscale methods in signal processing for adaptive optics. Other [cs.OH]. Université Sciences et Technologies - Bordeaux I, 2013. English. NNT : 2013BOR14912 . tel-00909085v2

HAL Id: tel-00909085

<https://theses.hal.science/tel-00909085v2>

Submitted on 1 Jul 2014

HAL is a multi-disciplinary open access archive for the deposit and dissemination of scientific research documents, whether they are published or not. The documents may come from teaching and research institutions in France or abroad, or from public or private research centers.

L'archive ouverte pluridisciplinaire **HAL**, est destinée au dépôt et à la diffusion de documents scientifiques de niveau recherche, publiés ou non, émanant des établissements d'enseignement et de recherche français ou étrangers, des laboratoires publics ou privés.

Université Bordeaux 1

THÈSE

pour obtenir le titre de DOCTEUR EN SCIENCES
de l'Université de Bordeaux 1
Spécialité : Informatique

MULTISCALE METHODS IN SIGNAL PROCESSING FOR ADAPTIVE OPTICS

Présentée et soutenue par

Suman Kumar Maji

Équipe GEOSTAT

INRIA Bordeaux Sud-Ouest

École Doctorale Mathématiques et Informatique

Université Bordeaux 1, Sciences et Technologies

Soutenue le 14 Novembre 2013

Devant le jury composé de:

Directeur de thèse	M. Hussein YAHIA	Chargé de recherche (HDR)	GEOSTAT, INRIA Bordeaux
Rapporteur	Mme Sylvie ROQUES	Directeur de recherche	IRAP-OMP, Toulouse
Rapporteur	M. Albert BJAOUI	Astronome émérite	Observatoire de la Côte d'Azur
Examineur	M. Richard G. BARANIUK	Professeur	ECE Dept., Rice University
Examineur	M. Xavier GRANIER	Professeur	Institut d'Optique, Paristech
Examineur	M. Antonio TURIEL	Directeur de recherche	ICM-CSIC, Barcelona
Examineur	M. Thierry FUSCO	Maitre de Recherche	DOTA, ONERA

RÉSUMÉ

Dans cette thèse nous introduisons une approche nouvelle pour la reconstruction d'un front d'ondes en Optique Adaptative (OA), à partir des données de gradients à basse résolution en provenance de l'analyseur de front d'ondes, et en utilisant une approche non-linéaire issue du Formalisme Multiéchelles Microcanonique (FMM). Le FMM est issu de concepts établis en physique statistique, il est naturellement approprié à l'étude des propriétés multiéchelles des signaux naturels complexes, principalement grâce à l'estimation numérique précise des exposants critiques localisés géométriquement, appelés exposants de singularité. Ces exposants quantifient le degré de prédictabilité localement en chaque point du domaine du signal, et ils renseignent sur la dynamique du système associé. Nous montrons qu'une analyse multirésolution opérée sur les exposants de singularité d'une phase turbulente haute résolution (obtenus par modèle ou à partir des données) permet de propager, le long des échelles, les gradients en basse résolution issus de l'analyseur du front d'ondes jusqu'à une résolution plus élevée. Nous comparons nos résultats à ceux obtenus par les approches linéaires, ce qui nous permet de proposer une approche novatrice à la reconstruction de fronts d'onde en Optique Adaptative.

ABSTRACT

In this thesis, we introduce a new approach to wavefront phase reconstruction in Adaptive Optics (AO) from the low-resolution gradient measurements provided by a wavefront sensor, using a non-linear approach derived from the Microcanonical Multiscale Formalism (MMF). MMF comes from established concepts in statistical physics, it is naturally suited to the study of multiscale properties of complex natural signals, mainly due to the precise numerical estimate of geometrically localized critical exponents, called the singularity exponents. These exponents quantify the degree of predictability, locally, at each point of the signal domain, and they provide information on the dynamics of the associated system. We show that multiresolution analysis carried out on the singularity exponents of a high-resolution turbulent phase (obtained by model or from data) allows a propagation along the scales of the gradients in low-resolution (obtained from the wavefront sensor), to a higher resolution. We compare our results with those obtained by linear approaches, which allows us to offer an innovative approach to wavefront phase reconstruction in Adaptive Optics.

Résumé substantiel en français

Dans cette thèse, nous présentons une approche nouvelle pour la reconstruction de la phase d'un front d'onde en optique adaptative (AO) en nous plaçant dans le cadre du Formalisme Multi-échelles Micro-canonique (FMM). Les idées fondamentales de ce formalisme sont introduites ainsi que ses applications notamment au cas du traitement du signal image, et nous l'utilisons avec succès dans le cadre d'une analyse multi-résolution associée aux ondelettes pour résoudre le problème de l'estimation de la phase turbulente pour l'AO. L'idée réside dans l'utilisation d'une ondelette permettant une inférence optimale le long des échelles d'un signal complexe dans l'analyse multi-résolution. La détermination effective d'une ondelette optimale restant pour l'instant hors de portée dans un cadre temps-réel, nous nous sommes limités à travailler uniquement avec une version approximative de l'ondelette optimale. Cette limitation nous a conduit à définir dans cette thèse une technique alternative pour l'inférence optimale le long des échelles. Nous avons montré que les exposants de singularité associés à l'acquisition d'une phase turbulente sont des candidats idéaux pour inférer des informations entre les échelles d'un signal et peuvent être utilisés dans une approche d'analyse multi-résolution (associée à une transformation en ondelettes) pour reconstruire une phase turbulente en partant des gradients à basse résolution. La justification de cette idée, qui forme le cœur de cette thèse, a été faite en deux étapes.

Dans la première étape, nous concluons qu'un signal complexe est bien décrit par l'arrangement géométrique de sa structure multi-échelle et que certaines de ses propriétés fines sont reliées aux propriétés de cascade multiplicative de certaines grandeurs physiques. Les transitions dans ces signaux peuvent être bien définies par un sous-ensemble de points qui sont liés à la notion de bord dans des images naturelles. En effet les bords sont généralement considérés comme des caractéristiques multi-échelles importantes dans un signal (des images dans notre cas) et notre objectif préliminaire a été de proposer une meilleure caractérisation des bords dans des signaux complexes et de montrer que ceux-ci peuvent se déduire de sa hiérarchie géométrique multi-échelle. En Physique Statistique on sait que les systèmes ayant des transitions d'ordre > 1 montrent des variables thermodynamiques qui ont une loi de puissance au voisinage d'un point critique. Les exposants de ces lois de puissance, quand on sait les déterminer correctement, renferment des informations clés sur un système complexe. Le FMM propose une approche adaptée à la détermination de ces exposants critiques, appelés exposants de singularité, avec pour conséquence des algorithmes améliorés pour la détermination précise des caractéristiques multi-échelles dans les signaux réels. En particulier, les exposants de singularité donnent accès à un sous-ensemble de points, appelé variété la plus singulière (VPS) dont la structure est reliée aux bords et aux contours dans les images naturelles. Nous concluons que ce sous-ensemble de points permet de définir de bien meilleurs candidats pour caractériser les transitions dans des signaux complexes : en particulier ils surpassent les approches classiques associées aux meilleurs détecteurs de bord en filtrage linéaire notamment en termes de cohérence entre les échelles. Les bords détectés par analyse de singularité sont capables de conserver leur structure à travers les échelles. Ces résultats nous aident à conclure que les exposants de singularité sont en mesure de conserver les importantes caractéristiques multi-échelles d'un signal le long des échelles.

Après avoir étudié les relations entre exposants de singularité et transitions dans un signal turbulent, nous passons à la deuxième étape de notre étude qui consiste à reconstruire un signal turbulent à partir des informations de sa structure multi-échelles associée aux transitions définies par les exposants de singularité. En effet, si les bords définis par ces exposants encodent de manière satisfaisante les caractéristiques multi-échelles plus importantes d'un signal, il devrait être possible de reconstruire un signal complexe quelconque à partir des bords. Nous étudions donc la performance des systèmes reconstructibles à la fois avec des transitions associées à des exposants de singularité et des pixels de

bord fournis par les algorithmes classiques de détection de bord. Des exemples sont choisis parmi les signaux naturels les plus difficiles à analyser: acquisition de phénomènes turbulents (phase optique et observation satellitaire de la dynamique océanique). Les résultats montrent clairement la supériorité de la reconstruction obtenue à partir de la VPS sur les sous-ensembles définis par les opérateurs classiques de détection de bord. Par l'application de différentes techniques pour reconstruire une image à partir de ses bords, on observe la supériorité générale de la reconstruction à partir de la VPS pour les signaux qui sont des images d'acquisitions de phénomènes naturels complexes. Les résultats nous permettent de tirer une autre conclusion importante : les exposants de singularité, non seulement conservent les caractéristiques multi-échelles d'un signal, mais il est également possible de reconstruire le signal à partir d'un sous-ensemble de ses points les plus informatifs.

Ces études préliminaires étant destinées à valider l'utilisation des exposants de singularité pour l'inférence optimale dans l'analyse multi-résolution, nous démontrons le potentiel de cette idée, dans le chapitre 6, pour la reconstruction de la phase d'un front d'onde turbulent. Nous étudions un schéma d'analyse multi-résolution associée au signal d'exposants de singularité permettant une approximation acceptable d'une analyse multi-résolution optimale. Trois types de phase sont utilisés pour fournir des données d'entrée haute résolution nécessaires à l'analyse multi-résolution quasi-optimale. Le premier type de phase permet de valider les performances de notre algorithme en utilisant la vérité terrain, c'est à dire que nous utilisons la véritable phase haute résolution en entrée. La très bonne qualité des résultats obtenus dans ce cas nous conduit à utiliser d'autres données de phase haute-résolution: la moyenne de la phase vraie (calculée sur un intervalle centré sur l'instant courant et dont la demi-longueur temporelle est de 10 phases d'acquisition) puis une phase atmosphérique dont le spectre de puissance respecte celui prévu par la théorie de Kolmogorov. Les résultats obtenus, comparés avec ceux obtenus par l'approche classique en AO par moindres carrés montre clairement le potentiel de notre approche en estimation de phase du front d'onde, notamment en présence de bruit, où l'approche basée sur le FMM se révèle supérieure.

Perspectives

La recherche présentée dans cette thèse a ouvert une nouvelle direction pour le problème de la reconstruction de la phase du front d'onde en AO. Les simulations indiquent clairement le potentiel de cette approche avec des résultats supérieurs ou égaux à ceux obtenus par des solutions linéaires classiques (avec une supériorité marquée dans le cas du bruit, au moins pour le type de bruit gaussien considéré dans cette thèse).

Une première perspective sera de mettre en œuvre notre algorithme de reconstruction dans un système AO et voir sa performance en temps réel. En fait, les exposants de singularité, qui sont les ingrédients de base utilisés dans la technique de reconstruction, peuvent être calculés en temps réel avec une utilisation minimale de ressources.

La technique de reconstruction que nous avons proposée dans cette thèse est généralisable au cas d'autres types de systèmes complexes.

Ces futures extensions du présent travail sont susceptibles de justifier l'utilisation du FMM pour l'analyse des caractéristiques multi-échelles dans les signaux complexes.

Publications

Revue internationale à comité de lecture

S. K. Maji, H. Yahia and H. Badri: Reconstructing an image from its edge representation, *Digital Signal Processing*, Elsevier, 23 (6): 1867-1876, 2013.

S. K. Maji and H. Yahia: Edges, Transitions and Criticality, *Pattern Recognition*, Elsevier, Accepted, 2013.

Conférences internationales à comité de lecture

S. K. Maji, O. Pont, H. Yahia and J. Sudre: Inferring Information across Scales in Acquired Complex Signals, *European Conf. Complex Systems*, Brussels, 2012.

S. K. Maji, H. Yahia, O. Pont, J. Sudre, T. Fusco and V. Michau: Towards Multiscale Reconstruction of Perturbed Phase from Hartmann-Shack Acquisitions, *IEEE AHS*, Nuremberg, 2012.

S. K. Maji, H. Yahia, O. Pont, T. Fusco, V. Michau and J. Sudre: A multiscale approach to phase reconstruction for Adaptive Optics, *IEEE ECMS*, Liberec, Czech Republic, 2011.

ACKNOWLEDGEMENTS

This work is the result of guidance and help of several individuals who in one way or another contributed in preparation and completion of this study. I am grateful to everyone who has helped me in this process.

First, I want to thank my supervisor Dr. Hussein Yahia without whom this thesis would not have been possible. Always present, he encouraged me during these three years, made me share his extensive experience in the field of image processing and guided me throughout the work. I thank him for the patience he has shown and the confidence he has placed in me throughout this thesis. These three years were very rich on many levels, and I thank him sincerely.

I also express my sincere gratitude to Dr. Thierry Fusco from ONERA for his scientific advise and suggestions that has helped me to enrich my knowledge and improve my work. He provided us with the necessary data to carry on this research work and was always available for discussions despite his busy schedule. I also thank Khalid Daoudi and Oriol Pont for their co-operation. Special thanks to Joël Sudre for his help on software simulations during my PhD. I am thankful to Josy Baron for managing all the administrative work on my behalf.

My co-workers will deserve a special position in this section for their contributions to my PhD. I will start with Vahid Khanagha whose support in the form of scientific discussions and advise had been extremely beneficial to me. The same with Hicham Badri has also helped me a lot to venture into new areas of research and apply them into my field of interest. Special thanks to Denis Arrivault for encouraging me and keeping up my spirits, to

Binbin Xu for his support during my final but crucial days of PhD. Thank you to Harish Kumar, Joshua, Nicolas, Andrea, Luca and Stojce for your company.

Special thanks to many friends I met in Bordeaux who made my stay a cheerful experience. Their presence helped me a lot to overcome difficult times and rejuvenate myself. It would not be possible without them.

And finally, I thank my parents to whom I dedicate my thesis and my achievements. Words cannot justify the contribution and sacrifices that they have made to fulfill my dream.

CONTENTS

Résumé	iii
Abstract	v
Acknowledgements	vii
List of figures	xiii
List of tables	xix
1 Introduction	1
1.1 Motivation of the research	1
1.2 Objective of the research	3
1.3 Organization of the thesis	6
2 Atmospheric turbulence and wavefront propagation	9
2.1 Atmospheric turbulence	9
2.1.1 Variations in the refractive index	10
2.1.1.1 Structure function of the refractive index variations	10
2.1.1.2 Power spectral density of the refractive index variations	11
2.1.1.3 Refractive index structure constant	12

2.1.1.4	Fried parameter	12
2.2	Effects of turbulence on wavefront phase	13
2.2.1	Structure function of the turbulent phase	14
2.2.2	Power spectrum of the turbulent phase	14
2.3	Imaging through turbulence	15
2.3.1	The point spread function (PSF)	15
2.3.2	The optical transfer function (OTF)	16
2.4	Modal decomposition of the phase	18
2.5	Simulation of the turbulent phase	20
2.5.1	Zernike realization of the phase screen	21
2.5.2	Fourier based representation of the phase screen	22
2.6	Conclusion	23
3	Adaptive Optics and wavefront reconstruction	25
3.1	The Adaptive Optics system	26
3.1.1	Deformable mirrors	26
3.1.2	Wavefront sensors	27
3.1.2.1	Shack-Hartmann wavefront sensor	28
3.1.3	The controller	30
3.2	Wavefront reconstruction	30
3.2.1	The Zonal approach	32
3.2.2	The Modal approach	33
3.2.3	Least squares wavefront reconstruction	34
3.2.4	Wavefront reconstruction as an inverse problem	34
3.2.4.1	Maximum likelihood method	35
3.2.4.2	Maximum <i>a posteriori</i> method	35
3.2.4.3	Minimum variance wavefront reconstruction	36
3.3	Conclusion	37
4	The Microcanonical Multiscale Formalism (MMF)	39
4.1	The concept of fractals	41
4.1.1	Box-counting dimension	42
4.1.2	Hausdorff dimension	42
4.2	Description of a multifractal system	43

4.2.1	Canonical approach to multifractals	43
4.2.2	Microcanonical approach to multifractals (MMF)	45
4.2.2.1	Singularity exponents	45
4.2.2.2	Singularity spectrum	46
4.2.3	Relation between canonical exponents τ_p and singularity spectrum $D(h)$	47
4.3	Estimating the singularity exponents	48
4.3.1	Singularity analysis via log-log regression	49
4.3.2	Singularity analysis via wavelet projection	50
4.4	Conclusion	51
5	Critical exponents and inference across the scales	53
5.1	Optimal Inference across scales : Realizing the microcanonical cascade	55
5.1.1	Multiresolution Analysis & wavelet transform	56
5.1.1.1	Realizing the scaling function	57
5.1.1.2	Realizing the wavelet function	58
5.1.1.3	Multiscale representation of a signal using wavelet transform	59
5.1.2	Approximating the microcanonical cascade	62
5.1.3	Choice of wavelet	66
5.2	Edge detection and critical exponents	69
5.2.1	Edges, unpredictability and critical exponents	71
5.2.1.1	Computation of the singularity exponents	73
5.2.1.2	Comments: The case of turbulent signals	76
5.2.2	Edge consistency across the scales	77
5.3	Reconstructing an image from its edge representation	83
5.3.1	Framework of Reconstructible Systems	85
5.3.1.1	Problem Formulation	85
5.3.1.2	Linear systems	85
5.3.2	Reconstruction from MSM (R_{msm})	87
5.3.3	Computational complexity	89
5.3.4	Choice of images	90
5.3.5	Results	90

5.4	Conclusion	103
6	A multiscale approach to phase reconstruction for AO	105
6.1	Description of data	107
6.2	Reconstruction technique	108
6.3	Results	112
6.4	Residual phase statistics	113
6.5	Results and discussion	117
6.6	Conclusion	121
7	Conclusion	123
7.1	Future perspectives	125
7.2	Publications	127
	Bibliography	129

LIST OF FIGURES

2.1	The effects of atmospheric turbulence on an incoming spatial wavefront. The incoming planar wavefront from a distant spatial object, upon entering the Earth's atmosphere (a homogeneous medium), gets distorted resulting in a phase degradation in the wavefront.	13
2.2	Graphical representation of the first 28 Zernike Polynomials.	20
2.3	Zernike realization of a turbulent wavefront phase with the addition of increasing number of polynomials. Realization of the phase with : (a) all Zernike polynomials (b) piston only ($i=1$) (c) first 3 polynomials (d) first 5 polynomials (e) first 9 polynomials (f) first 13 polynomials (g) first 28 polynomials (f) first 37 polynomials.	21
2.4	Fourier representation of a turbulent phase using: (a) Kolmogorov power spectrum (b) Von Karman power spectrum (c) PSD comparison of (a) and (b).	22
3.1	Schematic representation of an Adaptive Optics system (Courtesy: J. Vallergera [204]).	26

-
- 3.2 Schematic representation of a Shack-Hartmann wavefront sensor. An incident wavefront travelling along the Z -axis, after entering the telescope pupil, is sampled by an array of lenses (called lenslet array), and forms an image of the source on the CCD array. If the wavefront is plane, each lenslet forms an image of the source at its focus (marked by red). If the wavefront is distorted, the images are shifted from their reference position (marked by black). This shift in position is proportional to the mean slope of the wavefront and can be measured with equation(3.2) and equation(3.3). 29
- 3.3 AO correction of astronomical images. **Top row** : H-band image of Uranus and the moon Miranda (faint point at the bottom) captured using ground-layer adaptive optics system (GLAS). (a) Uncorrected image. (b) with AO correction. Image courtesy: Isaac Newton Group of Telescopes. **Bottom row** : 20×20 arcsecond region near the center of the globular cluster Omega Centauri. (c) without AO correction. (b) with MCAO correction. Image courtesy: Enrico Marchetti. . . 31
- 3.4 Fried Geometry for the (i, j) th sub-aperture. A measurement of the gradient of the phase is provided by a wavefront sensor at (x_i, y_j) . The phase values at the corners of the sub-aperture are then estimated. 32
- 4.1 The sequence of sets approaching the von Koch curve after 1, 2, 3 and 4 iterations. 42
- 4.2 Singularity spectrum for the phase screen shown in Fig 2.3a. (a) Reduced singularity spectra $D(h) - d$ at the finest scale (resolution) r_0 . (b) Reduced singularity spectra $D(h) - d$, with errorbars, at the finest possible scale r_0 , twice the finest possible scale r_1 and three times the finest scale r_2 46

4.3	(a) Image of a simulated optical phase perturbed by atmospheric turbulence. The image corresponds to a 128×128 pixels sub-image extracted from an original 256×256 pixels image to avoid the pupil boundary. (b) Image of the singularity exponents computed on the phase data using β -Lorentzian wavelet.	50
5.1	Realization of sub-space by scaling and wavelet functions: (a) Sub-space relationship of scaling functions. (b) Sub-space relationship of scaling and wavelet functions.	57
5.2	Representation of the decomposition in multiresolution analysis. $\langle \alpha_j \rangle$ is the approximation of the initial image $\langle \alpha_0 \rangle$ at the resolution j . $\langle \alpha_j^1 \rangle$, $\langle \alpha_j^2 \rangle$ and $\langle \alpha_j^3 \rangle$ are the horizontal, vertical and diagonal details respectively at the resolution j	60
5.3	(a) Realization of $\langle \epsilon_{0,0} s(\vec{x}) \rangle$, from equation (5.27), for the Benzi model [24], at 48×48 pixels resolution. (b) X -cut of (a). (c) Y -cut of (a).	65
5.4	Conditional histograms of the experimental phase data. The wavelet used for this experiment is the order 3 Battle-Lemarié wavelet with 41 central coefficients. The horizontal axis corresponds to $\ln \alpha_p $ and the vertical to $\ln \alpha_c $. Top: Approximation coefficients are shown in the left image, diagonal details (orthogonal complements) are shown in the right image. Bottom: Horizontal details are shown in the left image, vertical details on the right image (both correspond to the orthogonal complements in multiresolution analysis).	67
5.5	(a) Flowers - image imk01305 of van Hateren database. (b) visualization of the singularity exponents $h(\vec{x})$ computed via Lorentzian wavelet over the image.	72
5.6	Edges corresponding to the MSM points for the image imk01305 of van Hateren database. (a) compact representation of MSM points corresponding to 35 % pixel density. (b) MSM points corresponding to 25 % pixel density. (c) MSM points corresponding to 15 % pixel density.	74

-
- 5.7 This figure illustrates the complexity of edge detection in the case of turbulent images. The edge pixels are marked red or blue according to the sign of the scalar product between the normal to the set of edge and the image gradient at that point. **Top row** (from left to right): an excerpt from the sea surface temperature (SST) image (MODIS data) of the Agulhas current below the coast of South Africa, set of edge pixels computed by MSM corresponding to 25% of pixel density in the selected area. **Bottom row** (from left to right): singularity exponents of the SST image, edges produced by algorithm NLFS [107] which behaves the best among the classical edge operators tested (see table 5.8). The coherent structures are not respected by NLFS, showing the superiority of MSM. . . . 76
- 6.1 (a) Image of a simulated phase perturbed by atmospheric turbulence (see section 6.1 for imaging characteristics). The image corresponds to a 128×128 pixels sub-image extracted from an original 256×256 pixels image to avoid the pupil's boundary. (b) Point spread function (PSF) image associated to the image of the perturbed phase. . . . 108
- 6.2 Representation of the analysis process. We take as input a high-resolution 128×128 pixels phase screen. We then compute the singularity exponents of this high-resolution phase screen and do a multiresolution analysis (MRA) over the exponents. The high-resolution phase screen can be the true phase itself, an average instance of the true phase over time or any random phase screen with Kolmogorov turbulence statistics. Here, α_j is the approximation of the initial image (i.e. the image of the singularity exponents) at the resolution j . Level 1 MRA results in a coarser approximation of α_j i.e. α_{j+1}^0 (size: 64×64 pixels) and the details α_{j+1}^1 , α_{j+1}^2 and α_{j+1}^3 . The process is repeated four times to get an approximation of size 16×16 pixels. . . . 109

6.3	Representation of the synthesis process. Here the low-resolution 16×16 pixels approximation obtained from the analysis part are replaced with the low-resolution 16×16 pixels gradient of the phase. Then with the knowledge of the details at every level, the signal is reconstructed from 16×16 pixels to 32×32 pixels, then to 64×64 pixels (α_{j+1}^0) and finally to 128×128 pixels i.e. α_j . The process is repeated for both x and y gradients to obtain a high-resolution estimate of the phase gradients at 128×128 pixels.	110
6.4	(a) Image of a simulated turbulent phase screen generated by the FFT based method [134] using a Kolmogorov power spectrum. (b) Singularity exponents computed on the phase data.	117

LIST OF TABLES

2.1	Effects of turbulence on image formation in ground-based astronomy. Top row (from left to right): Simulated negative image of a point source (star) in an ideal telescope without atmosphere (corresponds to an <i>Airy</i> function), the X cut and Y cut of the image. Bottom row (from left to right): Simulated negative image showing what a point source (star) would look like through a ground-based telescope in presence of atmosphere (the <i>speckle</i> formation of the image is due to the turbulence in the atmosphere), the X cut and Y cut of the speckle image.	17
2.2	Zernike Polynomials.	18
5.1	Inconsistent behaviour of edges along the scales. Image used is an excerpt from the sea surface temperature (SST) image. Different resolutions of the SST image are the approximation coefficients resulting from a standard Haar discrete wavelet transform. We show the results of the following edge detection algorithms: MSM (proposed edge detection algorithm), Canny and multiscale Canny (mC) edge detection [130]. D corresponds to the pixel density of the respective edges. For edges computed using Canny edge detector, α specifies the lower sensitivity threshold and σ is the standard deviation of the Gaussian filter.	78

5.2	Inconsistent behaviour of edges along the scales. Image used is the clock image from SIPI image database [3]. Different resolutions of the clock image are formed by taking the approximation coefficients of Haar discrete wavelet transform.	79
5.3	Evaluation of edge consistency across scales using Lindeberg [115] scale space representation. Row 1 (from left to right): different resolutions of the clock image obtained by changing the scale parameter t (explained in section 5.2.2). Row 2: compact representation of MSM points. Row 3: edges computed using Lindeberg edge detector.	80
5.4	Evaluation of edge consistency across scales using Lindeberg scale space representation. Row 1 (from left to right): different resolutions of the SST image obtained by changing the scale parameter t . Row 2: compact representation of MSM points (pixel density fixed at 16%). Row 3: edges computed using Lindeberg edge detector.	81
5.5	Images used for our experiments. Row 1 (from left to right): Harrington weave, Hibiscus, Car, Lena, Turbulence degraded atmospheric phase, imk01310, imk03324, imk04050. Row 2: Brick wall, House, imk03322, Boat, Camille, Aerial view of a truck, Julia Roberts, Sea Surface Temperature (SST) image of the Agulhas current below the coast of South Africa. Image description is available in table 5.6.	89
5.6	Description of the experimental images shown in table 5.5.	91
5.7	Quantitative analysis: Evaluation of the reconstruction over different edge detection algorithms, in terms of PSNR and MSE, corresponding to Table 5.8. D represents the pixel density of the edges.	94
5.8	Results of reconstruction over different edge detection algorithms. Image description: Row 1: Harrington weave, Row 2: Hibiscus, Row 3: Car, Row 4: Lena, Row 5: imk01310, Row 6: imk03324, Row 7: imk04050, Row 8: Phase, Row 9: SST. . .	95

5.9	Performance under noise: Reconstruction results on different edge detection algorithms under different levels of Gaussian white noise.	96
5.10	Quantitative analysis (noisy environment): Evaluation of the reconstruction over different edge detectors. The 1st, 2nd and 3rd row, for every image, represents the performance under input SNR of 26 dB, 14 dB and 6 dB respectively.	96
5.11	Performance of different reconstruction algorithms. Row 1: Brick wall Row 2: House Row 3: imk03322 Row 4: Aerial view of a truck Row 5: Julia Roberts Row 6: SST image.	98
5.12	Quantitative analysis: Evaluation of the reconstruction algorithms, corresponding to Table 5.11, in terms of PSNR (in dB) and MSE.	99
5.13	Quantitative analysis for noisy environment: Evaluation of the reconstruction algorithms, in terms of PSNR and MSE, under different levels of noise.	99
5.14	Quantitative analysis of the performance of different reconstruction algorithms over different edge detectors: Data marked in blue indicates the reconstructor that performs the best, over other reconstruction techniques, for a particular edge detection algorithm. Data underlined indicates the edge detection algorithm that gives the best result, in terms of reconstruction, over all the other edge detectors, for a particular reconstructor.	101
5.15	Performance of different reconstructors over different edge detectors. Each row indicates the performance of the reconstructors for a given edge detection algorithm. Every column shows the edge detection algorithm that gives the best result, in terms of reconstruction, for a particular reconstructor.	102

6.1	Left to right : True phase, reconstruction of the phase using signal of the singularity exponents as input to the multiresolution decomposition, comparison of the PSD between the true phase and the reconstructed phase, reconstruction of the phase using the true phase as input to the multiresolution decomposition.	112
6.2	Results of the reconstruction in a noisy environment. Top row : Reconstructed phase under different levels of SNR. Bottom row : Comparison of the PSD between the true phase and the reconstructed phase under different levels of SNR.	113
6.3	Evaluation of the phase reconstruction of table 6.2 in terms of MSE and PSNR metrics.	113
6.4	Performance under noise - Point spread function (PSF) . The X cut and Y cut of the PSF are displayed. The y -axis corresponds to the square of the normalized image plane irradiance and the x -axis corresponds to the angular distance in arcseconds.	114
6.5	Performance under noise - Modulus of OTF (MTF) . The X cut and Y cut of the MTF are displayed with a logarithmic scale. The y -axis corresponds to the logarithm of the MTF and the x -axis represents the normalized frequency in D/λ units.	115
6.6	Comparison of the residual phase statistics with classical operators under different levels of SNR. To estimate ϕ_{cor} using the MMF technique, we use the singularity exponents computed over the true phase as input high-resolution phase in the decomposition process of our algorithm.	118
6.7	Comparison of the residual phase statistics with classical operators under different levels of SNR. To estimate ϕ_{cor} using the MMF technique, we use the singularity exponents computed over the average phase instance (obtained by averaging the 10 previous and 10 post instances of the true phase) as input high-resolution phase in the decomposition process of our algorithm.	119

6.8	Comparison of the residual phase statistics with the least squares operator under different levels of SNR. To estimate ϕ_{cor} using the MMF technique, we use the singularity exponents computed over a fixed FFT based Kolmogorov phase screen (see Fig 6.4) as input high-resolution phase in the decomposition process of our algorithm.	120
-----	---	-----

- CHAPTER 1 -

INTRODUCTION

The research performed in this thesis is about proposing a novel approach to wavefront phase reconstruction in Adaptive Optics (AO). The primary goal is to make use of advanced non-linear and multiscale analysis methods in signal processing for reconstructing the phase, through appropriate multiresolution analysis, using ideas coming from the novel framework of Microcanonical Multiscale Formalism (MMF); we apply these ideas for estimating a turbulent wavefront phase from the low-resolution sensor measurements of an AO system (a particular case of the general problem known sometimes as «super-resolution»¹ in signal processing jargon [13, 56, 222, 25, 196]). The aim of this research is to propose an alternative to the classical **inverse problem formulations** used in AO, with the objective of improved performance and comparison with existing techniques.

§ 1.1 MOTIVATION OF THE RESEARCH

Light emitted from distant spatial objects, before entering the Earth's atmosphere, are planar wavefronts. The Earth's atmosphere is a time-varying

¹High-resolution gradients are generated from low-resolution gradients (corresponding to low-resolution sensor measurements) and then the phase is estimated from these high-resolution reconstructed gradients. We work with the complete set of low-resolution gradient measurements and not selected measurement of the gradients.

inhomogeneous medium. When a planar wavefront propagates through this medium, refractive index variations of the air changes, to a considerable extent, the phase associated to the wavefront. This gives rise to a turbulent phase perturbation with the consequence of causing a limitation in the optical resolution of ground-based astronomical devices : acquisitions are «blurred» and there is a considerable loss in the spatial resolution of the instrument, compared to its theoretical limit resolution power.

One of the most common technology employed for ground-based observation of astronomical objects, and to overcome the limitation of low spatial resolution problems, is the Adaptive optics (AO). An AO system tries to eliminate the distortions in the wavefront phase, in real-time, with the help of a deformable mirror (DM) and a well designed servo-loop. A wavefront sensor (WFS) placed behind the mirror helps to measure these distortions, which is then passed through the servo-loop, as command, to the DM. The DM then tries to adjust its shape according to the shape of the incident wavefront to reduce wavefront residual phase error. The process is repeated iteratively to compensate the effects of atmospheric turbulence on the wavefront. The first generation of AO system, also known as SCAO or Single-Conjugate Adaptive Optics, was designed with a single DM and a single WFS. However, SCAO corrections are limited to a small field of view [158, 104] and to overcome this limitation and to enhance the performance of ground-based observations, several other AO concepts were introduced. For example in Multi-Conjugate Adaptive Optics or MCAO systems [20, 48, 67], multiple deformable mirrors and wavefront sensors are used to provide improved resolution in a large field of view. Other techniques like Ground Layer Adaptive Optics (GLAO) [160] and Extreme Adaptive Optics (XAO) [69] are also used to enhance the performance of ground-based telescopes.

AO technology primarily finds its application in ground-based astronomy and in defense applications [164]. However, the technology is getting increasingly popular in ophthalmology [40, 49]. The principle of AO technique was first proposed by Horace W. Babcock [12] in 1953. However, it was not until the 1990's that the idea of AO was first demonstrated in astronomical observations [171, 172]. Optical testing devices were the major source of inspiration for designing a WFS [170, 104]. The WFS records the wavefront

distortions in the form of slope measurements (gradients of the phase) [164], like the Shack-Hartmann (SH) WFS, or curvature measurements (Laplacian of the phase) [163], like the curvature WFS. The primary objective of any AO system is to estimate the wavefront phase values from the discrete measurements (gradients or Laplacian of the phase) provided by a wavefront sensor. The wavefront phase estimation is then classically formulated as an inverse problem [170, 137]. The techniques generally used to estimate the phase are: the maximum likelihood technique and the maximum *a posteriori* technique. Both these techniques yield to the generalized *least squares solution*, which is the solution classically used for estimating the phase under real-time constraints [137].

§ 1.2 OBJECTIVE OF THE RESEARCH

In this thesis, we propose, explore and experiment a completely different approach for phase reconstruction in AO. The motion of the upper-layers in the atmosphere, where the incoming wavefront are perturbed, are turbulent. Turbulent flows, although extremely chaotic in nature (since they belong, at high Reynolds number, to the field of Fully Developed Turbulence (FDT)), can be adequately described by a well defined multiscale and multifractal hierarchy. They are the place where multiplicative cascade phenomena are observed for intensive variables, and coherent structures are related to the transfer of energy between the scales [7, 64, 202, 185]. Consequently, a careful examination of the multiscale structure of turbulence has the potential of optimal inference across the scales of a turbulent acquisition. **In this work, we examine the problem of cross-scale information inference through the determination of a multiresolution analysis that suits best the multiscale structure of turbulence.** The methodology encompasses a large class of problems in Complex Systems Science and can be applied to propagate information across the scales for a wide variety of complex signals [124, 217]. We demonstrate that the MMF, set up for understanding and evaluating the mechanisms that govern the evolution of complex dynamical systems, can be successfully applied to the problem of turbulent phase

reconstruction from low-resolution gradient measurements. Consequently, we first focus on the determination of appropriate parameters, necessary to characterize the multiscale features of a complex signal. In non-linear physics, it is well known for instance in the study of ferromagnetism, that susceptibility, spontaneous magnetism, critical isotherm and heat capacity all have power-law behaviour in the vicinity of a critical point $t = t_c$ with values, called **critical exponents**, which can be predicted by the mean-field approximation [23]. Systems with high order transitions commonly reflect a power-law behaviour in their thermodynamical variables [202, 203]. This power-law behaviour of physical intensive variables around a critical point is known to be a fingerprint of scale invariance [109]. Moreover, the critical exponents are **universal** : close to the critical point, the details of the microscopic dynamics of the system become irrelevant, the macroscopic characteristics of the system are determined by these critical exponents, and systems having same distributions of critical exponents share equivalent macroscopic characteristics [154, 187, 203]. As a consequence of universality, critical exponents stand for a suitable mean for analysing complex systems as a whole [154]. There has been a considerable amount of work done by researchers in the past decades to characterize the multiscale and multifractal organization of complex systems; the most well-known approaches are related to the characterization of singularity spectra and the methods to compute them [7, 213]. These techniques require a lot of realizations for the computation of singularity spectra, and they determine the power-laws appearing in the limiting behaviour of moments of variables, not the geometrically localized critical exponents [202]. In the MMF, critical exponents are determined at high numerical precision at each point of the signal domain, using only one realization (or acquisition) and specific vectorial measures associated to predictability [32, 155]. Consequently, the MMF provides a suitable approach in the determination of localized critical exponents, which we call **singularity exponents** in the sequel; it is a formalism that has led to a sensible improvement in the design of numerical techniques for the determination of multiscale characteristics of natural complex signals.

Since turbulent signal possess a multiscale hierarchy which is closely related to the cascading properties observed in FDT, there must exist specific

multiresolution analysis that allow optimal inference of physical intensive variables across the scales of turbulent acquisition data. Similar and related ideas have been pervasive in multiscale statistical inference these past few years [191, 92, 58, 91]. This observation can be made precise through the notion of **optimal wavelet**, introduced in other contexts such as econometry and oceanography [199, 198, 152, 156]. The proper determination of an optimal wavelet, associated to turbulent wavefront acquisitions, would then allow us to reconstruct, in an optimal way, a phase from its low-resolution gradients with minimum error. Up to now, however, obtaining such a wavelet at high numerical precision from acquired data turns out to be a very difficult problem, and the attempts made so far produce only an approximation of it, not sufficient enough to ensure optimal transport across the scales (high numerical precision is a key element in any processing of turbulent signals). **In this thesis we observe experimentally that, instead of computing a multiresolution analysis associated to an optimal wavelet, one is able to obtain a close to optimal inference across the scales by applying classical multiresolution analysis on the singularity exponents of a phase signal. In other words, a classical multiresolution analysis performed, not on the signal itself, but on its singularity exponents, allows an (close to) optimal inference of physical variables across the scales.**

The primary reason behind this idea is the following : once determined at high numerical precision, the singularity exponents provide a much richer framework for describing the multiscale hierarchy present in turbulence, and they can be used to retrieve singularity spectra as well. Singularity exponents encode the transitions present in the signal and, particularly, in the case of well defined rigid objects, they contain the classical notion of edge pixel. Indeed, one of the main feature among multiscale characteristics in a signal is given by the classical notion of edge. Edge pixels form the most informative subset of an image, well known at least in the case of well defined objects, and one can reconstruct the object from the knowledge of its edges [125]. There are many algorithms for computing edges in digital signals, and these algorithms produce appropriate edge pixels in the case of rigid or slightly deformed objects. But, in the case of turbulent signals, and specifically

in the situation of FDT, the notion of edge is not well-defined by classical edge detectors. We however see that, in the case of complex natural signals and specifically in the case of turbulence, singularity exponents provide a more adapted notion of edge [125, 124, 100]. Consequently, since singularity exponents are ideal candidates in describing the multiscale organization of a turbulent signal, and since they turn out to be the adequate (and physically substantiated, an aspect which is very important to us) generalization of edge pixel, it is logical to expect that a multiresolution analysis performed on the signal of singularity exponents, instead of the signal itself, ensures proper inference across the scales. We will see, in the following chapters of this thesis, the efficiency of this concept in the derivation of a new method for reconstructing the wavefront phase for AO. However, because of the present lack of a theoretical physics justification of the above-mentioned equivalence, we need to carry out an important preliminary work, which will be achieved in this thesis, for showing that singularity exponents are better candidates for detecting edges in the case of turbulent data. This is achieved in two steps, and presented in chapter 5: first we prove that singularity exponents provide a consistent notion of edge pixel across the scales, much more consistent than the classical edge detectors in the case of turbulent data. Then we prove that this new notion of edge outperforms the classical edge detectors, in terms of reconstructibility of the whole signal (image in our case) from given edge pixels, and is naturally robust to noise. Armed with the results of chapter 5, we can be confident that a multiresolution analysis performed on the singularity exponents will provide good inference across the scales. This idea is then exploited in chapter 6 for providing a new method for phase reconstruction in AO.

§ 1.3 ORGANIZATION OF THE THESIS

The thesis is organized as follows:

- In chapter 2, we recall the mathematical description of atmospheric turbulence and its statistical descriptors. We talk about the effects of turbulence on image formation in ground-based astronomy and the role

of the descriptors in characterizing these effects. We also talk about the various techniques used to simulate a turbulent phase, for experimental purposes.

- In chapter 3, we discuss about the concepts of AO technique and its role in reducing the wavefront phase distortions. We give a brief presentation of the principle components in an AO system and their functions. The classical wavefront phase reconstruction techniques from the WFS measurements are then discussed.
- In chapter 4, we introduce the MMF. We talk about the origin of this formalism, and then discuss about its key parameters: the singularity exponents and the singularity spectrum. The different methods of estimating the singularity exponents are then explained.
- In Chapter 5, we introduce the concept of optimal inference across the scales of a given signal. We emphasize on the idea that singularity exponents of a signal are well-justified candidates for extracting information, across scales, through a multiresolution analysis. We justify this idea in section 5.2 and section 5.3.

In section 5.2, we discuss about the process of determining edges from the singularity exponents. We show that the edges obtained from the singularity exponents, for a given image, are much more consistent across the scales compared to edges detected by classical edge detectors, notably in the case of turbulence that interests us in this work. We justify our approach using two scale-based representation of images: the dyadic wavelet transform and the Lindeberg scale space representation.

In section 5.3, we prove the concept of edges (detected by singularity analysis) as the most informative set, by its ability to give an accurate reconstruction of the whole image compared to classical edges. In the process, we re-examine image reconstruction from their edges [197, 203] and show that it provides superior results, in terms of compact representation [16, 17, 15], over the state-of-the-art surface reconstruction techniques.

- In chapter 6, we introduce our wavefront phase reconstruction technique, using MMF, associated to a multiresolution analysis on the singularity exponents with an approximative version of the optimal wavelet (related to the phase signal). We evaluate the quality of our reconstruction by comparing the power spectral density (PSD), the point spread function (PSF) and the modulus of the optical transfer function (OTF) of the reconstructed phase with that of the true phase. We also compare the results of our reconstruction technique with classical least squares reconstruction technique.
- Finally, we conclude in chapter 7.

- CHAPTER 2 -

ATMOSPHERIC TURBULENCE AND WAVEFRONT PROPAGATION

§ 2.1 ATMOSPHERIC TURBULENCE

The Earth's atmosphere is a turbulent environment. Solar energy heats up the Earth's surface, and the boundary layers of the atmosphere gets heated giving rise to local unstable air masses that are always in motion (known as convection current). The motion of the air masses results in the formation of kinetic energy that creates turbulence. This energy causes the formation of vortices, also known as *turbulent eddies* [192], with a characteristic size ranging from hundreds of meters (outer scale of turbulence L_0) to the order of a few millimeters (internal scale turbulence l_0). Energy is transmitted successively from the higher size vortices to increasingly lower size vortices, until they are no longer able to retain their distinct characteristics. The area between these two characteristic sizes (or scales, i.e. L_0 and l_0), where turbulence is fully developed, is called the *inertial range*. Knowledge of this domain is important in describing the major reasons behind the degradation of images in ground-based astronomy [65]. It is of primary importance to recall the statistical description of a turbulent wavefront used in optics in order to understand the type of correction used in classical approaches for phase reconstruction in AO, and also to underline the novelty of the reconstruction

process undertaken in this thesis.

2.1.1 Variations in the refractive index

The starting point of getting insight into the properties of atmospheric turbulence is to view the refractive index of the atmosphere as a random process [6]. The atmospheric refractive index n , at a given point r in space, can be expressed in terms of temperature and pressure variations as:

$$n(r) = k(\lambda) \frac{P(r)}{T(r)} \quad (2.1)$$

where $k(\lambda)$ is a coefficient that depends on the optical wavelength λ (for $\lambda = 0.5\mu\text{m}$, $k(\lambda) = 77.6 \times 10^{-6}$) [93], P is the pressure in millibars, and T is the temperature in Kelvins. A precise knowledge of the atmospheric refractive index for all points r and at every moment of time is inaccessible [6]. This gives rise to the necessity of a statistical descriptor to best represent the atmosphere [179].

2.1.1.1 Structure function of the refractive index variations

In astronomy and other physical sciences, the description of the random variations, either in space or time, in the index of refraction, is making use of the terminology set up in probability theory for second order stochastic processes and is called in physics as the structure functions. The structure function, $D_n(r)$, of the index of refraction can be defined as the mean-square difference of $n(r)$ between two given points:

$$D_n(r_1, r_2) = \langle [n(r_1) - n(r_2)]^2 \rangle \quad (2.2)$$

where r_1 and r_2 are the two given points in space and $\langle \cdot \rangle$ is an ensemble average. Assuming that the refractive index fluctuations maintain stationary increments [6], the covariance function of any two random processes $n(r_1)$ and $n(r_2)$ can be simplified to:

$$B_n(\rho) = \langle n_1(r_1)n_1(r_1 + \rho) \rangle \quad (2.3)$$

so that the covariance function $B_n(\rho)$ becomes independent of the spatial position and is only dependent on the distance between the two points of

interest: $\rho = r_1 - r_2$. The structure function is related to the covariance function by [65]:

$$D_n(\rho) = 2[B_n(0) - B_n(\rho)] \quad (2.4)$$

Following a dimensional analysis [145], it can be shown that the structure function follows a 2/3 power-law and can be written as:

$$D_n(\rho) = C_n^2 \rho^{2/3} \quad \text{for } l_0 \ll \rho \ll L_0 \quad (2.5)$$

where C_n^2 is the refractive index structure constant. The parameter C_n^2 is expressed in $m^{-2/3}$ units and is generally referred to as the strength of the turbulence [6, 167].

2.1.1.2 Power spectral density of the refractive index variations

Another means of characterizing the statistical fluctuations of the refractive index is to consider its power spectral density (PSD). The PSD can be expressed as the Fourier transform of the covariance function $B_n(\rho)$ (refer to equation (2.3)) and can be written as:

$$\Phi_n(f) = \int_{-\infty}^{\infty} B_n(\rho) e^{-2\pi i f \rho} d\rho \quad (2.6)$$

where f represents the spatial frequency. The power spectrum of the refractive index fluctuations can be expressed, in terms of C_n^2 , as:

$$\Phi_n(f) = 0.033(2\pi)^{-2/3} C_n^2 |f|^{-11/3} \quad (2.7)$$

Equation (2.7) is generally referred to as the *Kolmogorov* power-law spectrum and is only valid over the inertial range i.e. for $1/L_0 \ll |f| \ll 1/l_0$.

The Kolmogorov power spectrum can be easily extended to other power spectrum models in order to increase the valid range for the PSD. The most common among them is the *Von Karman* power spectrum and can be expressed as :

$$\Phi_n(f) = 0.033(2\pi)^{-2/3} C_n^2 (|f|^2 + f_0^2)^{-11/6} \exp\left(-\frac{|f|^2}{f_m^2}\right) \quad (2.8)$$

where $f_m = 5.92/l_0$ and $f_0 = 1/L_0$.

2.1.1.3 Refractive index structure constant

The refractive index structure constant C_n^2 is a measure of the strength of the optical turbulence [65]. It is usually expressed as a function of altitude h . The precise characterization of the $C_n^2(h)$ profile above an astronomical observatory is very important for the design of adaptive optics systems. The integrated C_n^2 profile is defined as:

$$C_n^2 = \int C_n^2(h)dh \quad (2.9)$$

The C_n^2 is highly sensitive to changes in location, time and weather conditions. Different instruments have been developed to determine experimentally the $C_n^2(h)$ profile. The most common of them are the Meteorological Balloons [11], Scintillation Detection and Ranging (SCIDAR) [80, 207], Multi-Aperture Scintillation Sensor (MASS) [194] and Slope Detection and Ranging (SLODAR) [214].

2.1.1.4 Fried parameter

Another essential parameter that can measure the effects of atmospheric turbulence on the propagation of light waves and image formation in ground-based observatory is the *Fried parameter* r_0 [61]. It is defined as the diameter that fixes the resolution limit of the telescope introduced by turbulence [65]. As a result, imaging from telescopes with aperture diameter smaller than r_0 results in reduced effect of atmospheric seeing¹. Using telescopes with aperture size more than r_0 results in the opposite effect. The Fried parameter at wavelength λ can be expressed [84] in terms of C_n^2 as:

$$r_0 = \left[0.42 \left(\frac{2\pi}{\lambda} \right)^2 \frac{1}{\cos \gamma} \int_0^\infty C_n^2(h)dh \right]^{-\frac{3}{5}} \quad (2.10)$$

with γ the zenith angle (angle of observation measured from the zenith).

¹seeing refers to the blurring of spatial objects caused due to the high frequency fluctuations in the refractive index of the Earth's atmosphere.

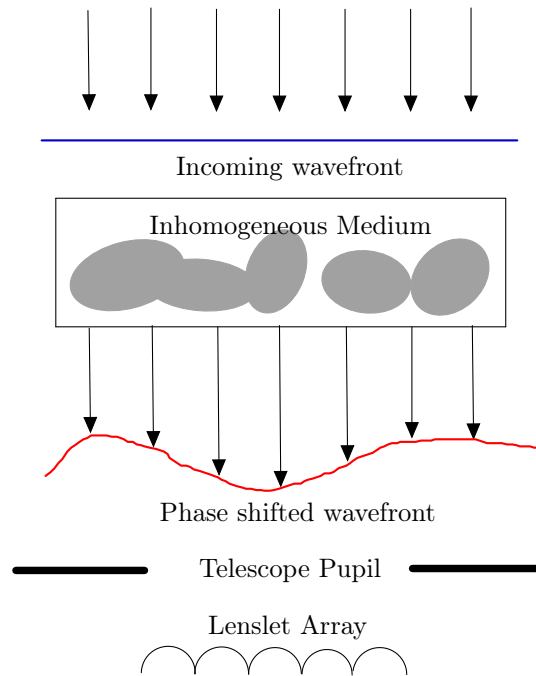


Figure 2.1: *The effects of atmospheric turbulence on an incoming spatial wavefront. The incoming planar wavefront from a distant spatial object, upon entering the Earth’s atmosphere (a homogeneous medium), gets distorted resulting in a phase degradation in the wavefront.*

§ 2.2 EFFECTS OF TURBULENCE ON WAVEFRONT PHASE

Turbulence in the Earth’s atmosphere results in refractive index variations that interfere with the propagation of light. This leads to a distortion in the planar wavefront from outer space trying to reach the ground giving rise to a phase degradation in the wavefront. The resultant complex field arising out of turbulence exhibits random fluctuations in its phase $\phi(r)$ and can be

expressed mathematically, at the telescope pupil, as [162]:

$$\Psi_0(r) = A(r)\exp[i\phi(r)] \quad (2.11)$$

where $A(r)$ is the amplitude of the resultant field. The phase $\phi(r)$ of the wavefront, after traversing through the atmosphere, is a function of the refractive index $n(r, h)$ at altitude h [65] and can be expressed as:

$$\phi(r) = \frac{2\pi}{\lambda} \int n(r, h)dh \quad (2.12)$$

where λ is the observing wavelength and integration is made along the optical path.

It is now clear from the above discussions, that the magnitude of the effect of turbulence is most noticeable in the phase $\phi(r)$ of the electromagnetic wave reaching the ground. We will now characterize the phase statistically by its structure function and power spectral density.

2.2.1 Structure function of the turbulent phase

The structure function of the phase $\phi(r)$, considered as a random process [193], can be written as:

$$D_\phi(\rho) = \langle [\phi(r + \rho) - \phi(r)]^2 \rangle \quad (2.13)$$

The equation can be further reduced [143], following the Kolmogorov-Obukhov law of turbulence, as:

$$D_\phi(\rho) = 6.88 \left(\frac{|\rho|}{r_0} \right)^{5/3} \quad (2.14)$$

where r_0 is the Fried parameter (refer to section 2.1.1.4).

2.2.2 Power spectrum of the turbulent phase

Like the structure functions, we are also interested in calculating the power spectrum of the turbulent phase. The power spectrum of a wavefront, following the law in equation (2.14), is commonly known as the Kolmogorov power spectrum and can be written as [143]

$$\tilde{\Phi}(f) = 0.023r_0^{-5/3}|f|^{-11/3} \quad (2.15)$$

Kolmogorov's PSD holds true only within a bandwidth proportional to the inertial range i.e. $1/L_0 \ll |f| \ll 1/l_0$. In this thesis, we use a Von Karman power spectrum, which can overcome the limitations of the Kolmogorov spectrum in terms of range. It takes into account two additional parameters (the inner and the outer scale) and can be written as

$$\tilde{\Phi}(f) = 0.023r_0^{-5/3}(|f|^2 + L_0^{-2})^{-11/6} \quad (2.16)$$

where L_0 is the outer scale of turbulence. When $L_0 \rightarrow \infty$, equation (2.16) approaches the Kolmogorov spectrum.

§ 2.3 IMAGING THROUGH TURBULENCE

After discussing the effects of turbulence on the degradation of a light wave, we will now study how the formation of images in ground-based telescopes are affected by this turbulence. We will focus in particular the problem of imaging through turbulence and the definition of the point spread function, which is the quantity that characterizes the damage suffered by the image of the observed object [65].

2.3.1 The point spread function (PSF)

The PSF describes the response of an imaging system to a point source or point object and characterizes atmospheric blurring effects that are spatially invariant in the immediate field of view [42]. The resultant image is therefore the PSF of the telescope + atmosphere optical system [167]. The PSF can be broadly divided based on the effects of short-exposure and long-exposure response of an imaging system towards a point source. The *short-exposure* PSF can be defined by its dependence on the wavefront profile $\Psi_0(r)$, as [42, 47, 65]:

$$k_{se}[\rho] = |\mathcal{F}^{-1}[\Psi_0(r)P(r)]_\rho|^2 \quad (2.17)$$

where \mathcal{F} denotes the 2-D Fourier transform and $P(r)$ denotes the pupil, or aperture, function i.e. is 1 inside the pupil and 0 otherwise. The *long-exposure* PSF can be considered as the ensemble average of the short-exposure

PSFs [158]:

$$k_{le}[\rho] = \langle k_{se}[\rho] \rangle \quad (2.18)$$

The PSF is determined by the size and shape of the pupil and also the phases across the pupil [47]. The goal of any AO system is to remove the phase error ϕ from the incoming wavefronts (i.e. the effect of the atmosphere optical system). If done exactly, the resulting PSF then has the form:

$$k[0] = |\mathcal{F}^{-1}\{P(r)\}|^2 \quad (2.19)$$

which is also known as the the *diffraction-limited* PSF of the telescope, and the image formed in this case is known as the diffraction-limited image [18]. In an ideal case, for a perfect telescope, the image of a point source (star) would be equal to an Airy pattern. A typical example of a diffraction limited PSF and the effect of turbulence on image formation in ground-based telescopes is shown in table 2.1.

2.3.2 The optical transfer function (OTF)

The optical transfer function (OTF) of an imaging system is defined as the Fourier transform of the PSF. Similar to the PSF, the long-exposure OTF can be defined as the ensemble average of short-exposure OTF's [193]:

$$O_{le}(f) = \langle O_{se}(f) \rangle \quad (2.20)$$

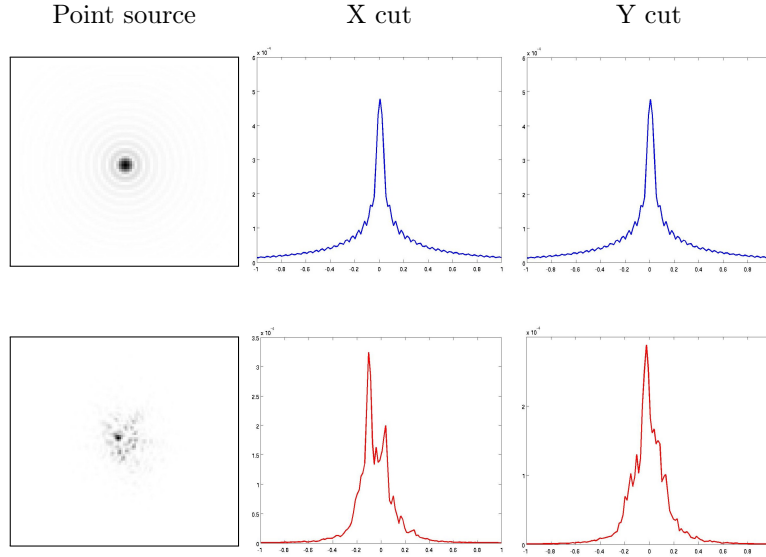
The long-exposure OTF is the result of the contribution of the telescope and the atmospheric turbulence and can be expressed as [193, 65]:

$$O_{le}(f) = O_{turb}(f)O_{tel}(f) \quad (2.21)$$

For large telescopes with good optical quality the effect of $O_{tel}(f)$ is negligible [193], so the OTF becomes a function of the OTF of the atmosphere i.e. $O_{le}(f) \approx O_{turb}(f)$. The atmospheric OTF can be expressed as a function of the phase structure function $D_\phi(\rho)$ [162], as:

$$O_{turb}(f) = \left[-\frac{1}{2}D_\phi(\lambda f) \right] \quad (2.22)$$

Table 2.1: *Effects of turbulence on image formation in ground-based astronomy. **Top row** (from left to right): Simulated negative image of a point source (star) in an ideal telescope without atmosphere (corresponds to an Airy function), the X cut and Y cut of the image. **Bottom row** (from left to right): Simulated negative image showing what a point source (star) would look like through a ground-based telescope in presence of atmosphere (the speckle formation of the image is due to the turbulence in the atmosphere), the X cut and Y cut of the speckle image.*



Following the Kolmogorov model of turbulence, substituting $D_\phi(\rho) = 6.88 \left(\frac{|\rho|}{r_0}\right)^{5/3}$ (refer to equation (2.14)), in the above equation, we get a final expression of $O_{turb}(f)$ as:

$$O_{turb}(f) = \left[-3.44 \left(\frac{\lambda f}{r_0} \right)^{5/3} \right] \quad (2.23)$$

The long-exposure OTF has the effect of averaging the high frequencies that were present in the short-exposure OTFs [65]. It has a cut-off frequency of $f \geq r_0/\lambda$, beyond which any high-frequency information is completely lost. Partial recovery of this high frequency information is possible with the use of Adaptive Optics as well as techniques like deconvolution [59, 139, 138, 94, 169]

Table 2.2: Zernike Polynomials.

Mode(<i>i</i>)	n	m	Polynomials	Name
1	0	0	$Z_1 = 1$	Piston
2	1	1	$Z_2 = 2\kappa \cos \theta$	<i>x</i> tilt
3	1	-1	$Z_3 = 2\kappa \sin \theta$	<i>y</i> tilt
4	2	0	$Z_4 = \sqrt{3}(2\kappa^2 - 1)$	Defocus
5	2	-2	$Z_5 = \sqrt{6}\kappa^2 \sin 2\theta$	<i>x</i> primary astigmatism
6	2	2	$Z_6 = \sqrt{6}\kappa^2 \cos 2\theta$	<i>y</i> primary astigmatism
7	3	-1	$Z_7 = \sqrt{8}(3\kappa^3 - 2\kappa) \sin \theta$	<i>x</i> primary coma
8	3	1	$Z_8 = \sqrt{8}(3\kappa^3 - 2\kappa) \cos \theta$	<i>y</i> primary coma
9	3	-3	$Z_9 = \sqrt{8}\kappa^3 \sin 3\theta$	<i>x</i> trefoil
10	3	3	$Z_{10} = \sqrt{8}\kappa^3 \cos 3\theta$	<i>y</i> trefoil
11	4	0	$Z_{11} = \sqrt{5}(6\kappa^4 - 6\kappa^2 + 1)$	Primary spherical

and speckle interferometry [106].

§ 2.4 MODAL DECOMPOSITION OF THE PHASE

It is a common practice in AO design to represent the turbulent wavefront phase, within the telescope aperture (or pupil), as the weighted sum of power series terms, where each term helps in explaining the wavefront distortion due to a particular aberration (or mode) [123]. Due to the circular nature of the telescope pupil, it is convenient to expand the wavefront phase distortion in terms of some basis functions that are orthogonal over a circular aperture. The most commonly used basis functions are the Zernike polynomials [143] and the Karhunen - Loève (KL) functions. The Zernike polynomials are preferred in AO due to their simplicity in analytical representation [164]; they form a set of basis functions (or modes) that are orthogonal over a unitary circular aperture. This makes them ideal candidates for accurate description of a distorted wavefront.

The Zernike polynomials, named after the renowned physicist Frits Zernike, are two dimensional polynomials that can be expressed in function of radial order n and the azimuthal frequency m [167] as:

$$Z_n^m(\kappa, \theta) = \sqrt{n+1} R_n^m(\kappa) \sqrt{2} \cos(m\theta) \quad (2.24)$$

$$Z_n^{-m}(\kappa, \theta) = \sqrt{n+1} R_n^m(\kappa) \sqrt{2} \sin(m\theta) \quad (2.25)$$

for $m \neq 0$ and

$$Z_n^0(\kappa, \theta) = \sqrt{n+1} R_n^0(\kappa) \quad \text{if } m = 0 \quad (2.26)$$

where (κ, θ) are the polar coordinates of the normalized position vector κ ($\kappa = r/R$, where R is the desired screen radius). The function $R_n^m(\kappa)$ is defined as:

$$R_n^m(\kappa) = \sum_{s=0}^{(n-m)/2} \frac{(-1)^s (n-s)!}{s! [(n+m)/2 - s]! [(n-m)/2 - s]!} \kappa^{n-2s} \quad (2.27)$$

In 1976, Noll [143] proposed an ordering scheme (mapping of m and n in terms of a single index i), by which the Zernike polynomials can be identified in terms of optical aberration. The index i is a function of n and m and is called the mode ordering number. Table 2.2 shows the ordering of the modes for the first 11 polynomials. The Zernike polynomials form a normal, orthogonal basis set [65] and can be expressed for any two polynomials Z_i and Z_j , as:

$$\int_0^{2\pi} \int_0^1 Z_i(\kappa, \theta) Z_j(\kappa, \theta) d\kappa d\theta = \begin{cases} 0 & \text{if } i \neq j \\ 1 & \text{if } i = j \end{cases}$$

A turbulent phase $\phi(r, \theta)$ can be expressed in terms of polynomial expansion over a circle of radius R as [143]:

$$\phi(R\kappa, \theta) = \sum_{i=1}^{\infty} z_i Z_i(\kappa, \theta) \quad (2.28)$$

$$\phi(r, \theta) = \sum_{i=1}^{\infty} z_i Z_i\left(\frac{r}{R}, \theta\right) \quad (2.29)$$

where $Z_i(r)$ is the i th Zernike polynomial and z_i is the corresponding Zernike coefficient. The shapes of the first 28 polynomials of Zernike are illustrated in Fig 2.3.

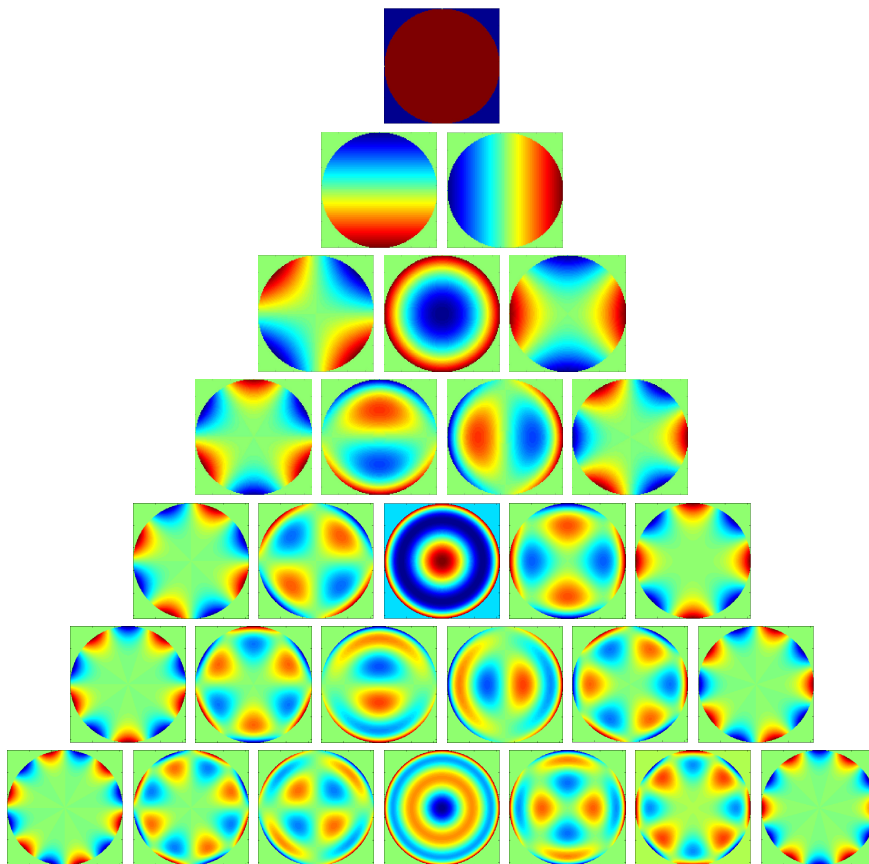


Figure 2.2: *Graphical representation of the first 28 Zernike Polynomials.*

§ 2.5 SIMULATION OF THE TURBULENT PHASE

For experimental and validation purposes of the work done in high-resolution imaging, it is important to do the numerical simulation of the phase after propagation through atmospheric turbulence [65]. There are two main approaches in the generation of atmospheric phase screens [9]: modal techniques (using basis functions like Zernike polynomials or KL modes) and sample based techniques. The sample based techniques can be either Fourier transform based [134, 108, 182] or covariance based [83]. However, for computing reasons, the Fourier based methods are more commonly used.

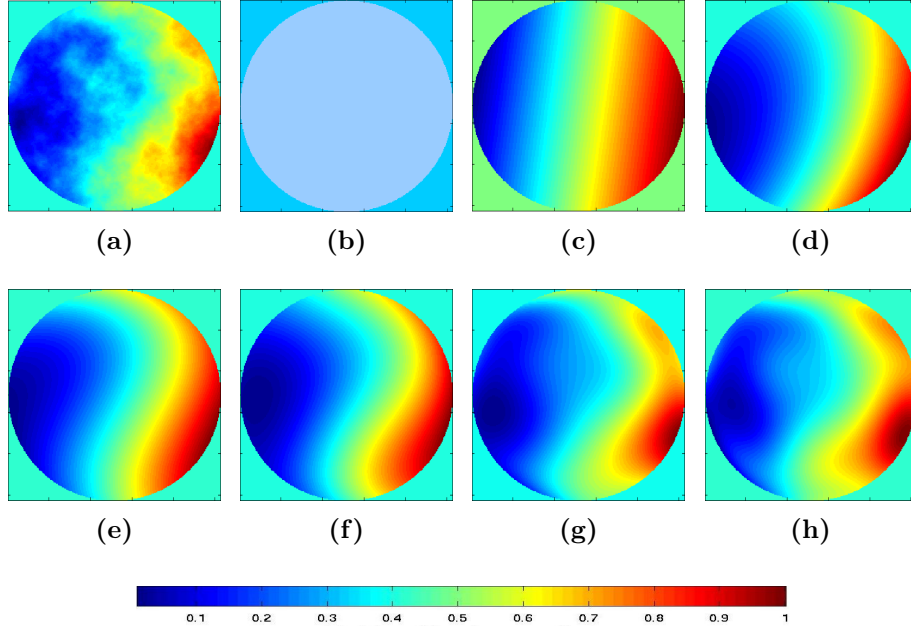


Figure 2.3: Zernike realization of a turbulent wavefront phase with the addition of increasing number of polynomials. Realization of the phase with : (a) all Zernike polynomials (b) piston only ($i=1$) (c) first 3 polynomials (d) first 5 polynomials (e) first 9 polynomials (f) first 13 polynomials (g) first 28 polynomials (h) first 37 polynomials.

2.5.1 Zernike realization of the phase screen

As explained in section 2.4, an atmospheric phase screen can be represented as a sum of all the Zernike polynomials in the wavefront as [165]:

$$\phi(r, \theta) = \sum_{i=2}^{\infty} z_i Z_i\left(\frac{r}{R}, \theta\right) \quad (2.30)$$

where z_i is the coefficient associated with the i th Zernike polynomial. The Zernike coefficients can be recovered from a given phase screen, using the following equation [143]:

$$z_i = \frac{1}{R^2} \int \mathcal{P}(r/R) \phi(r, \theta) Z_i(r/R, \theta) d^2r \quad (2.31)$$

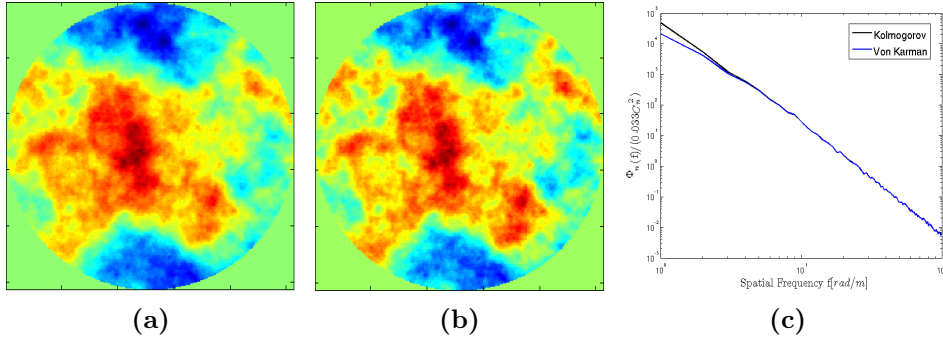


Figure 2.4: Fourier representation of a turbulent phase using: (a) Kolmogorov power spectrum (b) Von Karman power spectrum (c) PSD comparison of (a) and (b).

where $\mathcal{P}(r/R)$ is the characteristic function of the unitary disk [167]. A typical example of the realization of a phase screen with increasing number of Zernike polynomials is shown Fig 2.3.

2.5.2 Fourier based representation of the phase screen

This method, proposed by B. McGlamery [134, 141] in 1976, is widely accepted due to its simplicity and speed. The analysis of atmospheric turbulence is based on the assumption that atmospheric turbulence follows a Kolmogorov spectrum and has a phase whose frequency is uniformly, randomly distributed over the interval $-\pi$ to π [134, 108]. A phase can be statistically described by means of its power spectrum (described in section 2.2.2). The phase screen is obtained by the inverse Fourier transform of the product of a complex array of Gaussian random numbers and the square root of the phase spectrum [134, 44](Kolmogorov spectrum or the Von Karman spectrum). A typical example of Fourier generated phase screen is shown in Fig 2.4.

Although simple and computationally efficient, this method suffers from certain drawbacks. The model suffers from periodicity and the low frequency components are not well represented in this technique [9]. Solutions, however, exist to digitally enhance the low frequencies by the addition of subharmonics [108, 182].

§ 2.6 CONCLUSION

In this chapter, we have recalled the statistical descriptors of atmospheric turbulence. The effects of turbulence creates a distortion in the planar wavefront from outer space thereby resulting in a phase distortion in the wavefront. The knowledge of the statistical descriptors then helps to measure the effects of turbulence on the wavefront phase and also the blurring effects in ground-based image formation of astronomical objects. As a result, astronomers are able to recover a distorted wavefront or restore a blurred image, to a large-extent, given this statistical information of turbulence. It is also possible to simulate a turbulent phase, with the *a priori* knowledge of these descriptors, which is very important for experimental and validation purposes in ground-based astronomy. In this matter, the Zernike polynomials plays a useful role in representing an atmospherically distorted phase screen. Numerous other methods also exist, that are well known for their simplicity and speed: The Fourier based phase generation techniques using the power spectrum descriptor knowledge of turbulence are, however, widely preferred due to their simplicity and speed. In the next chapter, we will focus on the principle of operation of an AO system and the techniques it employ for estimating the distorted phase of a wavefront.

- CHAPTER 3 -

ADAPTIVE OPTICS AND WAVEFRONT RECONSTRUCTION

Turbulence in the Earth's atmosphere leads to a distortion in the planar wavefront from outer space resulting in a phase error. This phase error is responsible for the refractive blurring of images accounting to the loss in spatial resolution power of ground-based telescopes. Adaptive Optics (AO) is an opto-mechanical system that helps to remove this phase error, in real time, introduced in the wavefront due to atmospheric turbulence. In AO systems, an estimate of the phase error, or simply the phase, is obtained from the gradient measurements of the wavefront collected by a wavefront sensor. The correction estimate is then passed through a servo-control loop to a deformable mirror which deforms itself to adapt to the incident wavefront (on the telescope pupil) to correct and obtain an output plane wavefront.

The chapter is organized as follows: in section 3.1, we introduce the principal components and their functions in the AO system, in section 3.2 we discuss about the classical wavefront phase reconstruction techniques in AO, where in section 3.2.4, we talk about the inverse problem approach in wavefront phase reconstruction. Conclusion follows in section 3.3.

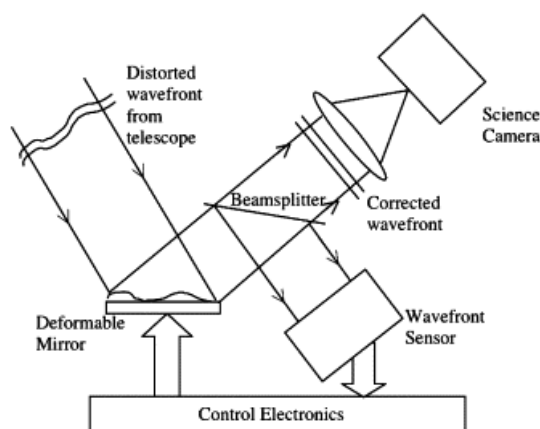


Figure 3.1: Schematic representation of an Adaptive Optics system (Courtesy: J. Vallerga [204]).

§ 3.1 THE ADAPTIVE OPTICS SYSTEM

An AO system is made up of three key elements [65, 164]. They are:

- the **deformable mirror** (DM) that changes its shape to fit to the incident wavefront,
- the **wavefront sensor** (WFS) that measure the wavefront distortions caused due to atmospheric turbulence,
- and the **controller** that generate the control signals to drive the DM based on the measurements provided by the WFS.

A schematic representation of an AO system is shown in Fig 3.1. We will summarize the operation of each of these elements in the following sections.

3.1.1 Deformable mirrors

The wavefront compensation in an AO system is physically performed by the DMs [158]. Depending on the type of AO system, the number of DMs can vary from one to many. For example, in SCAO and GLAO systems, only one DM is used whereas in MCAO systems, two to three DMs are incorporated. The movement of the DM, or in other words the change in the

shape of its surface is the result in the orientation of a continuous reflective facesheet which is deformed by a set of actuators glued to the back of it. The actuators expand or contract in length with the application of voltage signals, thereby pushing or pulling the mirror to deform its shape. The actuators are generally made of piezoelectric material (PZT) or Lead magnesium niobate (PMN). Many different technologies exist for the development of the DMs, the most common among them are the Stacked array mirrors (SAMs) [97, 161], Bimorph deformable mirrors [163], Micro deformable mirrors (or MEMS) [149, 220] and Voice coil deformable mirrors [8, 159]. A complete review of different types of DM technologies can be found in [181].

Irrespective of the technology used for the DM, the correction principle is always the same. When the perturbed wavefront arrives on the telescope pupil, the reflective facesheet of the deformable mirror is deformed to fit to the wavefront, and corrects the phase error introduced by the turbulence. The whole procedure of wavefront compensation can be summarized as:

$$\phi_{res}(r, \theta) = \phi_{turb}(r, \theta) - \phi_{cor}(r, \theta) \quad (3.1)$$

where $\phi_{res}(r, \theta)$ is the residual phase (tends to zero with the AO correction) and $\phi_{cor}(r, \theta)$ corresponds to the phase obtained by the mirror deformation (correction by AO).

3.1.2 Wavefront sensors

Wavefront sensors (WFS) are the measuring devices of an AO system that are capable of recording the wavefront distortion in terms of slope measurements or curvature measurements, depending on the type of WFS used. The Shack-Hartmann (SH) WFS works on the principle of measuring the local slope of the wavefront i.e. the spatial first derivatives (gradients) [164]. The curvature WFS, proposed by F. Roddier [163], measures the second derivative of the phase (Laplacian) of the incoming wavefront. The curvature WFS finds its application generally with bimorph DMs in curvature SCAO systems [158].

The SH WFS, designed by J. F. Hartmann [85] in 1900 and later modified by R. Shack [183] in 1960, is the most popular WFS used in AO systems. In this thesis, the proposed wavefront phase estimation algorithm will be based on the slope measurement technique of the SH sensor.

3.1.2.1 Shack-Hartmann wavefront sensor

A Shack-Hartmann wavefront sensor is used to measure the slope of an incoming wavefront. In a SH sensor, an array of lenses (also called a lenslet array) is placed in a conjugate pupil plane at the entrance of the telescope. Each lenslet covers a small part of the aperture (or pupil), the area covered is known as the sub-aperture area. A wavefront incident on the telescope pupil, is sampled by these lenslets and an image of the source is formed on a detector¹, placed in the focal plane of the lenslet array. When the wavefront is plane, each lenslet forms an image of the object (source) at its focus. But, in general, due to turbulence when the wavefront gets distorted, each lenslet sees a tilted version of the wavefront and the corresponding images are shifted from their reference position [137, 173, 170]. This shift in position is proportional to the mean slope of the wavefront and therefore can be measured [170]. The centroids (x_c, y_c) of the displaced spot are proportional to the gradient of $\phi(r)$ averaged over the sub-aperture area S [193, 65, 170], and can be written as:

$$x_c = \frac{f_l \lambda}{2\pi S} \int_S \frac{\partial \phi}{\partial x} dx dy + n_x \quad (3.2)$$

$$y_c = \frac{f_l \lambda}{2\pi S} \int_S \frac{\partial \phi}{\partial y} dx dy + n_y \quad (3.3)$$

where λ is the central wavelength of the detector and f_l is the focal length of the lenslet. n_x and n_y takes into account any type of noise associated with the WFS measurements. The principle of operation of SH WFS is shown in Fig 3.2.

The measurement noise for SH type WFS is due to the contribution of the photon noise and the detector noise. Every image formed on a detector is a percentage of the amount of photons (generally 50-80% that are converted to electrons) [193] received by a lenslet, and the noise associated with the incoming flux of photons from the source is known as the photon noise. An expression for the photon noise variance (σ_{ph}^2) and detector noise variance

¹The detector can be a four quadrant detector for each sub-aperture or a charged-coupled device (CCD) [164].

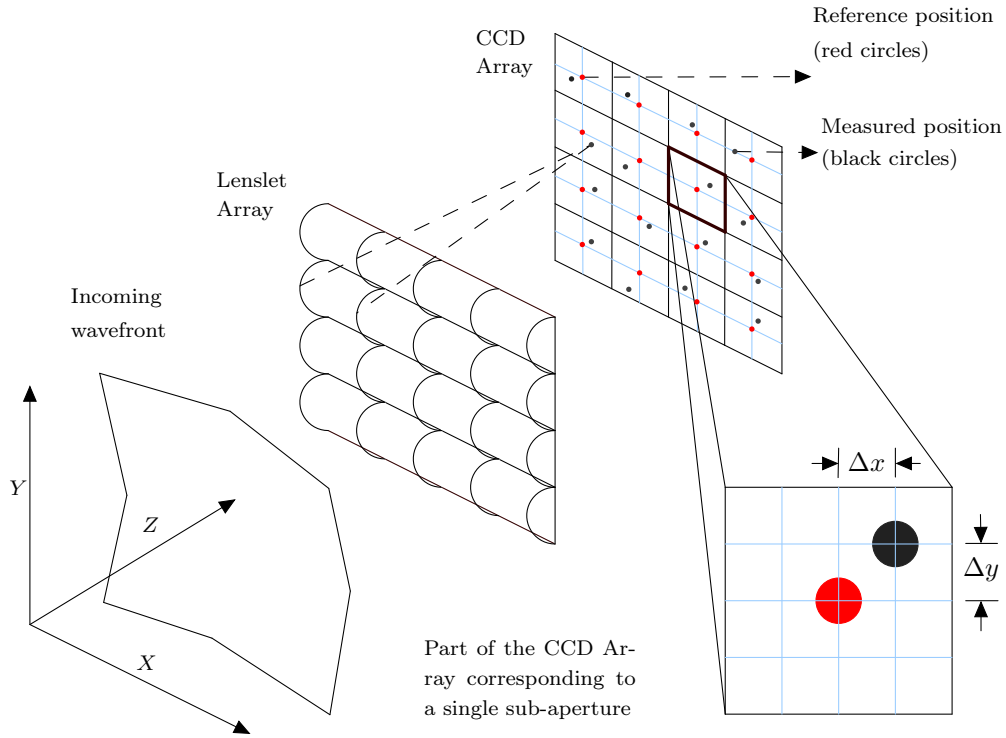


Figure 3.2: Schematic representation of a Shack-Hartmann wavefront sensor. An incident wavefront travelling along the Z -axis, after entering the telescope pupil, is sampled by an array of lenses (called lenslet array), and forms an image of the source on the CCD array. If the wavefront is plane, each lenslet forms an image of the source at its focus (marked by red). If the wavefront is distorted, the images are shifted from their reference position (marked by black). This shift in position is proportional to the mean slope of the wavefront and can be measured with equation (3.2) and equation (3.3).

(σ_{det}^2) is given by [170]:

$$\sigma_{ph}^2 = \frac{\pi^2}{2} \frac{1}{n_{ph}} \left(\frac{X_T}{X_D} \right)^2 \quad (rad^2) \quad (3.4)$$

$$\sigma_{det}^2 = \frac{\pi^2}{3} \frac{\sigma_{e^-}^2}{n_{ph}^2} \left(\frac{X_S^2}{X_D} \right)^2 \quad (rad^2) \quad (3.5)$$

where n_{ph} is the number of photons received per sub-aperture, X_T is the size of the image formed on a sub-aperture, X_D is the diffraction-limited size of the image formed on a sub-aperture, X_S^2 is the total number of pixels used in calculating the position of the image formed on a sub-aperture and σ_e is the rms value of electron noise per pixel and per sub-aperture.

3.1.3 The controller

The purpose of the controller, in an AO system, is to minimize the phase variance of the observed wavefront [166]. Given the measurements of the WFS, the objective of the controller is to control the movement of the deformable mirror to obtain the best possible correction phase ϕ_{corr} (see equation (3.1)). The WFS provides a vector of measurements M , corresponding to the sampling of the wavefront by sub-apertures. From these M measurements, the controller generates N corrected signals (corresponding to N corrected phase values over the detector) of the wavefront [164, 166]. These signals are then applied as high voltages (after passing through Digital-to-Analog converters) to the actuators beneath the DM. The actuators then push or pull the DM to update the shape of the mirror according to the wavefront.

The optimal correction of the wavefront phase by the controller depends not only on the WFS measurements, but also on the different temporal aspects of the control loop [65], which must be taken into consideration. A good source of information on the temporal aspects of the controller can be found in [34, 46, 53, 122]. Some examples of AO correction of spatial images are shown in Fig 3.3.

After discussing about the functioning of an AO system and its key elements, we will now focus on the problem of wavefront reconstruction from the measurements of the WFS.

§ 3.2 WAVEFRONT RECONSTRUCTION

The goal of any AO system is to reconstruct the wavefront phase values from the discrete measurement of its gradients (slope measurements) or Laplacian provided by the wavefront sensor. The problem of reconstruction can also be

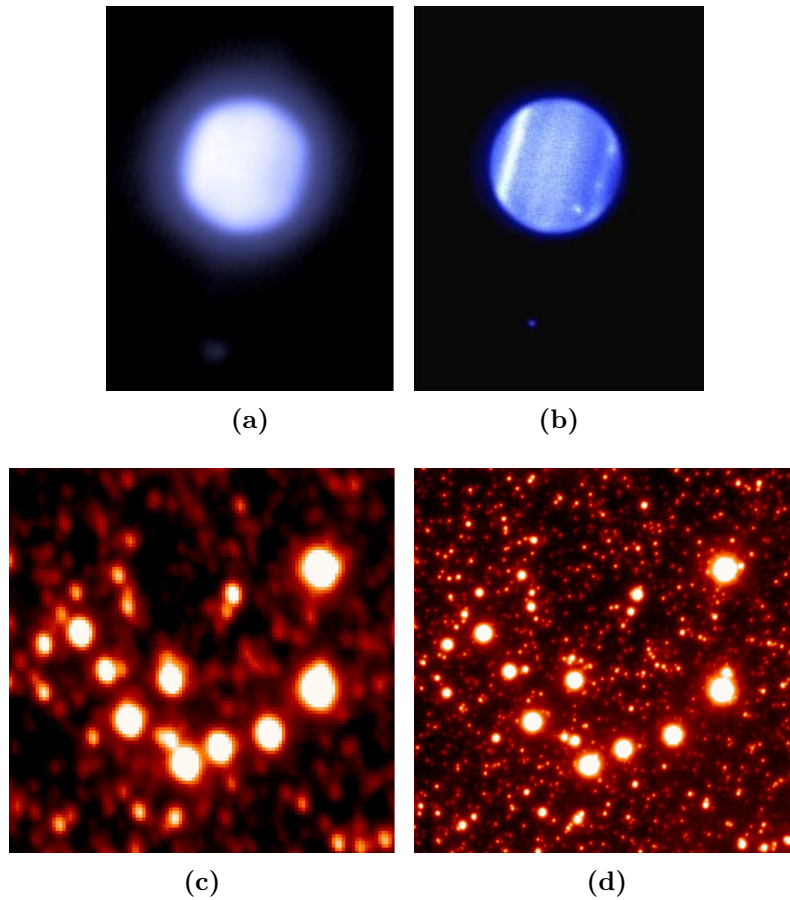


Figure 3.3: *AO correction of astronomical images. Top row : H-band image of Uranus and the moon Miranda (faint point at the bottom) captured using ground-layer adaptive optics system (GLAS). (a) Uncorrected image. (b) with AO correction. Image courtesy: Isaac Newton Group of Telescopes. Bottom row : 20×20 arcsecond region near the center of the globular cluster Omega Centauri. (c) without AO correction. (d) with MCAO correction. Image courtesy: Enrico Marchetti.*

viewed as a surface reconstruction approach from a given gradient field [164]. The slope measurements obtained from a SH sensor are a measure of the wavefront phase difference in two directions: the x direction and the y direction. Depending on the way of measurement of the wavefront shape in the optical pupil, the phase reconstruction process can be viewed either as a

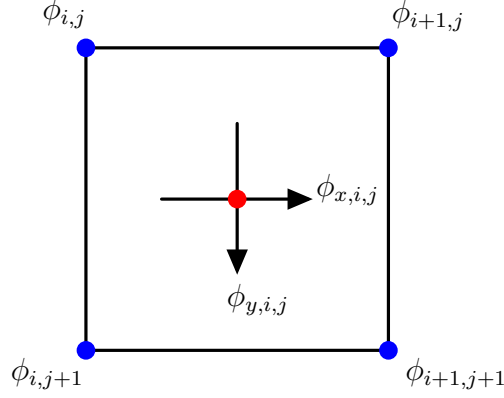


Figure 3.4: *Fried Geometry for the (i, j) th sub-aperture. A measurement of the gradient of the phase is provided by a wavefront sensor at (x_i, y_j) . The phase values at the corners of the sub-aperture are then estimated.*

zonal approach or a modal approach [186].

3.2.1 The Zonal approach

In the zonal approach, the wavefront phase ϕ is expressed as a discrete set of points determined by each zone (or sub-aperture) of the mirror responding to the incident wavefront on the telescope pupil and let Φ be a vector of this discretized phase values that we are searching for. The relation between the slope measurements of the wavefront sensor g and the unknown Φ can be generalized into a linear equation of matrix framework [18, 164, 193] as:

$$g = \Gamma\Phi + n \quad (3.6)$$

where Γ is the discrete differential operator, also known as the *interaction matrix*, and $n \sim \mathcal{N}(0, \sigma^2 I)$ is the noise vector. It should be noted here that the measurement g corresponds to a sampled version of the derivative of the phase, which results in g being corrupted by an overlapping error. As a result, a periodization is introduced in its spectrum in the Fourier domain [65]. Depending on the shape of the spectrum and the sampling rate, some error will therefore remain in the low frequency components of the phase.

Some well-known geometrical models exist that are able to express the discrete measurements g (assumed to be centered within each sub-aperture) in terms of the phase values at the four corners of a sub-aperture in the wavefront sensor [62, 88] (i, j being the co-ordinates of the sub-aperture considered). According to Fried geometry [62] (see Fig 3.4), the phase gradients at (x_i, y_j) can be expressed, in its two directions x and y as [164]:

$$\phi_{x,i,j} \approx \frac{1}{2}[(\phi_{i+1,j+1} + \phi_{i+1,j}) - (\phi_{i,j} + \phi_{i,j+1})] \quad (3.7)$$

$$\phi_{y,i,j} \approx \frac{1}{2}[(\phi_{i+1,j+1} + \phi_{i,j+1}) - (\phi_{i,j} + \phi_{i+1,j})] \quad (3.8)$$

where the grid spacing is assumed to be 1. If the unknown Φ is a vector of N phase values (or N command signals applied to the actuators in the DM through the controller) over a grid and the measurement vector g consists of M elements, then the interaction matrix Γ is a $N \times M$ matrix and describes the response of the WFS to each actuator [164, 166].

3.2.2 The Modal approach

In the modal approach, the wavefront phase is expressed in terms of polynomial expansion of some basis functions Z_i , also called modes (can be Zernike or KL modes). The objective is then to calculate the coefficients of Z_i from which the phase can be reconstructed [164] using the equation (see section 2.4):

$$\phi(r, \theta) = \sum_i z_i Z_i(\kappa, \theta) \quad (3.9)$$

where z_i are the coefficients of Z_i . Taking the derivatives on both sides of the equation (3.9), we obtain a set of equations that can be expressed in the matrix framework as:

$$s = cA \quad (3.10)$$

where s is the array containing the slope measurements of the wavefront sensor and $A = \{z_2, z_3, \dots, z_n\}$ (first mode or piston mode removed). The derivatives of the modes in the two directions are expressed as [164, 65]:

$$c_{ij}^x = \frac{f}{S} \int_{subap\ j} \frac{\partial Z_i}{\partial x} dx dy \quad \text{and} \quad c_{ij}^y = \frac{f}{S} \int_{subap\ j} \frac{\partial Z_i}{\partial y} dx dy \quad (3.11)$$

where f is the focal length of the lenslet array, i represents the mode number, j the number of sub-apertures and S represents the area of the sub-aperture.

3.2.3 Least squares wavefront reconstruction

A general approach to estimate the phase is to minimize the least squares error function given by:

$$\operatorname{argmin}_{\Phi} \|\Gamma\Phi - \mathbf{g}\|_2^2 \quad (3.12)$$

The solution to this function can be, for the zonal approach, written as:

$$\Gamma^T \Gamma \Phi = \Gamma^T \mathbf{g} \quad (3.13)$$

and, for the modal approach, as:

$$\mathbf{c}^T \mathbf{c} \mathbf{A} = \mathbf{c}^T \mathbf{s} \quad (3.14)$$

where Γ^T is the transpose of Γ . It should be noted that, the ground matrix $\Gamma^T \Gamma$ (or $\mathbf{c}^T \mathbf{c}$) should be well-conditioned [137, 65, 164] to verify the standard solution of equation (3.13) (or equation (3.14)).

Equation (3.13) (or equation (3.14)) can also be viewed as a discrete Poisson equation with Neumann boundary conditions [86, 144, 164]. So, surface reconstruction techniques based on solving the Poisson equation can also be used for reconstructing the phase. A general discussion on different surface reconstruction methods can be found in section 5.3.1, Chapter 5.

3.2.4 Wavefront reconstruction as an inverse problem

The wavefront reconstruction can also be viewed as an inverse problem [137, 164], where one searches for the unknown Φ in the equation $\mathbf{g} = \Gamma\Phi + \mathbf{n}$. An estimate the wavefront phase $\hat{\Phi}$ from the slope measurements can be written as:

$$\hat{\Phi} = \mathbf{B}\mathbf{g} \quad (3.15)$$

where \mathbf{B} is known as the *reconstruction matrix*.

Most of the existing methods for solving the inverse problem can be broadly classified into two types: the maximum likelihood (ML) technique and the maximum *a posteriori* (MAP) technique [98, 164].

3.2.4.1 Maximum likelihood method

The ML method tries to determine the unknown Φ such that it maximizes the probability of producing the measurement vector \mathbf{g} . In other words, it tries to maximise the probability $P(\mathbf{g}|\hat{\Phi})$ and we can write [137, 110]:

$$P(\mathbf{g}|\hat{\Phi}) \propto \exp\left\{-\frac{1}{2}(\Gamma\hat{\Phi} - \mathbf{g})^T C_n^{-1}(\Gamma\hat{\Phi} - \mathbf{g})\right\} \quad (3.16)$$

where C_n is the covariance matrix of the noise \mathbf{n} whose statistics are assumed to be known. To find the maximum of equation (3.16), we take the derivative of its logarithm and equate it to zero [164, 110]:

$$\frac{\partial}{\partial \hat{\Phi}} \ln(P(\mathbf{g}|\hat{\Phi})) = 0 \quad (3.17)$$

The resulting solution is rearranged to give an estimate of the phase as [177]:

$$\hat{\Phi} = (\Gamma^T C_n^{-1} \Gamma)^{-1} \Gamma^T C_n^{-1} \mathbf{g} \quad (3.18)$$

and the reconstruction matrix has the form:

$$\mathbf{B} = (\Gamma^T C_n^{-1} \Gamma)^{-1} \Gamma^T C_n^{-1} \quad (3.19)$$

Equation (3.18) is known as the maximum likelihood estimate of the phase Φ . The invertibility of the matrix $\Gamma^T C_n^{-1} \Gamma$, should however be checked in all circumstances. If $M \geq N$ there is generally no problem, but the matrix can be ill-conditioned. But in general $M < N$. In this case the matrix Γ has $N-M$ null eigenvalues, and thus can not be directly invertible. The classical solution consists in setting the eigenvalues associated to this subspace to 0. In other words, the solution is projected into a subspace of dimension M . In the case of Fourier transform (deconvolution, aperture synthesis) the solution is commonly known as the Bracewell solution [36, 35].

If the statistics of the noise is not known, C_n is assumed to be equal to \mathbf{I} , where \mathbf{I} is the identity matrix [110]. In this case, the maximum likelihood solution of equation (3.18) reduces to the least squares solution.

3.2.4.2 Maximum *a posteriori* method

Unlike the ML method, which tries to estimate the unknown phase Φ without any *a priori* knowledge of it, the MAP estimator works on the idea of including any available information of Φ in the solution process. This corresponds

to including a regularization criteria in the solution process of this ill-posed inverse problem, where there are less data than unknowns. The separation between ML and MAP can therefore be foreseen from this applied criterion.

The idea is, given the measured data \mathbf{g} and some *a priori* information of Φ , the MAP estimator tries to maximize the probability $P(\hat{\Phi}|\mathbf{g})$. From Bayes' theorem we can say:

$$P(\hat{\Phi}|\mathbf{g}) \propto P(\mathbf{g}|\hat{\Phi}) \times P(\hat{\Phi}) \quad (3.20)$$

where $P(\mathbf{g}|\hat{\Phi})$ is the conditional *a priori* probability and $P(\hat{\Phi})$ is the prior probability on Φ . We assume that Φ is Gaussianly distributed with a known covariance matrix C_Φ . We therefore have:

$$P(\hat{\Phi}|\mathbf{g}) \propto \exp\left\{-\frac{1}{2}(\Gamma\hat{\Phi} - \mathbf{g})^T C_n^{-1}(\Gamma\hat{\Phi} - \mathbf{g})\right\} \times \exp\left\{-\frac{1}{2}\Phi^T C_\Phi^{-1}\Phi\right\} \quad (3.21)$$

The resulting solution is obtained by minimizing the logarithm of $P(\hat{\Phi}|\mathbf{g})$ [164, 177, 63] and can be written as:

$$\hat{\Phi} = (\Gamma^T C_n^{-1} \Gamma + C_\Phi^{-1})^{-1} \Gamma^T C_n^{-1} \mathbf{g} \quad (3.22)$$

3.2.4.3 Minimum variance wavefront reconstruction

The minimum variance wavefront reconstruction is generally preferred over the least squares method as the latter is unstable for large scale AO systems. The minimum variance estimator tries to minimize the statistical average of the wavefront phase residual error ϵ and can be written as:

$$\epsilon = \langle \|\hat{\Phi} - \Phi\|^2 \rangle = \langle \|\mathbf{B}\mathbf{g} - \Phi\|^2 \rangle \quad (3.23)$$

The main goal of the minimization procedure is to determine the reconstruction matrix \mathbf{B} such that ϵ is minimum [164]. The final solution leads to [18, 65]:

$$\mathbf{B} = (\Gamma^T \Gamma + \sigma^2 C_\Phi^{-1})^{-1} \Gamma^T \quad (3.24)$$

and the estimated phase as:

$$\hat{\Phi} = (\Gamma^T \Gamma + \sigma^2 C_\Phi^{-1})^{-1} \Gamma^T \mathbf{g} \quad (3.25)$$

This solution is equivalent to the MAP solution of equation (3.22), when the statistics of noise is not known and C_n is assumed to be equal to I. Noise statistics are then assumed to be Gaussian, and the solution is equivalent to the inversion with a Wiener filter.

There are many different approaches to solving equation (3.25) that has been of major interest in recent years. A direct method using sparse matrix technique has been proposed in [54]. Multigrid techniques and precondition conjugate gradient methods [75, 74, 18] have, however, proven to be the most computationally efficient approaches.

§ 3.3 CONCLUSION

In this chapter, we have presented a summary on the basic principle of operation of an AO system and the techniques employed in the wavefront phase reconstruction from the slope measurements (or curvature measurements) of a wavefront sensor. We have talked about the operation of the SH WFS, which is the most widely used WFS in AO. The reconstruction principle is based on solving the least squares inverse problems. Multigrid solvers and precondition conjugate gradient solvers have proved to be the most computationally efficient approaches to this problem. In the next chapter, we introduce the framework of MMF (Microcanonical Multiscale Formalism) based on which we formulate our phase reconstruction algorithm.

- CHAPTER 4 -

THE MICROCANONICAL MULTISCALE FORMALISM (MMF)

After having recalled in the previous chapter an overview of existing main AO solution methods, we now turn to the necessary description of the formalism used in deriving a new approach to phase reconstruction through inference across the scales. In this chapter, we delve into the formalism used to achieve this goal: the MMF. The MMF is a specific microcanonical approach to multifractality. It allows the determination of the geometrical sets, unattainable by linear filtering techniques, that describe the cascading properties of intensive variables and the localization on information content in turbulent signals. These sets, which form the basis of multifractal or multiscale hierarchy in turbulence, are determined by the computation of singularity exponents in a microcanonical formulation. As inference across the scales will be achieved in chapter 6 by a multiresolution analysis performed on the signal of singularity exponents, this chapter gives the foundation of the key relevant quantities used in our thesis. We also recall the more classical approaches to multifractality devised in physics (canonical setting) to ease the understanding between the different introductions to this subject.

Most real-world signals are complex signals, usually difficult to describe but possess a high degree of redundancy [197]. The underlying dynamics of such systems are such that, at the macroscopic scale, intensive variables display a power-law in the vicinity of a critical point [203], the corresponding

exponent being called a critical exponent, or, as it is usual in the multifractal formalism, a singularity exponent. The distribution of the singularity exponents define a universality class : if two different systems have identical distribution of their singularity exponents, all the macroscopic quantities and correlation functions that can be derived from their generalized phase space will be equivalent i.e., these systems will share common macroscopic features. This implies the presence of a common macroscopic behaviour independent of the microscopic dynamics of each system [119] which is one of the basic justifications for the science of complex systems. The knowledge of localized singularity exponents allow the retrieval of classical characteristics in the multifractal formalism, such as the singularity spectrum, as computed through a Legendre transform in the canonical approach to multifractality. But the knowledge of localized singularity exponents goes much further in the characterization of the dynamics of a complex system. For example in the case of FDT (Fully Developed Turbulence), the multiscale hierarchy, whose singularity spectrum is a well known signature, can be computed from the localized singularity exponents. In the canonical approach to multifractality, developed by researchers since many years, the characteristic shape of the singularity spectrum is only an indicator of the presence of a multiscale hierarchy. The effective computation of the singularity spectrum in a canonical setting, for instance in relation with wavelet modulus maxima, remains a computationally demanding problem. This makes the MMF particularly interesting, because this formalism allows a direct computation of the localized singularity exponents, hence a direct access of the multiscale hierarchy whose existence goes back to the work of G. Parisi and U. Frisch [147] and Z. S. She and E. Leveque [185]. The same type of conclusion can be inferred from multiscale analysis of most complex signals [201]. As a consequence, the paradigm of understanding natural signals as acquisitions of complex systems with unknown phase space is a useful one [32]. The properties of physical cascading variables reflect the transfer of energy, or more generally information, taking place from larger scales to smaller ones. The MMF proves to be a suitable approach for the study of multiscale properties in real signals. Recent developments in microcanonical framework for the computation of **singularity exponents** and the derivation of singularity spectra have lead

to a sensible improvement in the numerical techniques for the determination of multiscale characteristics of real signals [154, 202]. Experimental analysis on different real-world signals, ranging from stock market time series to atmospheric perturbed optical phase shows that these systems are not only found to have multiscale behaviour, but their singularity spectra are also coincident [154]. Consequently, the precise numerical computation of geometrically localized singularity exponents in single acquisitions of complex systems, without the averages taken on grand ensembles, unveils the determination of their universality class [151].

Before getting into the theory of MMF, it is imperative to discuss the concept of *fractals*. Fractal geometry constitutes an important part of this formalism as they also exhibit scale-invariant phenomenon, although multifractal systems are more flexible in describing the scale-invariant nature of natural signals. A typical example of a fractal set is the *von Koch* curve shown in Fig 4.1.

The chapter is organized as follows: In section 4.1, we introduce the concept of fractals and fractal dimension, in section 4.2 we describe a multifractal system, where in section 4.2.2 we introduce the concept of MMF. In section 4.3 we discuss ways of estimating the singularity exponents and conclude in section 4.4.

§ 4.1 THE CONCEPT OF FRACTALS

The term fractal was introduced by Mandelbrot [131] to describe objects that exhibit an aspect of extreme irregularity and does not possess any length-scale characteristics [7]; they have been used as a standard strategy to describe self-similar systems [154]. The degree of irregularity in fractal sets can be realized with the help of their *fractal dimension*, proposed by Hausdorff in 1919. A fractal object is characterized by its fractal dimension and the fractal dimension of a set can be calculated in many ways. The different methods of computing it, however, may give different values of dimension for the same set. The most accepted methods for calculating the fractal dimensions are the *Box-counting dimension* and the *Hausdorff dimension*.

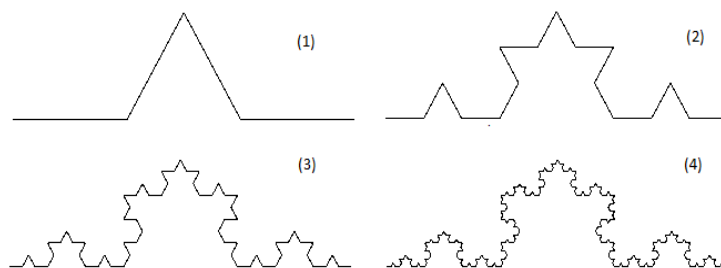


Figure 4.1: *The sequence of sets approaching the von Koch curve after 1, 2, 3 and 4 iterations.*

4.1.1 Box-counting dimension

The Box-counting dimension is a way of determining the fractal dimension of a given set. Let X be a non-empty, bounded subset of \mathbb{R}^n and $N(s)$ be the least number of closed balls of diameter s required to cover X , then, by definition, the Box-dimension of the set X is:

$$\dim_B(X) = \lim_{s \rightarrow 0} \sup \frac{\log N(s)}{\log(1/s)} \quad (4.1)$$

Due to its simplicity and convenience to estimate in practice [55], the Box-counting dimension (also known as the Minkowski–Bouligand dimension) is one of the most widely used fractal dimensions.

4.1.2 Hausdorff dimension

Another definition of the concept of dimension, called Hausdorff dimension, is defined as follows: for a subset X of \mathbb{R}^n and $\delta > 0$, we consider a countable collection of sets (U_i) required to cover X , then the δ -dimensional Hausdorff measure $H^\delta(X)$ of X can be expressed as:

$$H^\delta(X) = \lim_{s \rightarrow 0} \inf_{U_i} \sum_i \text{diam}(U_i)^\delta \quad (4.2)$$

The δ -dimensional Hausdorff measure of X is therefore estimated as the sum of the $\text{diam}(U_i)^\delta$, with the infimum taken over all the countable collections (U_i) , such that $\text{diam}(U_i) < s$ [178]. The Hausdorff dimension of X , $\dim_H(X)$

is then defined as:

$$\dim_H(X) = \inf\{\delta \mid H^\delta(X) = 0\} \quad (4.3)$$

The Hausdorff dimension for a fractal set, in practice, is however difficult to be estimated by computational methods [19, 55] and although it is mathematically more satisfactory than the Box-dimension, in practical applications we prefer to use the latter. However, in MMF we estimate the Hausdorff dimension as Box-counting dimension is not well defined.

§ 4.2 DESCRIPTION OF A MULTIFRACTAL SYSTEM

Similar to the fractals, a multifractal system is also a scale-free (scale invariant) system i.e. the smaller regions exhibit the same statistical properties as that of the whole system: they are statistically self-similar [154]. A multifractal system is characterized by the distribution of Hausdorff dimensions to describe its behaviour under changes of scale. The first attempt to exploit the organizational behaviour of a multifractal system, and relate it with a cascade process, was the Canonical Multiscale Formalism (CMF) [203].

4.2.1 Canonical approach to multifractals

According to Canonical Formulations (CMF), a signal s is multifractal if for a given family of functions Γ_r we have:

$$\langle |\Gamma_r s|^p \rangle = \alpha_p r^{\tau_p} + o(r^{\tau_p}) (r \rightarrow 0) \quad (4.4)$$

where $\langle \cdot \rangle$ denotes the average over an ensemble of signals s belongs to (α_p depends on the functional Γ_r) [203]. However, in general, such averages are inaccessible. Instead, the average for different points \vec{x} within the same signal domain, as the one of s , is calculated (ergodic assumption).

The existence of multiplicative cascade process was first justified by Kolmogorov in his theory on turbulence [64]. Under conditions of intense turbulence (fully developed turbulence), energy is passed down from the large-scales to the smaller ones by an injection process until the fluid attains a state

of dynamic equilibrium where we can expect a balance in the amount of energy stored in each scale. Kolmogorov proposed that for two given scales r and L , $0 < r < L$, we can define the process of energy transfer by the injection parameter $\eta_{r/L}$ as:

$$\Gamma_r s \doteq \eta_{r/L} \Gamma_L s \quad (4.5)$$

where ‘ \doteq ’ means that both sides are equally distributed. According to Kolmogorov, the injection process $\eta_{r/L}$ depends only on the ratio of the scales and can be written as $\eta_{r/L} = [r/L]^\epsilon$. From this we can say that the p -order moments have the following relationship

$$\langle |\Gamma_r s|^p \rangle = [r/L]^{\epsilon p} \langle |\Gamma_L s|^p \rangle = A_p r^{\epsilon p} \quad (4.6)$$

where $A_p = \langle |\Gamma_L s|^p \rangle L^{-\epsilon p}$. Comparing the equation (4.4) and equation (4.6), we can say that $\tau_p = \epsilon p$, that is, the canonical exponents τ_p have a linear relationship with p ; a condition known as *normal scaling* [203] and the system is monofractal. However, experiments show that in the case of fully developed turbulence (FDT), the relationship between τ_p and p is not linear, rather it is a convex curve, a condition known as *anomalous scaling* [202]. To apply Kolmogorov’s decomposition in anomalous scaling, certain assumptions have to be made:

- $\eta_{r/L}$ has to be interpreted as a random variable, independent of L .
- The variable $\eta_{r/L}$ has to be indefinitely divisible to ensure downward process from scale L to r is verified directly or in several stages giving rise to the cascade process.

It has been verified [64] that an injection mechanism as the one proposed by Kolmogorov leads to the understanding of a underlying geometrical structure in a multiplicative cascade process, together with the knowledge of the exponents τ_p , for inferring information along the scales of the signal. This description of self-similarity led researchers to propose tractable models for the determination of the geometric multiscale hierarchy. The Microcanonical Multiscale Formalism allows this determination by localized singularity exponents, contemplated in a microcanonical formulation and without ergodic hypothesis.

4.2.2 Microcanonical approach to multifractals (MMF)

In equation (4.4) the exponents τ_p are not geometrically localized, because of the use of average over ensembles. The microcanonical approach (MMF) proposes to overcome this limitation by introducing localized versions of the exponents, while providing effective means to compute them without stationarity hypothesis. We will say that a signal s is multifractal in a microcanonical sense if, for at least one functional Γ_r depending on the scale r , it is assumed that for any point \vec{x} the following equation holds [202]:

$$\Gamma_r s(\vec{x}) = \alpha(\vec{x}) r^{h(\vec{x})} + o(r^{h(\vec{x})}) \quad (r \rightarrow 0) \quad (4.7)$$

The exponent $h(\vec{x})$, which is a function of the point \vec{x} , is called the *singularity exponent* or *Local predictability exponent (LPE)* at point \vec{x} [202]. This is the microcanonical approach to multifractal theory which says that a signal is multifractal if every point in the signal is characterized by a local power-law scaling behaviour. So, the two main quantities that define a multifractal signal are the singularity exponents and the collection of its fractal dimensions: the singularity spectrum.

4.2.2.1 Singularity exponents

According to MMF, a signal $s(\vec{x})$ is multifractal if it is characterized by an hierarchy of fractal components [154]. In fact, decomposing a multifractal signal results in partitioning the signal domain into components \mathcal{F}_h , which are in general of fractal nature. In other words, each point \vec{x} in the signal is characterized by a singularity exponent $h(\vec{x})$ which is typical to one component \mathcal{F}_h . The fractal components are level sets of the function $h(\vec{x})$ [203] and are defined as follows:

$$\mathcal{F}_h = \{\vec{x} : h(\vec{x}) = h\} \quad (4.8)$$

and the multifractal hierarchy is equivalently defined by the family $\mathcal{G}_h = \{\vec{x} : h(\vec{x}) \leq h\}$, which is such that when $h_1 < h_2$, $\mathcal{G}_{h_1} \subset \mathcal{G}_{h_2}$. The knowledge of the family \mathcal{G}_h and \mathcal{F}_h are equivalent, the multifractal hierarchy is usually referred to the family \mathcal{F}_h .

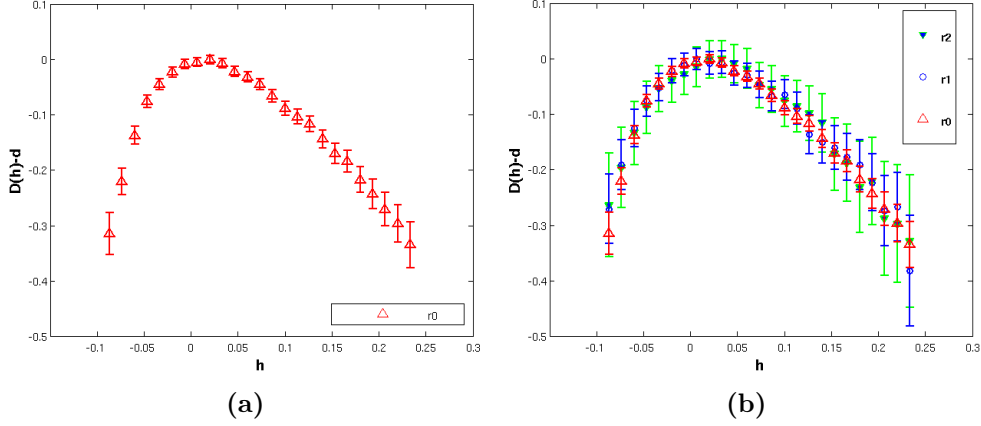


Figure 4.2: Singularity spectrum for the phase screen shown in Fig 2.3a. (a) Reduced singularity spectra $D(h) - d$ at the finest scale (resolution) r_0 . (b) Reduced singularity spectra $D(h) - d$, with errorbars, at the finest possible scale r_0 , twice the finest possible scale r_1 and three times the finest scale r_2 .

In practice, the sets \mathcal{F}_h are determined by the value of $h(\vec{x})$ not fixed, but belonging to an interval defined by a threshold Δh :

$$\mathcal{F}_h = \{\vec{x} : h(\vec{x}) \in]h - \Delta h, h + \Delta h[\} \quad (4.9)$$

The central problem is to compute at best possible numerical precision the value of $h(\vec{x})$ at point \vec{x} since bad approximations of singularity exponents lead to poor performances in signal processing applications.

4.2.2.2 Singularity spectrum

The singularity spectrum of a multifractal signal is the collection of all its fractal dimensions, i.e. the different Hausdorff dimensions $D(h)$ of the fractal components \mathcal{F}_h , represented as a function of h . The distribution of the singularity exponents has a simple relation with the singularity spectrum $D(h)$ at a given scale r . The empirical histogram of the exponents ($\rho_r(h)$) at small scale r verifies [203, 99]:

$$\rho_r(h) \propto r^{d-D(h)} \quad (4.10)$$

where d is the dimension of the signal domain. Henceforth, we can obtain $D(h)$ from the log-log regression of equation (4.10) as:

$$d - D(h) = \lim_{r \rightarrow 0} \frac{\log(\rho_r(h))}{\log r} \quad (4.11)$$

with, as stated, $r \rightarrow 0$. The process can however be numerically time consuming. One important aspect of the singularity spectrum is that, the maximum of the curve (obtained by the mapping of $D(h)$ as a function of h and is convex) corresponds to the fractal dimension of the support of the measure and is strictly positive [7]. This implies that there exists a fractal component \mathcal{F}_{h_1} of maximal fractal dimension $D(h_1) = d$, and we estimate the singularity spectrum at the finest resolution scale r_0 as [202, 203]:

$$D(h) = d - \frac{\log(\rho_{r_0}(h)/\rho_{r_0}(h_1))}{\log r_0} \quad (4.12)$$

where $\rho_{r_0}(h_1) = \max\{\rho_{r_0}(h)\}$.

4.2.3 Relation between canonical exponents τ_p and singularity spectrum $D(h)$

The canonical exponents τ_p can be computed from the Legendre transform of the singularity spectrum $D(h)$ by the simple relationship [147]:

$$\tau_p = \inf_h \{hp + d - D(h)\} \quad (4.13)$$

which is known as the Parisi-Frisch formula. One of the advantages of this formula is that it can be inverted. By definition, the Legendre spectrum $D_l(h)$ corresponds to the Legendre transform of τ_p [202]:

$$D_l(h) = \inf_p \{hp + d - \tau_p\} \quad (4.14)$$

where d stands for the dimension of the signal domain as before. By construction $D_l(h)$ is convex, and if not, the Legendre spectrum will equal its convex hull [202].

We will therefore summarize the MMF approach as follows: A signal $s(\vec{x})$ is multifractal in the microcanonical sense if it satisfies the following three conditions [203]:

1. there exists at least a family of functionals $\{\Gamma_r\}_r$ such that equation (4.7) is verified for every point \vec{x} in the signal.
2. at any scale r , equation (4.14) holds for the same curve $D_l(h)$.
3. the singularity spectrum $D_l(h)$ derived from equation (4.14) is a convex function of h .

The singularity spectrum of an experimental phase screen is shown in Fig 4.2. The same behaviour of the curve is observed for other phase screens also. The convex shape of the singularity spectra is the characteristic of the presence of a multiscale hierarchy in the signal defined by equation (4.8). The result shown in Fig 4.2 clearly indicates that the perturbed optical phase has multiscale properties, which justifies the use of MMF in exploiting its features.

We will now focus our attention on the computation of the singularity exponents $h(\vec{x})$. From this part onwards, we will be addressing the applications of MMF for the case of 2-D signals only, since the purpose of this thesis is to validate the MMF model on image processing applications in Adaptive Optics.

§ 4.3 ESTIMATING THE SINGULARITY EXPONENTS

Let I be a scalar image defined over a compact subset of \mathbb{R}^2 and $\|\nabla I\|$ is the norm of its gradient. We work with an additive normalization of $I(\vec{x})$ defined as [197] $I(\vec{x}) - \langle I \rangle$, where $\langle I \rangle$ is the average of luminance intensities over the signal domain. We then define a measure μ through its density $d\mu(\vec{x})$, so that the measure of a ball $\mathcal{B}_r(\vec{x})$ of radius r centered around the point \vec{x} corresponds to summing the norm of the gradient over $\mathcal{B}_r(\vec{x})$:

$$\mu(\mathcal{B}_r(\vec{x})) = \int_{\mathcal{B}_r(\vec{x})} d(\vec{y}) \|\nabla I\|(\vec{y}) \quad (4.15)$$

A measure μ as the one defined above is a multifractal measure, in a microcanonical sense, if for any point $\vec{x} \in \Omega$ the following equality holds [203]:

$$\mu(\mathcal{B}_r(\vec{x})) = \alpha(\vec{x}) r^{h(\vec{x})} + o(r^{h(\vec{x})}) \quad (r \rightarrow 0) \quad (4.16)$$

where $\alpha(\vec{x})$ is a signal-dependent amplitude prefactor and $h(\vec{x})$ is the singularity exponent at point \vec{x} . The singularity exponents for experimental, discretized data can be calculated using different methods [202, 155]. We will discuss about the two methods that has been widely popular for their simplicity and effectiveness.

4.3.1 Singularity analysis via log-log regression

A direct log-log regression of equation (4.16) gives an estimate of $h(\vec{x})$ as:

$$h(\vec{x}) = \lim_{r \rightarrow 0} \frac{\log(\mu(\mathcal{B}_r(\vec{x}))/\alpha(\vec{x}))}{\log(r)} \quad (4.17)$$

for a very small value of r , such that the term $o(r^{h(\vec{x})})$ of equation (4.16) is diminished. One can choose $\alpha(\vec{x})$ as the average of the norm of the gradients [202]. For multiple values of r , $r = \{r_0, r_1, \dots, r_n\}$, equation (4.17) can be written as:

$$\begin{aligned} \log(\mu(\mathcal{B}_{r_0}(\vec{x}))) &= \log(\alpha(\vec{x})) + h(\vec{x}) \log(r_0) \\ \log(\mu(\mathcal{B}_{r_1}(\vec{x}))) &= \log(\alpha(\vec{x})) + h(\vec{x}) \log(r_1) \\ \vdots &= \quad \quad \quad \vdots \quad + \quad \quad \quad \vdots \\ \log(\mu(\mathcal{B}_{r_n}(\vec{x}))) &= \log(\alpha(\vec{x})) + h(\vec{x}) \log(r_n) \end{aligned} \quad (4.18)$$

and can be expressed in the matrix framework as:

$$\underbrace{\begin{bmatrix} \log(\mu(\mathcal{B}_{r_0}(\vec{x}))) \\ \log(\mu(\mathcal{B}_{r_1}(\vec{x}))) \\ \vdots \\ \log(\mu(\mathcal{B}_{r_n}(\vec{x}))) \end{bmatrix}}_A = \underbrace{\begin{bmatrix} 1 & \log(r_0) \\ 1 & \log(r_1) \\ \vdots & \vdots \\ 1 & \log(r_n) \end{bmatrix}}_B \times \underbrace{\begin{bmatrix} \log(\alpha(\vec{x})) \\ h(\vec{x}) \end{bmatrix}}_Y \quad (4.19)$$

Equation (4.17) can then be solved using the Least-square approach:

$$Y = (B^T B)^{-1} B^T A \quad (4.20)$$

with $Y(2) = h(\vec{x})$. This approach, however, doesn't hold good for small images and is a special case only for large images [202]. This method for small images yields a coarse approximation of the exponents.

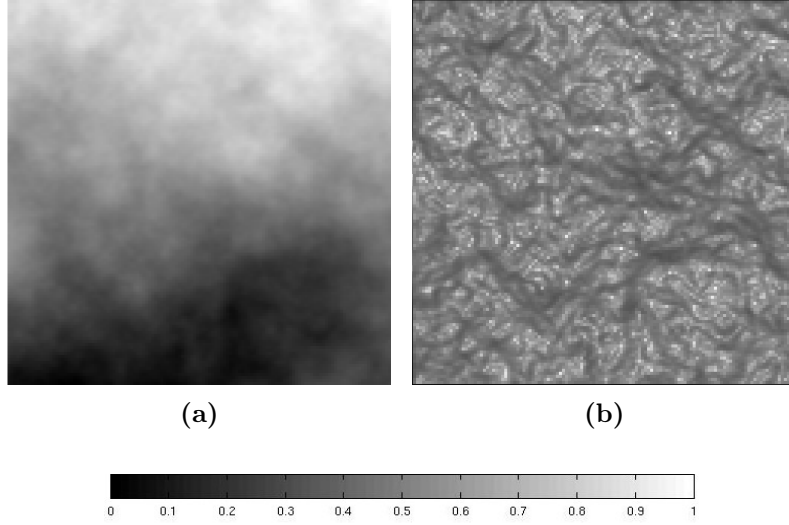


Figure 4.3: (a) Image of a simulated optical phase perturbed by atmospheric turbulence. The image corresponds to a 128×128 pixels sub-image extracted from an original 256×256 pixels image to avoid the pupil boundary. (b) Image of the singularity exponents computed on the phase data using β -Lorentzian wavelet.

4.3.2 Singularity analysis via wavelet projection

The standard technique used to overcome the problem in the log-log technique involves the use of wavelet projections as singularity analyzers. The wavelet theory is a valuable tool in analysing the multiscale properties of a signal. The choice of wavelet plays an important role in the determination of $h(\vec{x})$, and it has been seen [201] that the wavelets β -Lorentzian and Gaussian prove to be a good choice:

$$\beta - \text{Lorentzian} : \psi(\vec{x}) = \psi^\beta(\vec{x}) = \frac{1}{(1 + |\vec{x}|^2)^\beta} \quad (4.21)$$

$$\text{Gaussian} : \psi(\vec{x}) = e^{-\frac{|\vec{x}|^2}{2}} \quad (4.22)$$

It should be noted here that both types of wavelet are isotropic, i.e., they do not privilege any particular direction [203]. The wavelet projection of the

measure μ at scale r and point \vec{x} is then defined as:

$$\mathcal{T}_\psi\mu(\vec{x}, r) = \int \|\nabla I\|(\vec{y}) \frac{1}{r^d} \psi\left(\frac{\vec{x} - \vec{y}}{r}\right) d\vec{y} \quad (4.23)$$

where d is the dimension of the signal domain. Equation (4.16) can then be re-written as:

$$\mathcal{T}_\psi\mu(\vec{x}, r) = \alpha_\psi(\vec{x}) r^{h(\vec{x})} + o(r^{h(\vec{x})}) \quad (4.24)$$

and $h(\vec{x})$ is obtained by a linear regression of $\log(\mathcal{T}_\psi\mu(\vec{x}, r))$ vs. $\log(r)$ as:

$$h(\vec{x}) = \lim_{r \rightarrow 0} \frac{\log(\mathcal{T}_\psi\mu(\vec{x}, r)/\alpha_\psi(\vec{x}))}{\log(r)} \quad (4.25)$$

where $\alpha_\psi(\vec{x})$ is a constant depending on the choice of the wavelet and is independent of the scale r . The singularity exponents of an optical phase computed via wavelet projection is shown in Fig 4.3.

§ 4.4 CONCLUSION

In this chapter, we have introduced the concept of multifractal systems and the Microcanonical Multiscale Formalism, which tries to explore the multiscale behaviour of complex systems and its underlying dynamics related to the cascading behaviour in real-world signals [147, 64]. We have shown the existence of multiscale features, in a perturbed optical phase signal, through the multifractal analysis of its singularity spectrum. In the next chapter, we will justify the use of singularity exponents as the right candidate for describing the multiscale behaviour of turbulent signals, like the optical phase, and in the process on natural images as well. We will show that the critical exponents (the singularity exponents as we name them) $h(\vec{x})$ give access to a notion of transition in the case of turbulent data, in a way that generalizes *edge detection* by classical operators in the case of non-turbulent data. Edges convey the multiscale information of a signal, and we show that edges detected by MMF are not only consistent along the scales of a signal, but are also ideal candidates for reconstructing the signal.

- CHAPTER 5 -

CRITICAL EXPONENTS AND INFERENCE ACROSS THE SCALES

Transmission of information across the scales of a complex signal has some interesting potential, notably in the derivation of sub-pixel information, cross-scale inference and data fusion. It follows the structure of complex signals themselves, when they are considered as acquisitions of complex systems. In this section, we contemplate the problem of cross-scale information inference through the determination of appropriate multiscale decomposition. We demonstrate that microcanonical formulations, for understanding and evaluating the mechanisms that govern the evolution of dynamical systems, lead to accurate inference schemes across the scales in complex signals. Consequently, we study the notion of optimal wavelet [152, 200, 45] for inferring information across the scales. Such a wavelet is capable of extracting the essential multiscale features of a signal, thereby allowing information extraction across scales with minimal error. For the case of wavefront phase reconstruction in AO, a multiresolution analysis associated to an optimal wavelet (related to the turbulent phase signal) would therefore allow a near lossless extraction of details in the intermediate scales. Knowledge of the details with high precision, would then allow us in reconstructing high-resolution gradients from its low-resolution version, and subsequently the phase using any surface reconstruction algorithm. However, the accurate determination of an optimal wavelet for real data is still a challenge, and the attempts made so

far (we give an example of computing it on synthetic data in section 5.1.2) produce only approximative versions of it, thereby limiting the probability of maximum inference across scales. This leads us to define an alternative approach by which maximum cross-scale information inference is possible.

As discussed in the previous chapter, the singularity exponents carry the most relevant multiscale features of a signal. They give access to a notion of transition in the case of turbulent data, in a way that generalizes edge detection by classical operators in the case of non-turbulent data. Edges convey the multiscale information of a signal, and it is seen that edges obtained through singularity analysis are not only consistent along the scales of a signal, but are also ideal candidates for reconstructing the signal (from information contained in the edges [201, 125]). One possible way of an optimal inference across the scales can therefore be achieved by a multiresolution analysis on the signal of the singularity exponents. In order to justify this approach we first validate, through experimental analysis, the potential of the singularity exponents in encoding the most relevant multiscale features of a signal. We do this in two steps:

- We first prove that singularity exponents provide a notion of edge, well-adapted to the case of turbulent signals and coherent across the scales of the signal (see section 5.2).
- We then show that, compared to edges detected by classical edge detectors, better reconstruction of the signal is achieved from the edges obtained through singularity analysis (see section 5.3).

The choice of a mother wavelet for multiresolution analysis on the signal of singularity exponents also has some consequences on the optimality of cross-scale inference and quality of reconstruction. In section 5.1.3, we investigate the possibility of finding a “good” wavelet for the case of the turbulent phase data.

The chapter is organized as follows: In section 5.1, we introduce the concept of optimal wavelets in realizing the optimal information inference procedure from a given turbulent signal, we talk about appropriate functionals to realize such processes, where in section 5.1.1, we introduce the concept

of multiresolution analysis to perform the inference operation. We then introduce the concept of edge detection using singularity exponents in section 5.2, where edge consistency across the scales is addressed in section 5.2.2. Reconstructing a signal from its edge representation is discussed in section 5.3 with results of the reconstruction in section 5.3.5. Finally, we conclude in section 5.4.

§ 5.1 OPTIMAL INFERENCE ACROSS SCALES : REALIZING THE MICROCANONICAL CASCADE

As discussed in the previous chapter, in MMF, a commonly used function Γ_r for equation (4.7) is obtained through a measure μ defined by the norm of the signal's gradient in the following way:

$$\Gamma_r(\vec{x}) = \mu(B_r(\vec{x})) = \int_{B_r(\vec{x})} \|\nabla s\|(\vec{y}) d\vec{y} \quad (5.1)$$

where $B_r(\vec{x})$ is a ball of radius r centered at pixel location \vec{x} . We recall the Kolmogorov theory on energy cascades (see section 4.2, chapter 4), where two functionals Γ_r and Γ_L , representing the same operation at scales r and L respectively, $0 < r < L$, are related by an energy transfer parameter $\eta_{r/L}$ and can be written as:

$$\Gamma_r s \doteq \eta_{r/L} \Gamma_L s \quad (5.2)$$

The above equation, however, relate only the laws of the distribution and would not imply any corresponding relation pointwise i.e. $\Gamma_r s(\vec{x}) \neq \eta_{r/L} \Gamma_L s(\vec{x})$. However, one can formally define the variables of equation (5.2) as [217]:

$$\theta_{r/L}(\vec{x}) = \frac{\Gamma_r(\vec{x})}{\Gamma_L(\vec{x})} \quad (5.3)$$

But in general, the variables $\theta_{r/L}(\vec{x})$ defined by the above equation are such that there is no independence between $\theta_{r/L}(\vec{x})$ and $\Gamma_L(\vec{x})$. The random variables $\Gamma_r(\vec{x})$ carry the multiscale properties of the signal, but it is impossible to retrieve the cascading properties pointwise (called the microcanonical cascade) from its definition.

To tackle this problem, we make use of multiresolution analysis associated to wavelet transform. We say that for a given wavelet Ψ , and the original signal s , there is a multiscale operator which will be able to extract the information pointwise from the cascading properties of the signal. This multiscale operator can be defined as:

$$\Gamma_{\Psi}\mu(\vec{x}, r) = \int \|\nabla s\|(\vec{y})\Psi\left(\frac{\vec{x} - \vec{y}}{r}\right)d\vec{y} \quad (5.4)$$

Exactly like in equation (5.3), we can now define a random process $\zeta_{r/L}(\vec{x})$ as:

$$\Gamma_{\Psi}\mu(\vec{x}, r) = \zeta_{r/L}(\vec{x})\Gamma_{\Psi}\mu(\vec{x}, L) \quad (5.5)$$

Now, we can talk about a wavelet Ψ which, if determined, will make $\zeta_{r/L}(\vec{x})$ independent of $\Gamma_{\Psi}\mu(\vec{x}, L)$. Such a wavelet is called an *optimal wavelet*: it has the potential of unlocking the signal's microcanonical cascading properties through simple wavelet multiresolution analysis. We can thus define optimality of a wavelet as the degree of independence of $\zeta_{r/L}(\vec{x})$ vs $\Gamma_{\Psi}\mu(\vec{x}, L)$.

Before getting into the details of an optimal wavelet analysis, it is important to realize the microcanonical cascade process of a turbulent signal. We achieve this realization with the help of multiresolution analysis and wavelet transform, which is discussed in the subsequent section.

5.1.1 Multiresolution Analysis & wavelet transform

In this section, we recall the notion of multiresolution analysis and its practical implementation with digital filters [128]. Multiresolution analysis is mathematically formulated by the L^2 sub-space decomposition associated to wavelet projection. In order to realize the different sub-spaces, the wavelet theory suggests the use of certain functions Φ and Ψ , also known as the *scaling function* and the *wavelet function* respectively. Φ and Ψ forms the basis for multiscale functions in multiresolution analysis. In order to minimize data redundancy, so that the different sub-spaces convey new information of the object, we make use of dyadic wavelet sequences [128] which are geometric sequences of factor 2.

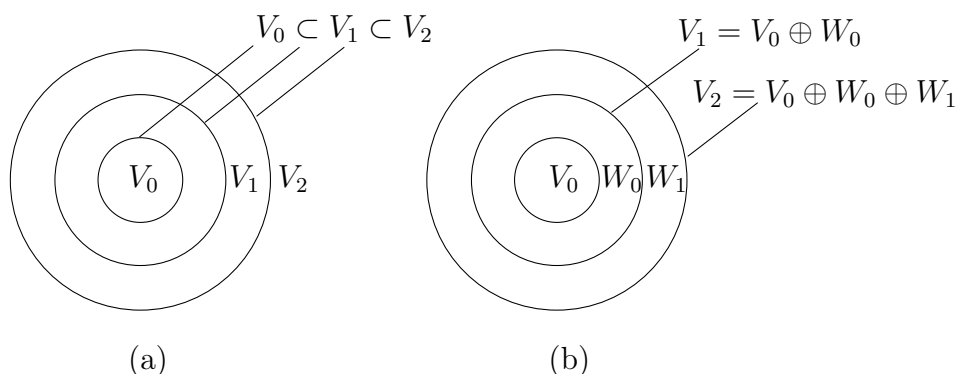


Figure 5.1: Realization of sub-space by scaling and wavelet functions: (a) Sub-space relationship of scaling functions. (b) Sub-space relationship of scaling and wavelet functions.

5.1.1.1 Realizing the scaling function

The scaling function Φ can be realized as the *scaled* and *shifted* version of some basis function. Φ is then defined in terms of two parameters: p which is the scale parameter and q the shift parameter, where $p, q \in \mathbb{Z}$ and $\Phi(\vec{x}) \in L^2(\mathbb{R})$, as:

$$\Phi_{p,q}(\vec{x}) = 2^{p/2} \Phi(2^p \vec{x} - q) \quad (5.6)$$

Let us take an example, where we define $\Phi(\vec{x})$ as:

$$\Phi(\vec{x}) = \begin{cases} 0 & \text{if } x \in [0, 1] \\ 1 & \text{otherwise} \end{cases}$$

This function is also known as the Haar function. When $p = 0, q = 0$, $\Phi_{0,0}(\vec{x}) = \Phi(\vec{x})$, when $p = 1, q = 0$, $\Phi_{1,0}(\vec{x}) = \sqrt{2} \Phi(2\vec{x})$ i.e. the width of $\Phi_{1,0}(\vec{x})$ is half of that of $\Phi_{0,0}(\vec{x})$. As a result $\Phi_{0,0}(\vec{x})$ cannot be used to approximate $\Phi_{1,0}(\vec{x})$. But, by scaling and shifting $\Phi_{1,0}(\vec{x})$ one can approximate $\Phi_{0,0}(\vec{x})$ as:

$$\Phi_{0,0}(\vec{x}) = \frac{1}{\sqrt{2}} \Phi_{1,0}(\vec{x}) + \frac{1}{\sqrt{2}} \Phi_{1,1}(\vec{x}) \quad (5.7)$$

Let us now define a sub-space V_0 corresponding to $p = 0$ and covering the width of $\Phi_{0,0}(\vec{x})$. Now, we increase the scale p by unity. The next sub-space V_1 is then realized by $\Phi_{1,q}(\vec{x})$. So, V_1 forms a super-set of V_0 , since whatever

can be measured by $\Phi_{0,0}(\vec{x})$, can also be measured by $\Phi_{1,0}(\vec{x})$. Similarly V_2 is realized by $\Phi_{2,q}(\vec{x})$. We can say that the sub-space covered by the scaling functions at lower scales is contained within the sub-space covered by those at higher scales and is given by the relationship (see Fig 5.1(a)):

$$V_{-\infty} \subset \cdots \subset V_{-1} \subset V_0 \subset V_1 \subset V_2 \subset \cdots \subset V_{\infty} \quad (5.8)$$

The scaling functions of sub-space V_0 can therefore be expressed as a weighted summation of scaling functions of higher-order sub-spaces as:

$$\Phi(\vec{x}) = \sum_n h_{\Phi}(n) \sqrt{2} \Phi(2\vec{x} - n) \quad (5.9)$$

where $h_{\Phi}(n)$ are the scaling function coefficients.

5.1.1.2 Realizing the wavelet function

Let us now consider the difference in sub-spaces (we will call them as detail sub-spaces from here on) i.e. $V_1 - V_0 = W_0$ which is also a sub-space. From Fig 5.1(b), we can write:

$$V_2 = V_1 \oplus W_1 = V_0 \oplus W_0 \oplus W_1 \quad (5.10)$$

So, we must develop functions that can cover the detail sub-space. Considering the Haar example of $\Phi(\vec{x})$, if this function is applied over a signal, a kind of averaging, i.e. low-pass filtering is done. For defining a function that should cover the detail sub-space, we are essentially trying to cover the difference in the spaces covered by two low-pass filters i.e. a high pass filtering operation. So the class of filters that can cover the detail sub-space has to be a high-pass filter and the class of functions that are used to cover the detail sub-space are given by:

$$\Psi_{p,q}(\vec{x}) = 2^{p/2} \Psi(2^p \vec{x} - q) \quad (5.11)$$

$\Psi_{p,q}(\vec{x}) \in L^2(\mathbb{R})$ is known as the *wavelet function* or just the *wavelet*. Although the functional forms of Φ and Ψ are the same, the scaling functions and the wavelet functions differ by their spanning sub-spaces. Also, the wavelet Ψ has the following properties [128]:

- The shifted version of $\Psi_{p,q}(\vec{x})$ has to be orthogonal with each other.
- $\Psi_{p,q}(\vec{x})$ must be functions which should be oscillatory in nature i.e. it should go to the positive as well as the negative.
- The area under these functions should be zero i.e. the area covered by the positive part is nullified by the area covered by the negative part.

The relation between the scaling functions and the wavelets can be summarized accordingly: let $s(\vec{x})$ be a function belonging to the V_1 sub-space, and not V_0 . A crude approximation of $s(\vec{x})$ is then provided by the scaling functions of V_0 and the wavelet functions of W_0 provide the details. We can, therefore, say that the scaling functions and the wavelet functions help to analyze, respectively, a low-pass and a high-pass filtered version of $s(\vec{x})$. The wavelet function can be expressed in terms of the scaling function as:

$$\Psi(\vec{x}) = \sum_n h_\Psi(n) \sqrt{2} \Phi(2\vec{x} - n) \quad (5.12)$$

where $h_\Psi(n)$ are the wavelet function coefficients.

5.1.1.3 Multiscale representation of a signal using wavelet transform

Any signal $s(\vec{x})$ can be represented in a dyadic wavelet basis of mother wavelet Ψ [128] as:

$$s(\vec{x}) = \sum_q \beta_{p_0,q} \Phi_{p_0,q}(\vec{x}) + \sum_{p=p_0}^{\infty} \sum_q \alpha_{p,q} \Psi_{p,q}(\vec{x}) \quad (5.13)$$

where $\beta_{p_0,q}$ and $\alpha_{p,q}$ are the corresponding expansion coefficients. The first term of the above equation, involving the scaling functions, provide approximations of $s(\vec{x})$ at scale p_0 , while the second term having the wavelet functions provide details of the approximation at scale p_0 and higher. $\alpha_{p,q}$ are also known as the *wavelet coefficients*. The coefficients of equation (5.13) can be obtained from the following equations:

$$\beta_{p_0,q} = \int \Phi_{p_0,q}(\vec{x}) s(\vec{x}) d\vec{x} \quad (5.14)$$

$$\alpha_{p,q} = \int \Psi_{p,q}(\vec{x}) s(\vec{x}) d\vec{x} \quad (5.15)$$

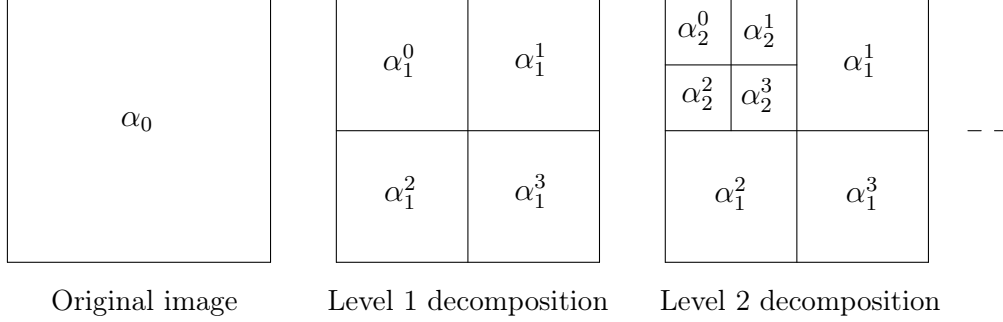

Original image
Level 1 decomposition
Level 2 decomposition

Figure 5.2: Representation of the decomposition in multiresolution analysis. « α_j » is the approximation of the initial image « α_0 » at the resolution j . « α_j^1 », « α_j^2 » and « α_j^3 » are the horizontal, vertical and diagonal details respectively at the resolution j .

This process of decomposing (or analyzing) the signal into approximation and detail coefficients is known as the *forward wavelet transform*. The process of decomposition can be repeated over different scales p to realize the different sub-spaces necessary.

In the case of 2D signals, we have to apply the wavelet transform in two directions: rows(n_1) and columns(n_2). Since, we are discretizing the signal by the use of dyadic wavelets, we will express $s(\vec{x})$ as $s(n_1, n_2)$ from now on. The notations for the scale parameter and shift parameter are changed to j and k_1, k_2 respectively. The decomposition process in images therefore realizes the necessity of four filters that can be recursively applied along the rows and columns to produce four coefficients (one approximation and three details: horizontal, vertical and diagonal). The four filters can be defined as:

$$\begin{aligned}
 \Phi(n_1, n_2) &= \Phi(n_1)\Phi(n_2) \\
 \Psi^H(n_1, n_2) &= \Phi(n_1)\Psi(n_2) \\
 \Psi^V(n_1, n_2) &= \Psi(n_1)\Phi(n_2) \\
 \Psi^D(n_1, n_2) &= \Psi(n_1)\Psi(n_2)
 \end{aligned} \tag{5.16}$$

Therefore, in a first level decomposition (scale $j = 1$), a low-pass filtering along the rows and columns gives rise to the approximation coefficient α_1^0 (we write α_1^0 instead of β_0 for simplicity), a low-pass filtering along the rows and

then a high-pass filtering along the columns gives rise to the horizontal detail α_1^1 , a high-pass filtering along the rows followed by a low-pass filtering along the columns results in the vertical detail α_1^2 and finally high-pass filtering in both the rows and columns of the image results in the diagonal details α_1^3 . And in all cases, we have to do a decimation by a factor of 2 i.e. an overall decimation by a factor of 4. Hence, the decomposition process using multiresolution analysis gives rise to an approximation image fourth smaller than the previous one. Since, images are generally rich in low-frequency components, the decomposition process is repeated over the approximation coefficient for further levels. The process can be viewed in Fig 5.2.

Reconstruction from the expansion coefficients finds each α_j from α_{j+1}^i , where i represents the orientation ($i = 0$ represents the approximation of the image α_j^0 at the resolution j , $i = 1$ represents the horizontal details α_j^1 , $i = 2$ the vertical details α_j^2 , and $r = 3$ the diagonal details α_j^3 at the dyadic scale 2^j and at position $2^j k_1, 2^j k_2$). This process of reconstructing (or synthesis) the signal from its coefficients is known as the *inverse wavelet transform*. Generalizing α_j^0 as the approximation coefficient, equation (5.13) can be simplified, in the discrete sense, as:

$$s(n_1, n_2) = \sum_{i=0,1,2,3} \sum_j \sum_{k_1, k_2} \alpha_{j, k_1, k_2}^i \Psi_{j, k_1, k_2}^i(n_1, n_2) \quad (5.17)$$

where $\Psi_{j, k_1, k_2}^0(n_1, n_2)$ represents the scaling function $\Phi_{j_0, k_1, k_2}(n_1, n_2)$.

The 2D scaling and wavelet functions (generalized as $\Psi_{j, k_1, k_2}^i(n_1, n_2)$ in equation (5.17)), used in the multiresolution decomposition and reconstruction of a signal, can be realized through separable, one-dimensional FIR digital filters of impulse responses $h_\Phi(-n)$ and $h_\Psi(-n)$. The choice of the filters depends on the choice of the scaling function and the wavelet. The relation between h_Φ and h_Ψ is given by:

$$h_\Psi(n) = (-1)^n h_\Phi(1 - n) \quad (5.18)$$

These filters, which act as the high-pass and low-pass filters, are applied along the rows and columns of an image to obtain the desired coefficients α_{j, k_1, k_2}^i . The process is more elegantly expressed by Fig 6.2 and Fig 6.3, in chapter 6.

Notice that when obtaining the multiresolution decomposition of an image the details at each resolution level refer to the same physical positions, but after each iteration they are defined at a coarser scale [217, 157]. Therefore, each *parent coefficient* $\alpha_p = \alpha_{j+1, k_1/2, k_2/2}^i$, at the coarser scale, covers the same spatial extent of four *children coefficients* $\alpha_c = \alpha_{j, k_1, k_2}^i$ at the finer scale.

5.1.2 Approximating the microcanonical cascade

The effective determination of an optimal wavelet for a given turbulent acquisition is a very complicated and unsolved problem. The child-parent dependancy valid for most wavelets, which are not too far from the optimal case, can be described in terms of a particular model (see equation (5.5) for explanation):

$$\alpha_c = \eta_1 \alpha_p + \eta_2 \quad (5.19)$$

with α_c : ‘child’ wavelet coefficient, α_p : ‘parent’ wavelet coefficient, η_1, η_2 : random variables independant of α_c and α_p and also independant of each other. For an optimal wavelet the above equation takes the form $\alpha_c = \eta_1 \alpha_p$ with η_1 independent of α_p . We can therefore write for all scales j and position k , the wavelet coefficients $\alpha_{j,k}$ as:

$$\begin{aligned} \alpha_{j,k} &= \eta_{j,k} \alpha_{j-1, [k/2]} \\ &= \eta_{j,k} \eta_{j-1, [k/2]} \alpha_{j-2, [k/4]} \\ &= \eta_{j,k} \eta_{j-1, [k/2]} \eta_{j-2, [k/4]} \dots \alpha_{0,0} \\ &= \prod_{j',k} \eta_{j', [k/2^{j-j'}]} \alpha_{0,0} \end{aligned} \quad (5.20)$$

for all orientation i .

The first ideas of finding an optimal wavelet for natural images were explored in [199, 198]. Generalizing equation (5.17), a given signal $s(\vec{x})$ can be expressed in the form of a wavelet series (set of signals) with the help of its wavelet coefficients as:

$$s(\vec{x}) = \sum_{j,k} \alpha_{j,k} \psi_{j,k}(\vec{x}) \quad (5.21)$$

Comparing with equation (5.20), this gives us:

$$\begin{aligned}
 s(\vec{x}) &= \sum_{j,k} \prod_{j',k} \eta_{j',[k/2^j-j']} \alpha_{0,0} \psi_{j,k}(\vec{x}) \\
 &= \sum_{j \neq 0,k} \prod_{j',k} \eta_{j',[k/2^j-j']} \alpha_{0,0} \psi_{j,k}(\vec{x}) + \alpha_{0,0} \psi_{0,0}(\vec{x}) \\
 &= \sum_{j \neq 0,k} \alpha_{j,k} \psi_{j,k}(\vec{x}) + \alpha_{0,0} \psi_{0,0}(\vec{x}) \tag{5.22}
 \end{aligned}$$

where $\psi_{j,k}$ now forms the wavelet basis for the optimal wavelet. Now, the expectation of the signal $\langle s(\vec{x}) \rangle = 0$ as $\langle \alpha_{0,0} \rangle = 0$ and $\langle \alpha_{j,k} \rangle = 0$ due to symmetry. However, if we consider $\sigma_{0,0}$ to be the sign of $\alpha_{0,0}$, we can write $\alpha_{0,0} = \text{sign}(\alpha_{0,0}) \text{abs}(\alpha_{0,0}) = \sigma_{0,0} |\alpha_{0,0}|$. We can then consider an ensemble average of dynamically equivalent signals, say $\langle s^p(\vec{x}) \rangle$ to get the expected value for all these signals (p is the index of an ordering of the signals). Equation (5.22) can then be generalized to:

$$\begin{aligned}
 \langle \sigma_{0,0}^p | s^p(\vec{x}) \rangle &= \sum_{j \neq 0,k} \langle \sigma_{0,0} \rangle \langle \alpha_{j,k} \rangle \psi_{j,k}(\vec{x}) + \langle \sigma_{0,0} \alpha_{0,0} \rangle \psi_{0,0}(\vec{x}) \\
 &= \sum_{j \neq 0,k} \langle \sigma_{0,0} \rangle \langle \alpha_{j,k} \rangle \psi_{j,k}(\vec{x}) + \langle \sigma_{0,0} \sigma_{0,0} |\alpha_{0,0}| \rangle \psi_{0,0}(\vec{x}) \\
 &= \sum_{j \neq 0,k} \langle \sigma_{0,0} \rangle \langle \alpha_{j,k} \rangle \psi_{j,k}(\vec{x}) + \langle |\alpha_{0,0}| \rangle \psi_{0,0}(\vec{x}) \tag{5.23}
 \end{aligned}$$

where $\langle \cdot | \cdot \rangle$ denotes the standard Hermitian product on \mathbb{C}^2 . $\sigma_{0,0}$ is independent of all the terms except $\alpha_{0,0}$. So the term $\langle \sigma_{0,0} \rangle \langle \alpha_{j,k} \rangle \psi_{j,k}(\vec{x})$ is zero due to $\langle \alpha_{j,k} \rangle = 0$. Hence equation (5.23) reduces to:

$$\langle \sigma_{0,0}^p | s^p(\vec{x}) \rangle = \langle |\alpha_{0,0}| \rangle \psi_{0,0}(\vec{x}) \tag{5.24}$$

We don't know the sign, so we try to estimate the sign of $\alpha_{0,0}$. Let $\epsilon_{0,0}$ be the estimation, we then have:

$$\langle \epsilon_{0,0}^p | s^p(\vec{x}) \rangle = \langle \epsilon_{0,0} \sigma_{0,0} |\alpha_{0,0}| \rangle \psi_{0,0}(\vec{x}) \propto \psi_{0,0}(\vec{x}) \tag{5.25}$$

So, a correct estimate of $\langle \epsilon_{0,0}^p | s^p(\vec{x}) \rangle$ will lead us to the optimal wavelet. The product $\epsilon_{0,0} \sigma_{0,0}$ in the above equation, can either be positive or negative. If we have correct estimate of the sign, the product will be positive.

Now, $\sigma_{0,0}$ is the sign of $\alpha_{0,0} = \text{sign}$ of the projection of the signal $s(\vec{x})$ on the wavelet $\psi_{0,0}(\vec{x}) = \text{sign}\langle s(\vec{x})|\psi_{0,0}(\vec{x})\rangle$. Since we don't know $\psi_{0,0}$, we try to make the projection of the signal on the element which has the most dependency with all the other elements (i.e. dominant presence of the term $\langle |\alpha_{0,0}| \rangle \psi_{0,0}(\vec{x})$). We will call this element as the most central element or MCE. The principle of finding the MCE on a given realization of signals is explained in algorithm 1.

Algorithm 1 Finding the MCE

Step 1: Subdivide a given image $s^p(\vec{x})$ over small areas of equal sizes and normalize individually every sub-image. Do this for all the realizations of p .

Step 2: We denote every sub-image as $s_{u,v}^p(\vec{x})$, where u, v gives the sub-image position in p . Let N be the total number of sub-images.

Step 3: For every sub-image, find its correlation with all the other sub-images (for all p) i.e., $C_{p,p'} = \langle s_{u,v}^p(\vec{x})|s_{u',v'}^{p'}(\vec{x})\rangle$.

Step 4: Find the average of the correlation for every sub-image i.e., $\frac{1}{N} \sum_N |C_{p,p'}|$.

Step 5: Find for which $s_{u,v}^p(\vec{x})$, the average correlation is maximum. Let it be $s_{u^*,v^*}^{p^*}(\vec{x})$.

Step 6: We call $s_{u^*,v^*}^{p^*}(\vec{x})$ as the MCE.

Step 7: Repeat and check for different sizes of $s_{u,v}^p(\vec{x})$, to get the best result.

After determining the MCE, we estimate the sign of every $s_{u,v}^p(\vec{x})$, by orienting it with the sign of the MCE. For ease of understanding, we fix the sub-image size as the image size i.e. $s_{u,v}^p(\vec{x}) = s^p(\vec{x})$ which is the same as repeating Algorithm 1, not with sub-images but with the image itself. In this case, we assume that the MCE is a signal within the realization p , denoted by $s^{p^*}(\vec{x})$, and we estimate the sign as:

$$\begin{aligned}
 \epsilon_{0,0}^p &= \sigma(C_{p,p^*}) = \sigma(\langle s^p(\vec{x})|s^{p^*}(\vec{x})\rangle) \\
 &= \langle \sigma_{0,0}s(\vec{x})|\sigma_{0,0}^*|\alpha_{0,0}^*|\psi_{0,0}(\vec{x})\rangle \\
 &= |\alpha_{0,0}^*|\sigma_{0,0}\sigma_{0,0}^*\langle s(\vec{x})|\psi_{0,0}(\vec{x})\rangle
 \end{aligned} \tag{5.26}$$

$|\alpha_{0,0}^*|$ being a constant, we are left with the projection of the signal on the wavelet and its sign $\sigma_{0,0}\sigma_{0,0}^*$. If we have a correct estimate of the sign, we

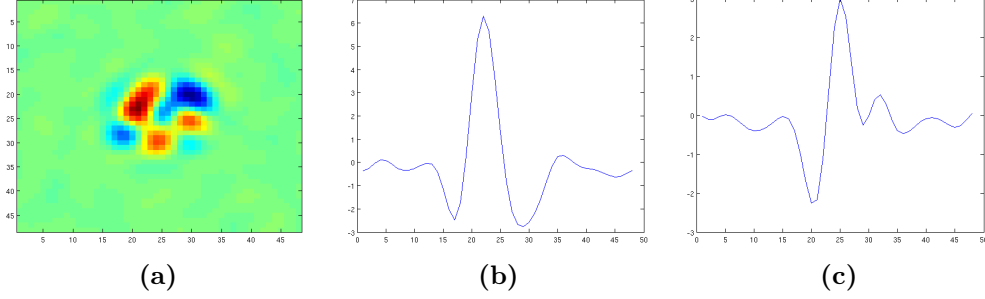


Figure 5.3: (a) Realization of $\langle \epsilon_{0,0} | s(\vec{x}) \rangle$, from equation (5.27), for the Benzi model [24], at 48×48 pixels resolution. (b) X-cut of (a). (c) Y-cut of (a).

can say $\langle \epsilon_{0,0}^p | s^p(\vec{x}) \rangle \propto \langle \sigma_{0,0}^p | s^p(\vec{x}) \rangle$ i.e., we can have a field, for a particular realization p , whose distribution will be close to the optimal wavelet (see equation (5.25)). Considering this process repeated over all the realizations and then summed, should magnify the presence of the wavelet in the resultant image. The resultant image is therefore obtained accordingly:

$$\langle \epsilon_{0,0} | s(\vec{x}) \rangle = \sum_p \langle \sigma(C_{p,p^*}) | s^p(\vec{x}) \rangle = \sum_p \langle \sigma(\langle s^p(\vec{x}) | s^{p^*}(\vec{x}) \rangle) | s^p(\vec{x}) \rangle \quad (5.27)$$

We have tested this algorithm on Benzi model [24]. We recall the computation of multiaffine functions in Benzi model. A random field $R(\vec{x})$ is generated by wavelet decomposition such that:

$$R(\vec{x}) = \sum_{j=-\infty}^{+\infty} \sum_{k=-\infty}^{+\infty} \alpha_{j,k} \psi_{j,k}(\vec{x}) \quad (5.28)$$

with the wavelet family $\psi_{j,k}(\vec{x}) = 2^{j/2} \psi(2^j \vec{x} - k)$. The coefficients $\alpha_{j,k}$ are generated such that:

$$\begin{aligned} \alpha_{1,0} &= \epsilon_{1,0} \eta_{1,0} \alpha_{0,0}, & \alpha_{1,1} &= \epsilon_{1,1} \eta_{1,1} \alpha_{0,0}, \\ \alpha_{2,0} &= \epsilon_{2,0} \eta_{2,0} \alpha_{1,0}, & \alpha_{2,1} &= \epsilon_{2,1} \eta_{2,1} \alpha_{1,0}, \\ \alpha_{2,2} &= \epsilon_{2,2} \eta_{2,2} \alpha_{1,1}, & \alpha_{2,3} &= \epsilon_{2,3} \eta_{2,3} \alpha_{1,1}, \end{aligned} \quad (5.29)$$

and so on with $\epsilon_{j,k} = \pm 1$ with equal probability; $\eta_{j,k}$ are independent random

variables having the same distribution $\mathcal{P}(\eta)$ given by:

$$\mathcal{P}(\eta) = y\delta(\eta - \eta_0) + (1 - y)\delta(\eta - \eta_1) \quad (5.30)$$

where a typical realization of $R(\vec{x})$ in [24] is obtained for $y = 0.125$, $\eta_0 = 2^{-1/2}$ and $\eta_1 = 2^{-5/6}$. The wavelet $\psi(\vec{x})$ considered for the Benzi model is a mexican-hat function obtained from differentiation of a Gaussian:

$$\psi(\vec{x}) = \frac{d^2}{dr^2} \exp\left(-\frac{r^2}{2\sigma^2}\right) \quad \text{with } r^2 = \|\vec{x}\|^2 \quad (5.31)$$

For this particular model the optimal wavelet should correspond to ψ , which is a mexican-hat function.

We compute over $p = 1000$ realizations of the Benzi data. The preliminary results are shown in Fig 5.3. It is clear from the results, that although the essence of a mexican-hat function can be realized from the data (the X-cut), it is still not close to the ground truth (the Y-cut does not correspond to a mexican-hat function). The process is also computationally highly demanding. The failure of the approach, even for the case of synthetic data, makes it obviously more challenging for the case of real world signals. This leads us to define an alternative approach for optimal inference across the scales of a signal. Nevertheless, a close approximation of an optimal wavelet for a given turbulent signal will play a crucial role in the multiresolution analysis process. In the next section, we concentrate on finding such an approximative wavelet for turbulent phase signals.

5.1.3 Choice of wavelet

As discussed in section 5.1.2, the child-parent dependancy, for an optimal wavelet, takes the form $\alpha_c = \eta_1 \alpha_p$. A log domain representation of it implies:

$$\ln |\alpha_c| = \ln |\eta_1| + \ln |\alpha_p| \quad (5.32)$$

Therefore, the local probability maxima in the conditional histogram of $\ln |\alpha_c|$ in terms of $\ln |\alpha_p|$, for an optimal wavelet, must be a straight line of slope 1 [157]. However, for a sub-optimal wavelet we will observe a deviation in the linearity, a horizontal bend is observed on the left. This is obvious as per equation (5.19), where the term η_2 becomes dominant when the value of

5.1. Optimal Inference across scales : Realizing the microcanonical cascade

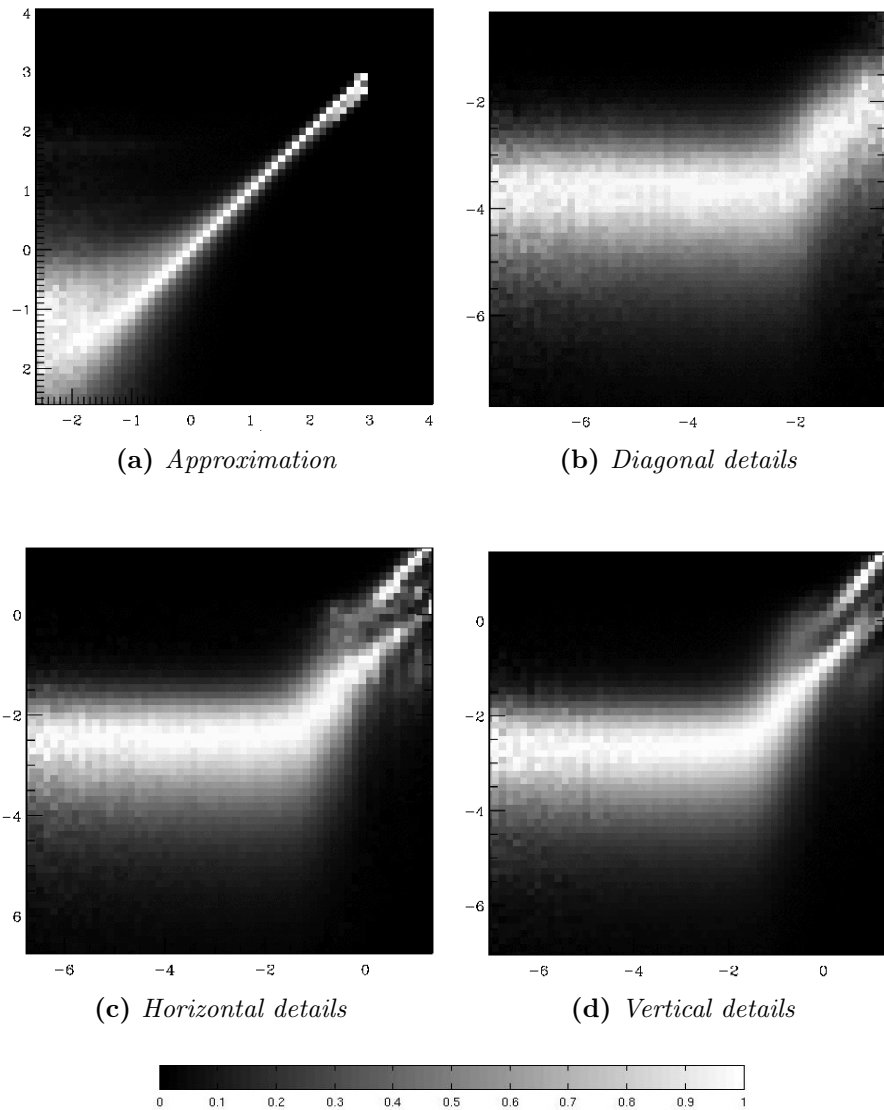


Figure 5.4: *Conditional histograms of the experimental phase data. The wavelet used for this experiment is the order 3 Battle-Lemarié wavelet with 41 central coefficients. The horizontal axis corresponds to $\ln|\alpha_p|$ and the vertical to $\ln|\alpha_c|$. **Top:** Approximation coefficients are shown in the left image, diagonal details (orthogonal complements) are shown in the right image. **Bottom:** Horizontal details are shown in the left image, vertical details on the right image (both correspond to the orthogonal complements in multiresolution analysis).*

α_p becomes smaller. We will therefore be interested in observing a linearity in the conditional histograms (for different wavelet coefficients) for higher values of α_p . So, to test the optimality of a wavelet, we examine the conditional expectation value $E(\ln |\alpha_c| | \ln |\alpha_p|)$ for the different types of wavelet coefficients. We have used 37 standard wavelets belonging to different families. They are: Haar, Daubechies (orders 2 to 20), Coiflet (orders 1 to 5), Symlet (orders 4 to 10) and Battle-Lemarié (orders 1, 3, 5, 7 and 9). The conditional histograms are plotted over a set of 1000 sub-images extracted from the dataset of 1000 turbulent phase screens (data described in section 6.1) provided by ONERA. Fig. 5.4 shows the linear/affine character for the Battle-Lemarié wavelet of order 3; the functional dependancies for the approximation as well as the orthogonal (horizontal, vertical and diagonal) complements provide a qualitative estimation of the optimality of a wavelet decomposition. The two parallel lines, seen for the higher values of α_p in the horizontal and vertical details, show some tendencies in the data revealing a deviation from optimality.

Following the program announced previously in this thesis, we are now in place for devising an alternative optimal multiresolution analysis since, as we have seen, the computation of a high precision optimal wavelet from long exposure turbulent phase data is not possible at this moment. We turn towards one of the main results obtained in this thesis which shows that a very good approximation of an optimal multiresolution analysis can be obtained by considering a classical multiresolution analysis on the signal of singularity exponents (computed on the phase data), instead of the phase itself. The profound reason behind this idea lies in the ability of the singularity exponents to encode efficiently the transitions in a turbulent signal. We will indeed see that, in the case of turbulent data, classical edge detection algorithms fail to produce the exact location of transition points, although they can work satisfactorily for non-turbulent data.

As said before, our experimental validation is done in two steps. In section 5.2, we show the potential of the singularity exponents in providing a notion of edge, consistent along the scales of a turbulent signal. Then in section 5.3, we prove that better signal reconstruction is achieved from edges obtained through singularity analysis, than from edges obtained through clas-

sical edge detectors. Since we are working with 2D signals, we will limit our justification for the case of images only.

§ 5.2 EDGE DETECTION AND CRITICAL EXPONENTS

As algorithms dedicated to the computation of edges in digital images started to emerge [184, 223, 135, 121, 117, 120, 96, 133, 82, 190, 150, 37, 176, 142], Torre and Poggio [195], while observing that most methods rely on the ill-posed problem of differentiating digital images, proposed a general qualitative description of *edges*: they noted that edges are naturally associated to the concepts of *compact representation* [16, 17, 15], i.e. edges encode most information of an image [50]. Similarly, other authors note that edges represent an image's independent features [22] (similar to the case of 3D modelling where a 2D sketched curve is considered as the basic ingredient [111, 146]). In [195] the authors focus on edge detection as the process of computing derivatives, and, while attempting to do so in a well-posed form, they are led naturally to the problem of prefiltering the image by a (e.g. Gaussian) kernel, which transforms the input signal into a differentiable mapping in the continuous domain, hence allowing the characterization of edges by differential operators. An instance of this formalism is the zero-crossing of second-order derivatives, as in [133, 87, 82, 37, 209, 90, 103], or [5] to cite few, including a recent nonlinear derivative approach (called NLFS) [107]. This formal setting allowed the development of edge characteristics in the framework of differential geometry, a perspective that has become pervasive in image processing [57, 33]. The multiscale nature of edges was recognized very early and it was noted that tracing edge properties across scales would gain insight into the physical process behind image formation. Neurophysics was demonstrating that, in the optical pathway, spatial filters of different sizes operate at the same location [219]. This is related to the processing of information in the early visual system [201], where cells tend to take advantage of the statistical regularities of the input signal in order to get compact representations out of redundancy [10, 205, 206].

The convolution of the input image signal by a Gaussian kernel intro-

duces a scale parameter (the standard deviation of the Gaussian kernel) corresponding to a simple linear scale-space associated to the heat equation. This is often used as an argument for advocating multiscale properties of Gaussian prefiltering [195, 215, 26, 41, 95]. In general, however, the multiscale properties of complex systems do not comply with such an extreme simplification [109]. The advent of scale-space theory in Computer Vision allowed more complex multiscale representations corresponding, among others, to anisotropic diffusion schemes [114, 148, 113, 71], which can incorporate probabilistic models of both sensor noise and operators' responses (to better estimate the gradient's magnitude threshold in case of noise [132]). However the simple example of an image corresponding to the acquisition of a turbulent fluid, like, for instance, a remotely sensed acquisition over the oceans, contains coherent structures associated to the cascading properties of intensive variables in Fully Developed Turbulence (FDT) [217]. It has an associated multiscale hierarchy consisting of sets having a multifractal nature [64] and, as such, cannot be contemplated within a differentiable scale-space framework. Incidentally note that in [52] authors write that an appropriate spatial scale depends upon the local structure of the edge, and thus varies *unpredictably* over the image.

In a seminal paper, Mallat and Zhong [130] relate multiscale Canny edge detection to the local maxima of a wavelet transform and study the completion of multiscale edges associated to the maxima of wavelet coefficients (multiscale edge detection [130, 128]). Local maxima of wavelet coefficients are also used by other authors to form the basis of the Wavelet Transform Modulus Maxima (WTMM) methodology [129], which can be used to relate edges to a concept of *transition* as understood in statistical physics, but, in WTMM, the use of structure functions and moments necessitate large amounts of data for an accurate numerical computation, and, most importantly to our point of view, contains implicitly *ergodicity* hypothesis which can be leveraged for better numerical computations [202]. Moreover, these methods are sensitive to multifractal noise. Note that, edge detection algorithms based on Markov field formulations share also stationarity hypotheses. The use of wavelet coefficients have been more recently extended to include better orientation feature detection through the *X-lets* (i.e. *curvelets* etc.) [188] formulations.

Edge-preserving image smoothing can also be formulated in Bayesian frameworks [112] (and their neural network counterpart [189]) originating from well known reference [72]. We will not review all the Markov formulations in Computer Vision, but we note, for our purpose, that they basically detect transitions in the stationary case, and that the problem of threshold selection can be a difficult one. Edges can also be understood as alignment of Fourier or wavelet phases across scales [136, 105, 211].

In this section, we present a new definition of edge, based on critical exponents defined in statistical physics, consistent across the scales in acquisitions of natural phenomena, such as high-resolution natural images or turbulent acquisitions. Edges belong to the multiscale hierarchy of an underlying dynamics, they are understood from a statistical perspective well adapted to fit the case of natural images. We show that recent developments around the notion of *transition* in nonlinear physics, along with enhanced computational methods of its quantitative parameters (most notably *singularity exponents*) [217], lead to a notion of edge whose consistency can be tested across scales. We give specific attention to the case of turbulent images, whose edges are not well defined in the classical context of edge detection, and we show that in this context the new notions introduced in this article work much better than the previous ones.

5.2.1 Edges, unpredictability and critical exponents

The distribution of critical exponents in a system determines its multiscale properties which are accessible statistically. In particular, the classical notion of gradient, which serves as the basic ingredient in most edge detection algorithm, is not clearly defined in such context and one must find more accurate statistical description of transitions across the scales. This allows us to consider images, and most particularly natural images, as acquisitions of *complex systems* with undetermined extended phase space, and to compute inside the acquired data (images) the quantities known to play a role in the predictability properties of the system. The first step concerns the definition of an appropriate multifractal measure.

As explained in section 4.3, chapter 4, we take the measure as the density

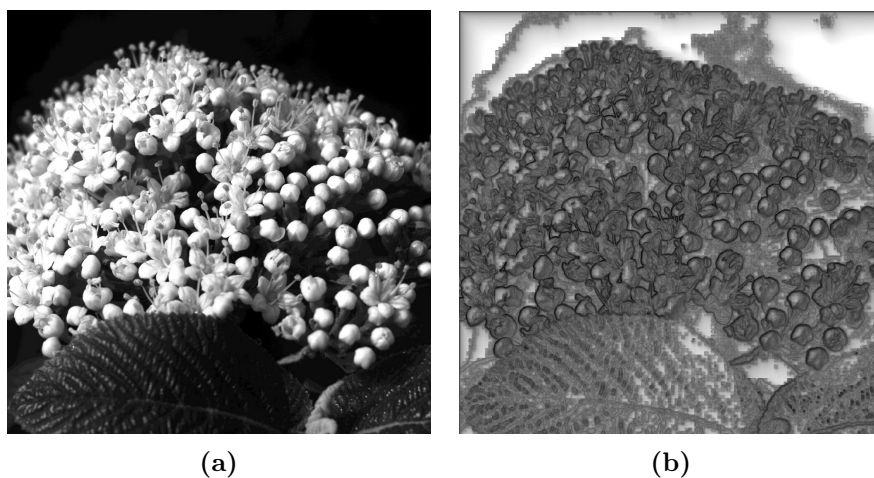


Figure 5.5: (a) Flowers - image *imk01305* of van Hateren database. (b) visualization of the singularity exponents $h(\vec{x})$ computed via Lorentzian wavelet over the image.

function $d\mu(\vec{x})$ defined for a given image I over a ball $\mathcal{B}_r(\vec{x})$ of radius r centered around the point \vec{x} in the given image, as:

$$\mu(\mathcal{B}_r(\vec{x})) = \int_{\mathcal{B}_r(\vec{x})} d(\vec{y}) \|\nabla I\|(\vec{y}) \quad (5.33)$$

such that the measure μ holds true for the following equation:

$$\mu(\mathcal{B}_r(\vec{x})) = \alpha(\vec{x}) r^{h(\vec{x})} + o(r^{h(\vec{x})}) \quad (r \rightarrow 0) \quad (5.34)$$

The exponent $h(\vec{x})$, which is a function of the point \vec{x} , quantifies the multiscale behaviour of the measure μ [203]. The existence of a multifractal measure implies a strong hierarchical organization, with multiscale characteristics, in images. The multiple fractal character shows up when the image is split into different singular components \mathcal{F}_h (refer to equation (4.8), section 4.2.2.1, chapter 4).

This family of sets \mathcal{F}_h is naturally associated to the multiscale hierarchy in a signal and in the case of natural images, there exists a distinguished set of points, called the Most Singular Manifold (MSM), where the features of the system are well recorded [203]. The MSM points are the singularity components associated with the smallest possible value h_∞ and can be interpreted as the most informative set, in the sense that the whole signal can be

reconstructed from the information of the gradients restricted to the MSM. We will denote this set by \mathcal{F}_∞ and it can be expressed as:

$$\mathcal{F}_\infty = \{\vec{x} : h(\vec{x}) = h_\infty = \min(h(\vec{x}))\} \quad (5.35)$$

noting that in digital signals, the value of h_∞ is thresholded and must correspond to a (small) tolerance interval. In practical terms, we write:

$$\mathcal{F}_\infty = \{\vec{x} : h(\vec{x}) \in [h_\infty - \Delta h, h_\infty + \Delta h]\} \quad (5.36)$$

The MSM plays a fundamental role in the multiscale geometrical hierarchy of natural images. Visual inspection of this set reveals a structure which is characterized by the presence of ‘edges’ or contours in natural images [197].

The second step of the approach now concerns on the computation of singularity exponents with high numerical precision.

5.2.1.1 Computation of the singularity exponents

As discussed in section 4.3, chapter 4, the singularity exponents can be obtained by a log-log regression of equation (5.34) as:

$$h(\vec{x}) = \lim_{r \rightarrow 0} \frac{\log(\mu(\mathcal{B}_r(\vec{x}))/\alpha(\vec{x}))}{\log(r)} \quad (5.37)$$

A very fast but crude version of computing $h(\vec{x})$ is known as the Gradient histogram method [202], which takes into account the multifractal measure defined in equation (5.34), at a minimum resolution r_0 . The scale r_0 is chosen such that the whole image corresponds to size 1; in other words, if the image is an array of discretize values of size $m \times n$, one chooses $r_0 = 1/\sqrt{m \times n}$. Approximating $\alpha(\vec{x})$ as the average of the norm of the gradients, an estimate of $h(\vec{x})$ is obtained as:

$$\tilde{h}(\vec{x}) \equiv \frac{\log(\|\nabla I\|(\vec{x})/\langle\|\nabla I\|\rangle)}{\log r_0} \quad (5.38)$$

The method however fails to produce satisfactory results for natural images and is highly sensitive to noise [202]. A better solution would consist in performing the regression on wavelet projection of measures [203], discussed in section 4.3.2, chapter 4. However, a wavelet projection of the measure

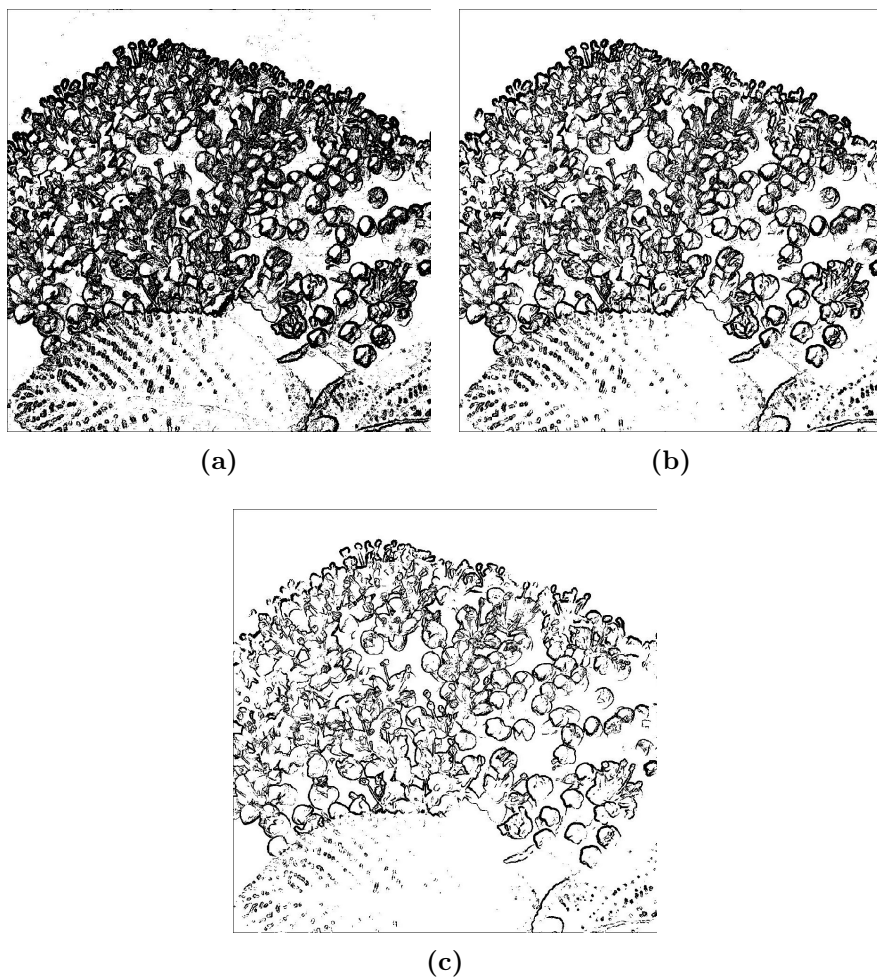


Figure 5.6: *Edges corresponding to the MSM points for the image imk01305 of van Hateren database. (a) compact representation of MSM points corresponding to 35 % pixel density. (b) MSM points corresponding to 25 % pixel density. (c) MSM points corresponding to 15 % pixel density.*

at various scales is costly in computation time and only serves to enhance the resolution of less singular structures at the cost of coarsening the most singular ones [202]. Since the objective is to recover the most singular structures, a better optimized and cost-effective way is to use a point estimation of the singularity exponents. From the perspective of reconstructible systems, good evaluation algorithms come from the observation that the set of most unpredictable points \mathcal{F}_∞ (see equation (5.35)) that provides a perfect

reconstruction is such that [155]:

$$\operatorname{div}(\nabla I|_{\mathcal{F}_c}) = 0. \quad (5.39)$$

where \mathcal{F}_c is the complementary set of \mathcal{F}_∞ . As a consequence, singularity exponents can be called *Local Predictability Exponents*, they encode predictability information [31], like Lyapunov exponents, and are better evaluated in digital signals by one of the following approximation [155, 153]:

$$h(\vec{x}) = \frac{\log(\mathcal{T}_\Psi\mu(\vec{x}, r_0)/\langle\mathcal{T}_\Psi\mu(\cdot, r_0)\rangle)}{\log r_0} + o\left(\frac{1}{\log r_0}\right) \quad (5.40)$$

where $\mathcal{T}_\Psi\mu(\vec{x}, r_0)$ is the wavelet projection of the measure μ at scale r_0 and point \vec{x} (see section 4.3.2), $\langle\mathcal{T}_\Psi\mu(\cdot, r_0)\rangle$ is the average value of the wavelet projection over the measure and r_0 is chosen to diminish the relative amplitude of the correction term $o\left(\frac{1}{\log r_0}\right)$. The preferred wavelet of choice are the wavelets from the family $\Psi^\beta(\vec{x}) = 1/(1 + |\vec{x}|^2)^\beta$ (for $\beta = 1, 2, 3, 4$), and averaging the resulting coefficients.

Algorithm 2 Edge detection: Finding the MSM points

Step 1: Normalize an input image I as: $I(\vec{x}) - \langle I \rangle$.

Step 2: Compute the singularity exponents $h(\vec{x})$, at each point \vec{x} on the image I , from equation (5.40).

Step 3: Determine the value of the most singular exponent h_∞ from the distribution of the singularity exponents $h(\vec{x})$ by sorting them and determining the appropriate quantile corresponding to the desired density.

Step 4: Define the density function $\delta_{\mathcal{F}_\infty}$ as: $\delta_{\mathcal{F}_\infty}(\vec{x}) = 1$ if $h(\vec{x}) \approx h_\infty$; $\delta_{\mathcal{F}_\infty}(\vec{x}) = 0$ otherwise.

Step 5: $\delta_{\mathcal{F}_\infty}(\vec{x})$ is a binary mask that locates the MSM points.

The singularity exponents of an experimental image is shown in Fig 5.5. Fig 5.6 shows the MSM points, with different densities, for an experimental image (imk01305 of the van Hateren image database [206]). The procedure for computing the MSM points, corresponding to the edge pixels of an image, is presented in algorithm 2.

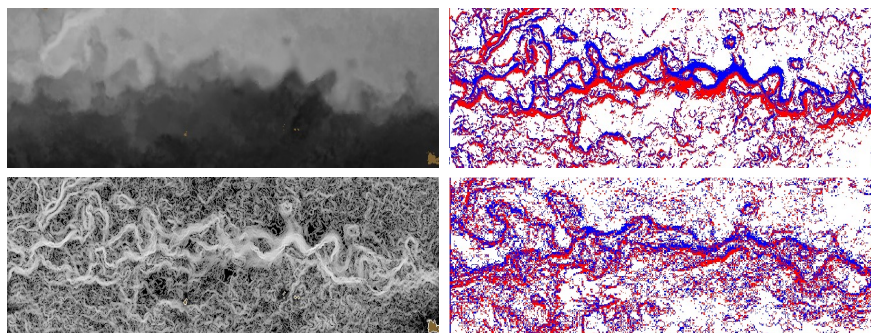


Figure 5.7: *This figure illustrates the complexity of edge detection in the case of turbulent images. The edge pixels are marked red or blue according to the sign of the scalar product between the normal to the set of edge and the image gradient at that point. **Top row** (from left to right): an excerpt from the sea surface temperature (SST) image (MODIS data) of the Agulhas current below the coast of South Africa, set of edge pixels computed by MSM corresponding to 25% of pixel density in the selected area. **Bottom row** (from left to right): singularity exponents of the SST image, edges produced by algorithm NLFS [107] which behaves the best among the classical edge operators tested (see table 5.8). The coherent structures are not respected by NLFS, showing the superiority of MSM.*

5.2.1.2 Comments: The case of turbulent signals

Examination of the results for SST (turbulent phenomena) images are particularly interesting: an edge in a turbulent signal is poorly characterized by a filter's response to step functions, and the case of Fully Developed Turbulence is paradigmatic for the existence of a multiscale hierarchy associated to cascading dynamics of physical variables [64]. Tuning with the scale-space parameter given by the kernel's standard deviation modifies the input signal incoherently w.r.t. to the real multiscale hierarchy present in the data. Universality classes are not well characterized by the transitions associated to classical edge operators. We compare with the NLFS operator [107] due to its superior performance over the other classical edge detectors and robustness to noise.

NLFS is a non-linear approach to edge detection. The method aims at the localization of edge pixels in a signal, according to the sign of the slope of the

transition, with simultaneous noise cancellation. For this two filters are used: one for detecting the positive-slope edge points and the other for detecting the negative-slope edge points. The result are two signals containing positive and negative variations. In the case of limited noise the disturbances are detected, by these positive and negative variations of the signal, as peaks at the same location and are thereby removed. In Fig 5.7, we show an extended part of the SST data and illustrate the sensitivity of edge detection between MSM and NLFS.

5.2.2 Edge consistency across the scales

Edges are primary features naturally associated to scale invariant properties of natural images, specifically in the case of turbulent signals where symmetry is restored only in statistical sense [201, 64]. As a consequence, the algorithms used in computing edge features should be consistent across the scales: if one has different acquisitions of a same phenomenon at different scales, the resulting edge pixels computed by these algorithms must produce matching edge pixels accross the scales. To check this, we set up an experiment where a same signal at different resolution is generated and their outputs produced by some classical edge detection algorithms are evaluated. To generate the different resolutions, we use two methods. The first one consists in computing a multiscale version of the signal by using a standard Haar discrete wavelet transform [128]. The second one consists in using the well-known linear scale-space representation developed by Lindeberg *et al* [115, 116]. A linear scale-space family $L(., t)$ associated to an original signal f is obtained by convolving f with a Gaussian kernel g such that:

$$L(., t) = g(., t) * f \quad (5.41)$$

where the Gaussian kernel is given by

$$g(x, t) = \frac{1}{2\pi t} e^{-(x^2+y^2)/2t} \quad (5.42)$$

and $t > 0$ is the scale parameter.

We take two images: the clock image from SIPI image database [3], which is a standard rigid object, and an excerpt of the SST image. The SST image corresponds to the acquisition of a turbulent phenomenon, for which the

Table 5.1: Inconsistent behaviour of edges along the scales. Image used is an excerpt from the sea surface temperature (SST) image. Different resolutions of the SST image are the approximation coefficients resulting from a standard Haar discrete wavelet transform. We show the results of the following edge detection algorithms: MSM (proposed edge detection algorithm), Canny and multiscale Canny (mC) edge detection [130]. D corresponds to the pixel density of the respective edges. For edges computed using Canny edge detector, α specifies the lower sensitivity threshold and σ is the standard deviation of the Gaussian filter.

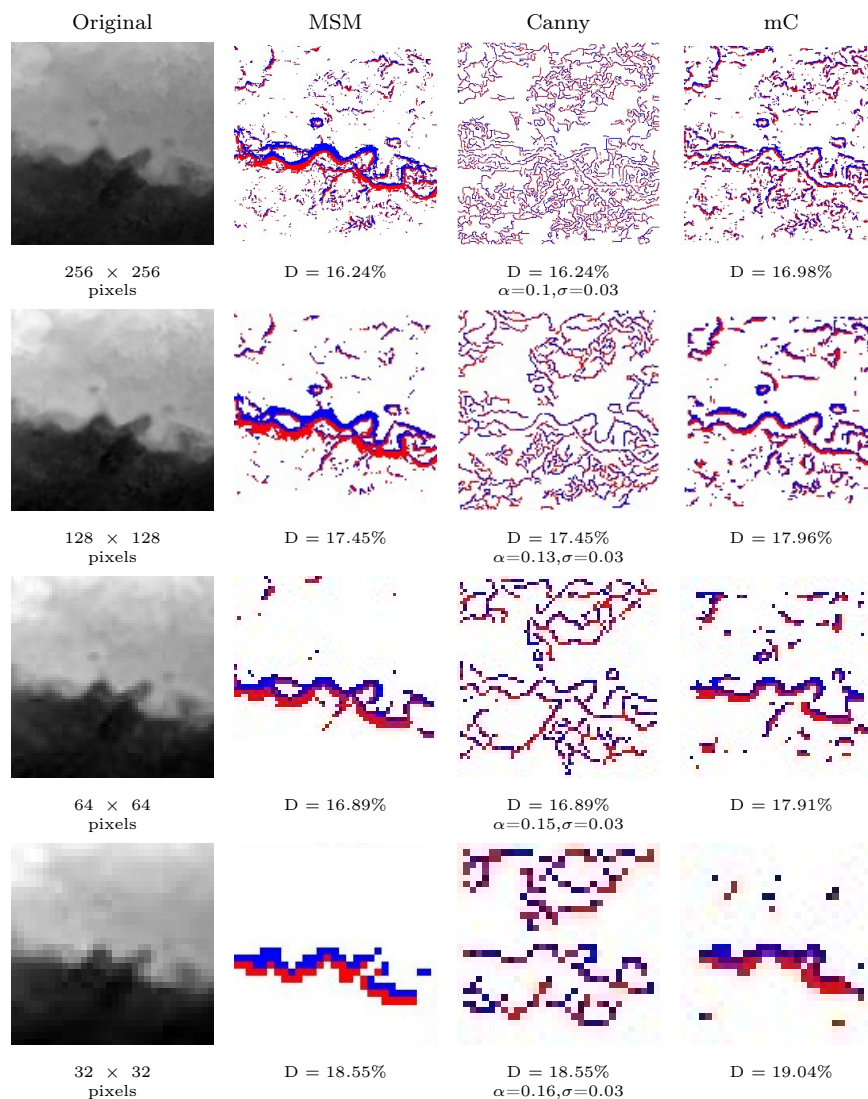
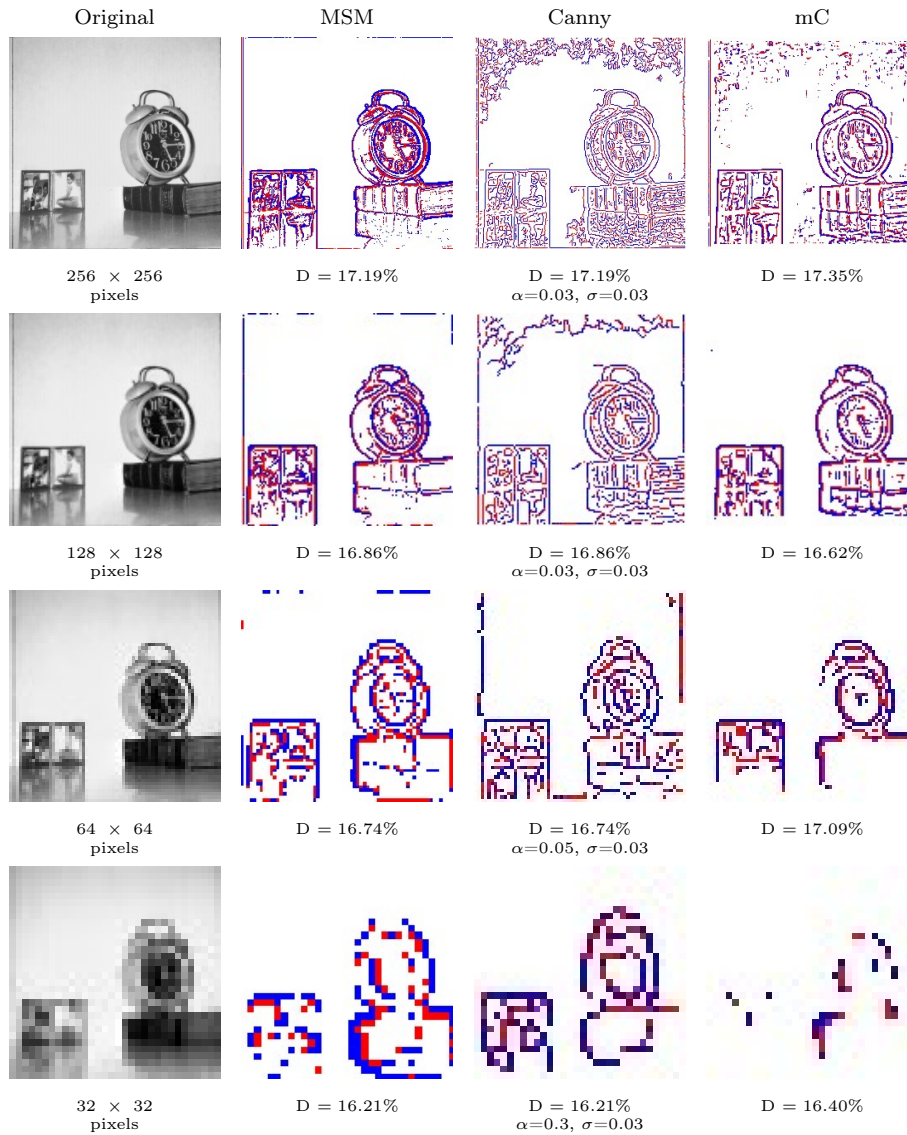
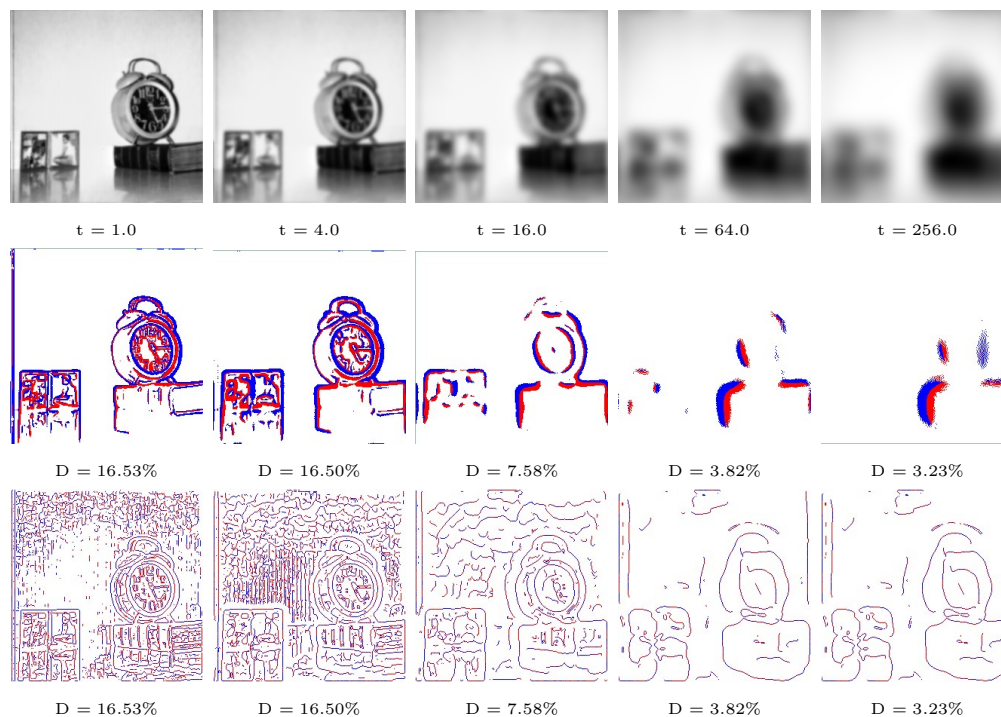


Table 5.2: Inconsistent behaviour of edges along the scales. *Image used is the clock image from SIPI image database [3]. Different resolutions of the clock image are formed by taking the approximation coefficients of Haar discrete wavelet transform.*



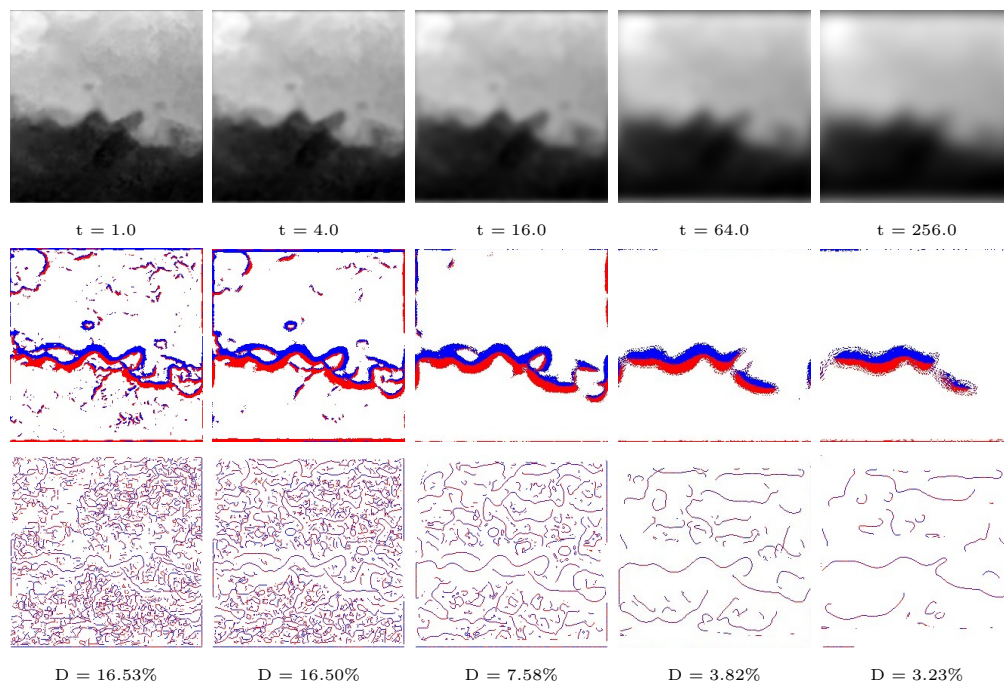
existence of a multiscale hierarchy comes from the turbulence associated to Navier-Stokes equations [64]. The results for the SST image are shown in Table 5.1. In this table are displayed (left column) the SST image at various

Table 5.3: Evaluation of edge consistency across scales using Lindeberg [115] scale space representation. Row 1 (from left to right): different resolutions of the clock image obtained by changing the scale parameter t (explained in section 5.2.2). Row 2: compact representation of MSM points. Row 3: edges computed using Lindeberg edge detector.



resolutions using the Haar discrete wavelet transform. Columns 2, 3 and 4 show the edge pixels produced by three different algorithms: the algorithm called MSM, which is the proposed edge detection algorithm (explained in subsection 5.2.1.1), classical Canny edge detector (column 3) and the Mallat-Zhong edge detection technique [130], also known as multiscale Canny edge detection (which is also related to the WTMM (Wavelet Transform Modulus Maxima) [129] method). It is clear from these results that Canny edge pixels are not consistent across the scales: first the boundary of the main coherent structure (the temperature front depicted by the boundary between the dark and light area) is not properly described by Canny edge pixels across the scales. Second, it is difficult to match the corresponding edge pixels across the scales. This can, however, be related to the fact that Canny edge

Table 5.4: Evaluation of edge consistency across scales using Lindeberg scale space representation. Row 1 (from left to right): different resolutions of the SST image obtained by changing the scale parameter t . Row 2: compact representation of MSM points (pixel density fixed at 16%). Row 3: edges computed using Lindeberg edge detector.



detector encodes all edges regardless of scale, and that is why we also use multiscale Canny in our comparison. Considering the multiscale Canny edge pixels, they behave more consistently compared to Canny edge pixels, but they are still outperformed by MSM, the latter being specifically designed to retain consistency across the scales. Note that in Table 5.1, MSM points encode in a particularly efficient way the main boundary of the temperature front across the scales. The same is reproduced in Table 5.2 on the clock image, with similar results. In Table 5.3 and Table 5.4, we make a similar comparison between the MSM points and the edges produced by the multiscale edge detection of Lindeberg [115]. Here again, we see that in both cases, consistency across the scales is better achieved by MSM. In Table 5.4, the density of the MSM points are kept around 16% precisely; but because

Lindeberg edges take the zero-crossings of image intensity, further filtered by a third order directional derivative, the number of candidate edge pixels are automatically reduced with increased blurring, resulting in a limited density across the scales. From these experiments we see that, specially in the case of acquired turbulent phenomena, some classical edge detection algorithms, even those based on linear scale-space theory, do not behave consistently across the scales.

In this context, one might argue about a comparison with Elder-Zucker's algorithm [52]. Elder-Zucker's algorithm on the detection of edges is inspired by its own local scale control method that determines a unique scale, as a function of filter scale σ , for local estimation at each point in an image [52, 51]. Therefore, a *minimum reliable scale* i.e., a filter with smallest standard deviation σ that can be used reliably, is being determined for each point in the gradient map and used locally to derive logical inferences from derivative estimates of the signal (that are key to edge detection). The choice of σ and the definition of reliability rest with the prior computation of a *critical value function* that depends on some statistical parameters [50]. A good choice of these statistical parameters are necessary for the proper functioning of the algorithm; incorrect estimate may lead to reduced performances. The performance of MSM, on the other hand, is independent of the choice of any *a priori* inputs and is applied directly on different scale-based representation of images (without doing any processing to enhance the performance of edge detection) and verify its performance across scales. We are interested in extracting the most singular components that are related to edges in an image (by proper computation of singularity exponents on the image), irrespective of the scale or the spatial representation of the image.

In this section, we have shown that critical exponents defined in statistical physics lead to a coherent definition of edges, consistent across the scales in acquisitions of natural phenomena, such as high-resolution natural images or turbulent acquisitions. Edges belong to the multiscale hierarchy of an underlying dynamics, they are understood from a statistical perspective well adapted to fit the case of natural images. In the next section, we will prove that this new definition edge outclass the performance of classical edge detectors in terms of reconstructing an image from its edge representation.

§ 5.3 RECONSTRUCTING AN IMAGE FROM ITS EDGE REPRESENTATION

Early methods dedicated to the reconstructability of signals from their edge pixels lacked completeness in terms of compact representation and failed to provide a near estimate of the original signal [50]. The first theoretical instance of reconstructing a one-dimensional signal from its zero-crossing was found in the Logan theorem [118]. Logan proved that for a signal which is one-dimensional and strictly band-limited to a single octave, the time of the zero-crossings can form a complete representation of the signal and are sufficient candidates to reconstruct the signal. The findings of Logan were used in [133] to further investigate the possibility of complete representation of an image from the zero-crossings and gradient magnitudes of the image, convolved with a Laplacian of Gaussian (LoG) filter, at multiple scales. The proof of the theoretical completeness of the zero-crossing was further extended to the case of one-dimensional finite polynomial signal [218] and for a restricted class of band-limited two-dimensional signals [43].

It was acknowledged, however, in [118] that “the problem of actually recovering functions from their zero-crossing appears to be difficult (to say the least), under the most general conditions of uniqueness”. The completeness of zero-crossings in representing an image feature and its ability to produce stable reconstructions, in practice, was further argued in [89]. In [38] an algorithm was introduced that computes an approximate reconstruction of an image from information coded at the image edges. The edges were computed in a manner quite similar to [133], but were further thresholded based on outputs from gradient based filters [50]. The method however lacked completeness to a large extent and was reintroduced in [39] by modifying the edge representation from a sub-sampled low-pass residual image [50]. In [221], it was proposed that images are well represented by the partial information confined to zero-crossings and a new reconstruction technique was proposed. The results, although better than the previous techniques [38, 39], lacked completion. A method based on minimizing equation error for stable reconstruction of image, from the restriction of its gradient measure over edges,

was proposed in [89]. A new contour based image reconstruction technique was proposed in [76], by taking the edge as a Gaussian-blurred step discontinuity and considering a number of parameters, like luminance, brightness, contrast, blur and ‘contour width’ [50], in the process of calculating them. In a seminal paper, Mallat and Zhong [130] described an algorithm to reconstruct images from their multiscale edges; the edges were detected by applying local maxima on a wavelet transformed version of the image. While this representation is far more compact in the case of 1-D signals, it misses certain details and some defocused structures are not recovered [50] in the case of images.

In [197], the authors have proposed a new technique of image reconstruction from their edges, based on the most informative fractal set contained within an image. Inspired by the quality of the reconstruction achieved by them, we have moved on to define an alternate approach to derive a similar reconstruction formula as in [197, 203]. The derivation of the new approach, tries to relate the concept of Poissonian diffusion to image reconstruction from edges and has equivalent performance as that in [197, 203].

When an intensity image $I(x, y)$ is considered as a mathematical surface [208], edges can be detected as irregular distribution of intensity values over this surface. The idea of constructing complete surface specifications from the information contained in the zero-crossings was illustrated in [79]. In fact, a common surface reconstruction technique of regularization has been exploited in an attempt to reconstruct from contour line information [140], and in [175], a regularized fusion approach to the problem of reconstruction from color edge maps was applied. In this context, one should mention about 3D modelling of objects from

In this section, we test the performance of different edge detection algorithms through the framework of *reconstructible systems*. We show that ‘state-of-the-art’ surface reconstruction techniques, like fast Poisson solver [73], M-estimator, regularization [4] and diffusion [212], can be successfully applied to reconstruct images from their edge representation. In the process, we study image reconstruction from edge pixel data that better suits turbulence.

5.3.1 Framework of Reconstructible Systems

5.3.1.1 Problem Formulation

Let f_x, f_y denote a given non-integrable¹ gradient field over a $L \times B$ rectangular grid of image pixels. Given f_x, f_y , the goal is to obtain an image I , such that ∇I is “as close as” possible to the vector field (f_x, f_y) . Let I_x, I_y denote the gradient field of I . Note that in our experiments f_x, f_y represents the density of the gradient measure corresponding to the MSM i.e., $f_x = I_x \delta_{\mathcal{F}_\infty}$ and $f_y = I_y \delta_{\mathcal{F}_\infty}$, where $\delta_{\mathcal{F}_\infty}$ stands for the standard density measure restricted to the set \mathcal{F}_∞ i.e., $\delta_{\mathcal{F}_\infty}$ denotes the Dirac measures associated to the set \mathcal{F}_∞ . A common approach is to minimize the least squares error function such that:

$$\operatorname{argmin}_I \int \int ((I_x - f_x)^2 + (I_y - f_y)^2) dx dy \quad (5.43)$$

The associated Euler-Lagrange equation gives the Poisson equation:

$$\operatorname{div}(I_x, I_y) = \operatorname{div}(f_x, f_y) \quad (5.44)$$

where ‘div’ refers to the divergence operator and is defined as $\operatorname{div}(f_x, f_y) = \frac{\partial f_x}{\partial x} + \frac{\partial f_y}{\partial y}$. The aim of all the reconstruction algorithms is to find a solution for (I_x, I_y) of equation (5.44) which minimizes the error function in equation (5.43).

5.3.1.2 Linear systems

In this section, we try to summarize some existing techniques for reconstruction from a given gradient field. Readers are referred to [73, 4, 148] for a more detailed explanation of the algorithms.

Fast Poisson solver : A well known approach to solving the Poisson equation was proposed in [73]. The idea is to project the non-integrable gradient field on to a set of integrable slopes using discrete cosine functions. The Poisson equation can be written as $\frac{\partial^2 I}{\partial x^2} + \frac{\partial^2 I}{\partial y^2} = f(x, y)$, where $f(x, y) = \operatorname{div}(f_x, f_y)$

¹In the sense that the differential form $f_x dx + f_y dy$ is not supposed to be exact.

is the divergence of the gradient field. An associated finite difference equation reads:

$$I_{j+1,l} + I_{j-1,l} + I_{j,l+1} + I_{j,l-1} - 4I_{j,l} = f_{j,l} \quad (5.45)$$

where every coefficient can be expanded with the 2D discrete cosine transform as:

$$I_{j,l} = \frac{4}{JL} \sum_{m=0}^{J-1} \sum_{n=0}^{L-1} \hat{I}_{m,n} \cos \frac{\pi jm}{J} \cos \frac{\pi ln}{L} \quad (5.46)$$

Substituting the values of the expansion coefficients in equation (5.45), we get the final solution as

$$\hat{I}_{m,n} = \frac{\hat{f}_{m,n}}{2(\cos \frac{\pi m}{J} + \cos \frac{\pi n}{L} - 2)} \quad (5.47)$$

M-estimator : M-estimators is viewed as an iterative re-weighted least square solution [4] and can be written as:

$$\operatorname{argmin}_{\mathbf{I}} \int \int (w(\epsilon_x^{k-1})(I_x - f_x)^2 + w(\epsilon_y^{k-1})(I_y - f_y)^2) dx dy \quad (5.48)$$

where the weights at each iteration k depends on the residual at iteration $k-1$ i.e., $|\epsilon_x^k| = |I_x^{k-1} - f_x|$ and $|\epsilon_y^k| = |I_y^{k-1} - f_y|$. The weights $w_x = w(\epsilon_x^{k-1})$, $w_y = w(\epsilon_y^{k-1})$ are calculated using Huber function [81]. Applying Euler-Lagrange over equation (5.48) we get $\operatorname{div}(w_x I_x, w_y I_y) = \operatorname{div}(w_x f_x, w_y f_y)$. I can then be recovered by solving the linear equation $L_w I = f_w$, where $f_w = \operatorname{div}(w_x f_x, w_y f_y)$ and L_w is the sparse Laplacian matrix of size $LB \times LB$.

Regularization : The L^2 regularization can be written as [4]:

$$\operatorname{argmin}_{\mathbf{I}} \int \int ((I_x - f_x)^2 + (I_y - f_y)^2 + \alpha(\phi(I_x) + \phi(I_y))) dx dy \quad (5.49)$$

where α is called the regularization parameter using function ϕ . Some commonly used variations of ϕ are $\phi(d) = \sqrt{1 + d^2}$ and $\phi(d) = \log(1 + d^2)$. Applying Euler-Lagrange to equation (5.49) and after simplification, the solution can be achieved by iterative minimization [4].

Anisotropic diffusion : The anisotropic diffusion equation, commonly defined as $I_t = \text{div}(c(x, y, t)\nabla I)$, of [148] was generalized in [212] as $I_t = \text{div}(c\nabla I)$, where c is the diffusion tensor and can be defined as a 2×2 symmetric, positive-definite matrix at each pixel. A generalized Poisson equation using c was proposed in [4] as

$$\text{div}\left(c \begin{bmatrix} I_x \\ I_y \end{bmatrix}\right) = \text{div}\left(c \begin{bmatrix} f_x \\ f_y \end{bmatrix}\right) \quad (5.50)$$

Several methods have been proposed for obtaining the diffusion tensor c . The method followed in [4] suggests an edge preserving diffusion tensor at each pixel, by convolving component wise $\begin{bmatrix} f_x^2 & f_x \times f_y \\ f_x \times f_y & f_y^2 \end{bmatrix}$ with a Gaussian kernel. The final solution is given by $L_c I = f_c$, where $f_c = \text{div}\left(c \begin{bmatrix} f_x \\ f_y \end{bmatrix}\right)$ and L_c is the Laplacian matrix.

5.3.2 Reconstruction from MSM (\mathbf{R}_{msm})

In this section, we turn back to the propagator introduced in [197], and derive a parallel propagator from the concept of Poisson equation applied to surface reconstruction problems from non-integrable gradient fields. We consider the gradient measure of the signal $\nabla I(\vec{x})$ and integrate it over the set of most unpredictable points \mathcal{F}_∞ . A practical expression for the reconstruction formula is given by [197]:

$$I(\vec{x}) = \int \langle \vec{g}(\vec{x} - \vec{y}) | \nabla_\infty I(\vec{y}) \rangle d\vec{y} = \vec{g} * \nabla_\infty I(\vec{x}) \quad (5.51)$$

where $\int_{\mathcal{F}_\infty} d\vec{y}$ means integration over the MSM, \vec{g} represents the desired propagator. The essential gradient of the signal $\nabla_\infty I(\vec{x})$ is defined as the following distribution:

$$\nabla_\infty I(\vec{x}) = \nabla I(\vec{x}) \delta_{\mathcal{F}_\infty}(\vec{x}) \quad (5.52)$$

where $\delta_{\mathcal{F}_\infty}(\vec{x})$ is the density of the gradient measure restricted to the MSM. Accordingly, equation (5.51) can be expressed in the Fourier domain as:

$$\hat{I}(\vec{\omega}) = \langle \hat{\vec{g}}(\vec{\omega}) | \widehat{\nabla_\infty I}(\vec{\omega}) \rangle \quad (5.53)$$

where $\hat{\cdot}$ represents the Fourier transform.

To derive an exact formulation for the reconstruction kernel \hat{g} , we begin with the idea presented in [197, 203], but follow the derivation presented in [4] (in the case of differentiable fields), so that it relates in an interesting way Poisson diffusion and the reconstruction from the MSM explained in [197, 203]. In that context, one seeks a smooth vector field \vec{f} defined over the whole image and which minimizes the L^2 distance with the original gradient $\nabla I(\vec{x})$ and can be expressed as

$$\operatorname{argmin}_{\vec{f}} \int \int (\nabla I(\vec{x}) - \vec{f}(\vec{x}))^2 d\vec{x} \quad (5.54)$$

We then follow the derivation explained in [4] to get a version of the reconstruction kernel \hat{g} in the smooth case. Taking the Euler-Lagrange variational formulation of equation (5.54) we get

$$\operatorname{div}(\nabla I)(\vec{x}) = \operatorname{div}(\vec{f})(\vec{x}) \quad (5.55)$$

Taking the Fourier transform of equation (5.55), we get as in [4]

$$\hat{I}(\vec{\omega}) = -i \frac{\omega_x \hat{f}_x(\vec{\omega}) + \omega_y \hat{f}_y(\vec{\omega})}{\omega_x^2 + \omega_y^2} \quad (5.56)$$

where the vector field $\vec{f}(\vec{x})$, after Fourier transformation gives rise to a complex vector field $\hat{\vec{f}} = (\hat{f}_x(\vec{\omega}), \hat{f}_y(\vec{\omega}))$. For $\vec{\omega}_0 = (\omega_x = 0, \omega_y = 0)$, $\hat{I}(\vec{\omega}_0)$ is undefined, which corresponds to the mean of I (DC component). We set a null value in this case. Comparing with equation (5.53), this suggest the kernel as

$$\hat{g}(\vec{\omega}) = \frac{\vec{\omega}}{i \|\vec{\omega}\|^2} \quad (5.57)$$

and we have the final expression of the reconstruction formula over the MSM \mathcal{F}_∞ i.e., R_{msm} , in the Fourier domain, as:

$$\hat{I}(\vec{\omega}) = \frac{\langle \vec{\omega} | \widehat{\nabla_\infty I}(\vec{\omega}) \rangle}{i \|\vec{\omega}\|^2} \quad (5.58)$$

Fourier inversion of this formula gives the reconstruction of the image from the restriction of the gradient field to the MSM. It should be noted that the

Table 5.5: Images used for our experiments. Row 1 (from left to right): *Harrington weave, Hibiscus, Car, Lena, Turbulence degraded atmospheric phase, imk01310, imk03324, imk04050. Row 2:* *Brick wall, House, imk03322, Boat, Camille, Aerial view of a truck, Julia Roberts, Sea Surface Temperature (SST) image of the Agulhas current below the coast of South Africa. Image description is available in table 5.6.*



MSM edge points are defined irrespective of any reconstruction formula. In fact, $\delta_{\mathcal{F}_\infty}$ holds true for edges detected by any edge detector and can be incorporated likewise to create f_x, f_y and subsequently perform reconstruction. The algorithmic formulation of R_{msm} is presented in algorithm 3, below.

Algorithm 3 Reconstructing the signal from the MSM

- Step 1:** Calculate the singularity exponents $h(\vec{x})$ for every point \vec{x} in the image.
Step 2: Determine h_∞ .
Step 3: Define the density function $\delta_{\mathcal{F}_\infty}$ as the mask relative to the set \mathcal{F}_∞ .
Step 4: Calculate the field $\nabla_\infty I(\vec{x}) = \nabla I(\vec{x})\delta_{\mathcal{F}_\infty}(\vec{x})$ i.e., the values of the gradient over the MSM.
Step 5: Go to Fourier domain to obtain $\widehat{\nabla_\infty I}(\vec{\omega}) = (\widehat{\nabla_\infty I_x}(\vec{\omega}), \widehat{\nabla_\infty I_y}(\vec{\omega}))$.
Step 6: Calculate the scalar product $\vec{\omega} \cdot \widehat{\nabla_\infty I}(\vec{\omega}) = \omega_x \widehat{\nabla_\infty I_x}(\vec{\omega}) + \omega_y \widehat{\nabla_\infty I_y}(\vec{\omega})$.
Step 7: Calculate $\hat{I}(\vec{\omega}) = \frac{\langle \vec{\omega} | \widehat{\nabla_\infty I}(\vec{\omega}) \rangle}{i\|\vec{\omega}\|^2}$ with $\omega^2 = \omega_x^2 + \omega_y^2$.
Step 8: Do an inverse Fourier transform of $\hat{I}(\vec{\omega})$ to obtain $I(\vec{x})$.
-

5.3.3 Computational complexity

R_{msm} is essentially based on Fourier transform computation. We use fast Fourier transform (FFT) where the computational complexity is $N \log N$,

N being the total number of pixels in the image. We use FFT only once in our operation and very fast implementations of FFT already exists e.g. Fastest Fourier Transform in the West (FFTW). Poisson solver is using the discrete cosine transform (DCT) instead of FFT. The other solvers are using one or more linear systems (e.g. M-estimator is using 7 – 8 iterations) and the complexity depends on the solvers used. Multigrid solvers are the fastest solvers available till now, with the complexity $o(N)$, but still their fastest implementations are slow compared to the fastest implementations of FFT.

5.3.4 Choice of images

Images of different entities are chosen trying to cover a broad spectrum of natural images starting from textures (Harrington weave) to an object (Brick wall, House, Car), landscape (imk01310, imk03322, imk03324), aerial view (Truck), face (Julia Roberts, Camille, Lena) and turbulent acquisitions of signals (sea surface temperature, turbulence degraded atmospheric phase) as is shown in table 5.5. These experimental images are chosen from standard databases like SIPI image database [3], CMU image database [1] and the van Hateren database [206]. The description of the images are given in table 5.6.

5.3.5 Results

In this section, we discuss about the experiments performed. We perform three sets of experiment on different natural images (described in section 5.3.4). Visual quality of the reconstructed images are evaluated based on the structural similarity index metric (SSIM) [210]. The SSIM measure between two windows x and y of similar size $N \times N$ is:

$$\text{SSIM}(x,y) = \frac{(2\mu_x\mu_y + c_1)(2\sigma_{xy} + c_2)}{(\mu_x^2 + \mu_y^2 + c_1)(\sigma_x^2 + \sigma_y^2 + c_2)} \quad (5.59)$$

where μ_x, μ_y are the average of x and y ; σ_x^2, σ_y^2 are the variance of x and y ; σ_{xy} the covariance of x and y ; c_1 and c_2 are two normalizing parameters. We also illustrate the pertinence of the framework of reconstructible systems for evaluating an edge operator's compact representation effectiveness using the *mean square error* (MSE) and *peak signal to noise ratio* (PSNR, expressed

Table 5.6: Description of the experimental images shown in table 5.5.

Image	Size	Source
Harrington weave	1024 × 1024 pixels	SIPI image database
Hibiscus	512 × 512 pixels	SIPI image database
Car	260 × 320 pixels	CMU image database
Lena	512 × 512 pixels	SIPI image database
Phase	128 × 128 pixels	French aerospace lab ONERA
imk01310	512 × 512 pixels	van Hateren database
imk03324	512 × 512 pixels	van Hateren database
imk04050	512 × 512 pixels	van Hateren database
Brick wall	512 × 512 pixels	SIPI image database
House	256 × 256 pixels	SIPI image database
imk03322	512 × 512 pixels	van Hateren database
Boat	512 × 512 pixels	SIPI image database
Camille	256 × 256 pixels	Internet download
Aerial view of a truck	512 × 512 pixels	SIPI image database
Julia Roberts	256 × 256 pixels	Internet download
Sea surface temperature (SST) image	512 × 512 pixels	MODIS acquisition of the Agulhas current below the coast of South Africa

in decibels dB) defined by:

$$\text{MSE} = \frac{1}{m \times n} \sum_{i,j} |I(x_{i,j}) - I_r(x_{i,j})|^2 \quad (5.60)$$

$$\text{PSNR} = 20.0 \times \log_{10} \frac{\max(I(\vec{x}))}{\sqrt{\text{MSE}}} \quad (5.61)$$

where $I_r(x)$ represents the reconstructed image.

The three sets of experiments performed, are discussed elaborately with results in ‘Experiment 1’, ‘Experiment 2’ and ‘Experiment 3’ in the subsequent sections. In Experiment 1, we test the quality of the edges obtained from different edge detectors in terms of reconstructibility of the whole image from its edges. In Experiment 2, we test the performance of R_{MSM} over classical

surface reconstruction techniques in its ability to reconstruct the image from edges. Finally, in Experiment 3 we test the best possible combination (edge detector + reconstructor) that gives the best reconstruction results.

It should be noted that we do not use any kind of denoising while testing the performance of our reconstruction algorithm over noisy gradient data, as we wanted to check the robustness of our algorithm in the presence of noise. With the use of denoising the results may differ, but if we denoise the gradients it will still be a non-integrable gradient field. This means reconstructing from them will still introduce artifacts.

Experiment 1

In this experiment we try to study the performance of our edge detection algorithm over all the previous declined versions encountered in image processing in terms of reconstructibility of the whole image from its edges. The classical edge algorithms tested are Matlab[©] implementations. Reconstruction is performed over edges, calculated from different edge detection algorithms, using R_{msm} . The pixel density of the edges calculated using different edge detectors are kept within a close range (given the constraint imposed by the Gaussian sigma), with the pixel density of MSM points kept lowest.

Discussion

Reconstruction results over edges obtained from different edge detectors are shown in table 5.8. Performance of the reconstruction under different levels of noise (SNR = 26 dB, 14 dB and 6 dB) is shown in Table 5.9. Visual quality of the reconstructed images, shown in Table 5.8 and Table 5.9, are evaluated based on SSIM [210]. SSIM's for the reconstructed images show that MSM outperforms the classical edge detectors in majority of the cases. Similar conclusion is derived from the quantitative analysis of the results, using MSE and PSNR metrics, as shown in Table 5.7 and Table 5.10. The performance of NLFS is sometimes better in the noisy environment (as seen in Table 5.10), due to the algorithm's natural configuration to noise cancellation. MSM, however, outperforms it in majority of the cases.

Tested classical edge detection algorithms are reviewed in this experiment in the sense that they lack compact representation. It happens that MSM points lead, for most images used in this experiment, the best quantitative results in terms of PSNR, SSIM and MSE. But MSM points are defined irrespective of any reconstruction formula. Consequently, the eval-

Table 5.7: Quantitative analysis: *Evaluation of the reconstruction over different edge detection algorithms, in terms of PSNR and MSE, corresponding to Table 5.8. D represents the pixel density of the edges.*

Image	Params	MSM	NLFS [107]	Canny	Lindeberg [115]	LoG	Sobel	Prewitt
Weave (1024 × 1024 pixels)	D (%) MSE PSNR (dB)	31.5 0.1439 17.38	32.87 0.1977 16.01	29.56 0.6600 10.76	31.86 0.3955 13.99	31.28 0.2790 14.51	31.57 0.2148 15.64	31.67 0.2158 15.62
Hibiscus (512 × 512 pixels)	D (%) MSE PSNR (dB)	28.55 0.0906 22.43	28.87 0.0944 21.92	28.55 0.4005 16.04	29.15 0.3139 17.04	29.98 0.2657 17.76	29.43 0.1690 19.72	29.22 0.1622 19.80
Car (260 × 320 pixels)	D (%) MSE PSNR (dB)	30.00 0.0794 25.59	36.03 0.1321 23.37	32.28 0.7350 15.84	36.28 0.3972 18.68	37.58 0.4038 18.53	36.86 0.2150 21.26	37.24 0.2262 21.04
Lena (512 × 512 pixels)	D (%) MSE PSNR (dB)	32.00 0.0563 21.17	32.93 0.0587 20.99	28.80 0.5898 10.98	32.20 0.3718 12.98	32.36 0.3775 12.91	30.13 0.2298 15.06	30.26 0.2305 15.05
imk01310 (512 × 512 pixels)	D (%) MSE PSNR (dB)	30 0.0626 29.43	30.12 0.0923 27.74	27.98 1.1389 16.88	31.09 1.0744 17.08	31.24 0.9434 17.65	29.90 0.2150 24.07	30.40 0.1933 24.53
imk03324 (512 × 512 pixels)	D (%) MSE PSNR (dB)	30.00 0.0854 23.08	30.14 0.1057 22.15	32.48 0.7808 13.42	35.43 0.3879 16.51	36.46 0.3168 17.38	36.06 0.1634 20.26	36.82 0.1705 20.07
imk04050 (512 × 512 pixels)	D (%) MSE PSNR (dB)	31.00 0.0652 25.79	31.32 0.0974 24.05	31.22 0.4634 17.23	32.59 0.3554 19.17	32.95 0.2996 22.60	32.61 0.1358 20.50	32.93 0.1361 22.59
Phase (128 × 128 pixels)	D (%) MSE PSNR (dB)	25.00 0.0184 23.97	27.27 0.0187 23.14	24.63 0.8025 7.08	23.62 1.3023 5.29	29.15 0.9307 5.34	25.91 0.1660 14.24	25.42 0.1745 14.02
SST (512 × 512 pixels)	D (%) MSE PSNR (dB)	25.00 0.0114 23.99	30.73 0.0404 18.50	21.62 0.8105 5.56	22.64 0.8257 5.40	23.95 0.7545 5.79	23.80 0.2035 11.48	24.01 0.2011 11.54

uation procedure based on the reconstruction formula is independent of the definition of edge pixels. Indeed, if one suppose that a reconstructor is able to generate the whole signal from its set \mathcal{K} of edges, using a linear functional \mathcal{G} , then equation (5.51) must be valid, with \mathcal{F}_∞ replaced by \mathcal{K} . Then assuming linearity, translational invariance and isotropy, one gets the following reconstruction formula for testing the validity of the set \mathcal{K} of edge pixels:

$$\widehat{I}(\vec{\omega}) = \frac{\langle \vec{\omega} | \widehat{\nabla I}|_{\mathcal{K}} \rangle}{i \|\vec{\omega}\|^2} \quad (5.62)$$

In that sense, we can say that the reconstruction technique presented in this section is universal.

Table 5.8: Results of reconstruction over different edge detection algorithms. *Image description: Row 1: Harrington weave, Row 2: Hibiscus, Row 3: Car, Row 4: Lena, Row 5: imk01310, Row 6: imk03324, Row 7: imk04050, Row 8: Phase, Row 9: SST.*

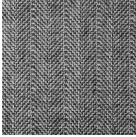
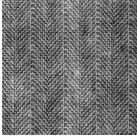
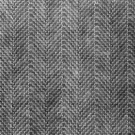
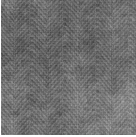
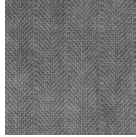
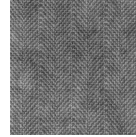
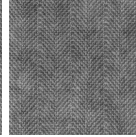



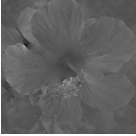

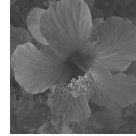
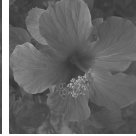
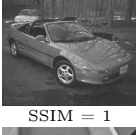
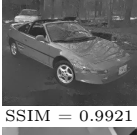


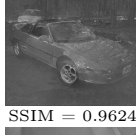
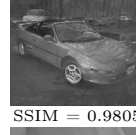
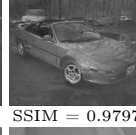

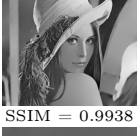

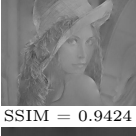
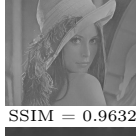
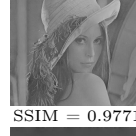

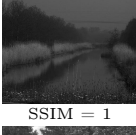


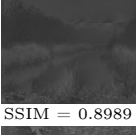
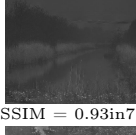


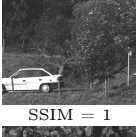
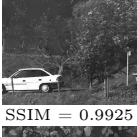
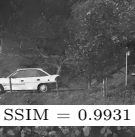
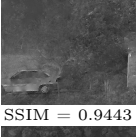
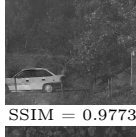
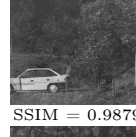
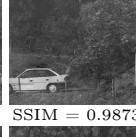
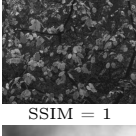
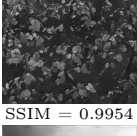
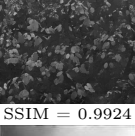
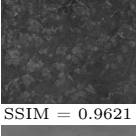
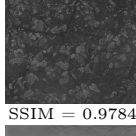
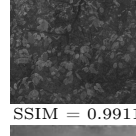
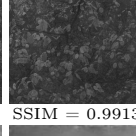
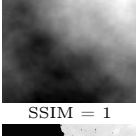



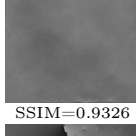

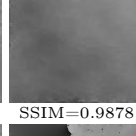
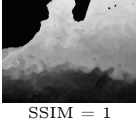


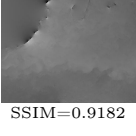
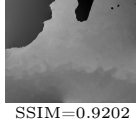


Original	MSM	NLFS	Canny	LoG	Sobel	Prewitt
						
SSIM = 1	SSIM = 0.9881	SSIM = 0.9848	SSIM = 0.9464	SSIM = 0.9839	SSIM = 0.9837	SSIM = 0.9844
						
SSIM = 1	SSIM = 0.9899	SSIM = 0.9886	SSIM = 0.9683	SSIM = 0.9773	SSIM = 0.9862	SSIM = 0.9863
						
SSIM = 1	SSIM = 0.9921	SSIM = 0.9879	SSIM = 0.9347	SSIM = 0.9624	SSIM = 0.9805	SSIM = 0.9797
						
SSIM = 1	SSIM = 0.9938	SSIM = 0.9935	SSIM = 0.9424	SSIM = 0.9632	SSIM = 0.9771	SSIM = 0.9769
						
SSIM = 1	SSIM = 0.9927	SSIM = 0.9903	SSIM = 0.8989	SSIM = 0.93177	SSIM = 0.9823	SSIM = 0.9848
						
SSIM = 1	SSIM = 0.9925	SSIM = 0.9931	SSIM = 0.9443	SSIM = 0.9773	SSIM = 0.9879	SSIM = 0.9873
						
SSIM = 1	SSIM = 0.9954	SSIM = 0.9924	SSIM = 0.9621	SSIM = 0.9784	SSIM = 0.9911	SSIM = 0.9913
						
SSIM = 1	SSIM=0.9986	SSIM=0.9983	SSIM=0.9293	SSIM=0.9326	SSIM=0.9886	SSIM=0.9878
						
SSIM = 1	SSIM=0.9988	SSIM=0.9957	SSIM=0.9182	SSIM=0.9202	SSIM=0.9665	SSIM=0.9881

Table 5.9: Performance under noise: Reconstruction results on different edge detection algorithms under different levels of Gaussian white noise.

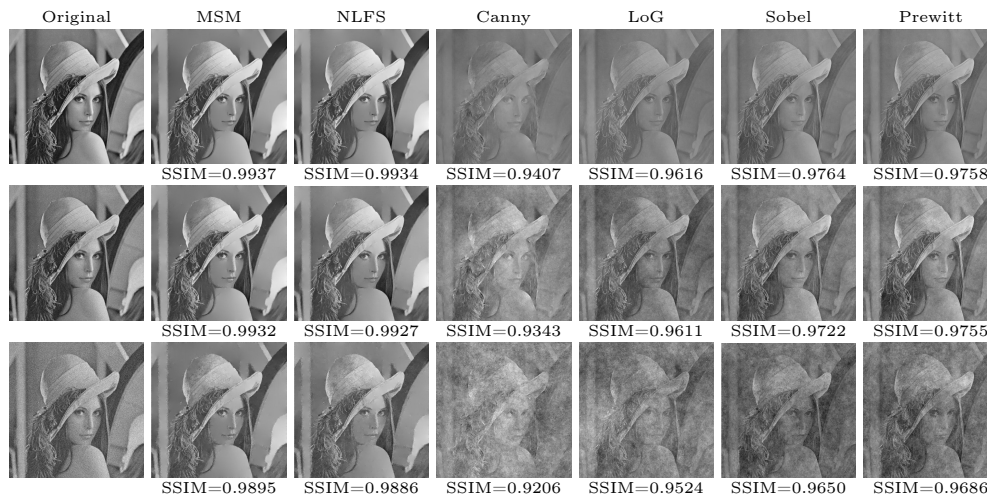


Table 5.10: Quantitative analysis (noisy environment): Evaluation of the reconstruction over different edge detectors. The 1st, 2nd and 3rd row, for every image, represents the performance under input SNR of 26 dB, 14 dB and 6 dB respectively.

Image	MSM	NLFS	Canny	LoG	Sobel	Prewitt
	PSNR , MSE	PSNR , MSE	PSNR , MSE	PSNR , MSE	PSNR , MSE	PSNR , MSE
Weave	16.89 , 0.1763	15.49 , 0.2384	10.37 , 0.7858	14.45 , 0.2964	15.60 , 0.2278	15.51 , 0.2356
	16.68 , 0.2388	15.21 , 0.3301	10.05 , 0.8449	14.24 , 0.4103	15.48 , 0.3344	15.22 , 0.3245
	14.51 , 0.5388	14.61 , 0.6217	9.75 , 1.0993	13.53 , 0.7520	13.98 , 0.6500	13.57 , 0.6169
Hibiscus	22.18 , 0.0954	21.88 , 0.1078	16.01 , 0.4336	17.72 , 0.2755	19.69 , 0.1762	19.66 , 0.1728
	20.64 , 0.1553	20.24 , 0.1708	15.26 , 0.5146	16.93 , 0.3385	18.96 , 0.2590	18.29 , 0.2685
	17.66 , 0.4300	16.07 , 0.4420	13.49 , 0.9930	14.20 , 0.8359	15.53 , 0.6033	16.24 , 0.6487
Car	25.48 , 0.0837	22.87 , 0.1535	15.80 , 0.7351	18.52 , 0.4040	21.22 , 0.2260	20.99 , 0.2364
	23.69 , 0.1416	22.05 , 0.2189	15.72 , 0.7951	18.12 , 0.4612	20.81 , 0.2796	20.02 , 0.3071
	19.41 , 0.3952	17.96 , 0.4794	15.40 , 1.0349	16.61 , 0.7574	18.39 , 0.9708	17.98 , 0.5778
imk01310	29.23 , 0.0627	27.53 , 0.0951	16.82 , 1.1749	17.57 , 0.9494	23.83 , 0.2232	24.46 , 0.1938
	26.21 , 0.1247	25.23 , 0.1595	15.98 , 1.3719	17.45 , 0.9709	22.34 , 0.3155	22.16 , 0.2756
	19.64 , 0.3872	18.75 , 0.4196	13.28 , 1.5785	14.23 , 1.3095	16.67 , 0.6838	17.99 , 0.6100
imk03324	23.07 , 0.0921	21.98 , 0.1216	13.39 , 0.8802	17.34 , 0.3571	20.10 , 0.1932	19.43 , 0.2217
	22.16 , 0.1551	21.80 , 0.1568	13.13 , 0.8853	17.15 , 0.4636	19.52 , 0.2753	19.33 , 0.2911
	18.82 , 0.4310	18.22 , 0.4578	12.10 , 0.9979	16.13 , 0.6700	18.13 , 0.5482	17.40 , 0.5882
imk04050	25.53 , 0.0696	23.95 , 0.1005	17.21 , 0.4712	18.95 , 0.3149	22.49 , 0.1429	22.45 , 0.1422
	23.25 , 0.1317	21.80 , 0.1697	16.46 , 0.5960	18.05 , 0.3875	20.60 , 0.2379	19.74 , 0.2580
	18.06 , 0.4295	17.66 , 0.4450	14.35 , 0.9353	15.36 , 0.7492	16.59 , 0.6069	16.07 , 0.6592
Phase	23.30 , 0.0230	22.77 , 0.0261	7.69 , 0.8889	6.55 , 1.0722	13.07 , 0.2603	12.63 , 0.2604
	19.35 , 0.0884	19.02 , 0.0883	7.17 , 0.9437	6.00 , 1.2843	10.65 , 0.5678	10.97 , 0.5775
	15.39 , 0.3784	15.87 , 0.3693	6.59 , 0.93in51	5.03 , 1.3440	9.80 , 1.1675	9.26 , 0.9469
SST	23.47 , 0.0159	18.02 , 0.0427	5.22 , 0.8383	5.41 , 0.7707	10.11 , 0.3280	10.74 , 0.2852
	19.21 , 0.0822	17.85 , 0.0979	5.09 , 0.9554	4.96 , 0.8102	9.74 , 0.4179	10.53 , 0.3253
	15.09 , 0.3686	15.03 , 0.3797	4.86 , 1.3826	4.14 , 0.9676	9.00 , 0.7962	9.76 , 0.7958

Experiment 2

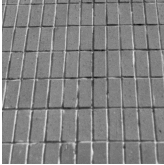
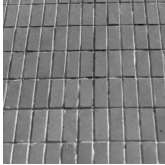
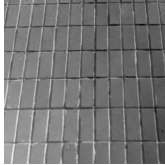
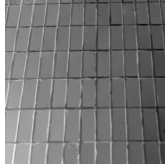
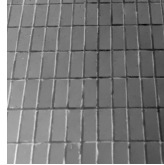
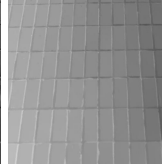

















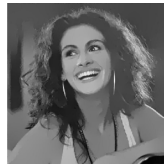




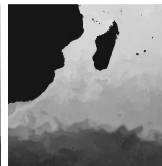
We take the edge representation of different natural images given by their MSM points and reconstruct from them an approximation of the original image, using equation (5.58). We compare our reconstruction with the results of the reconstruction, over the MSM points, obtained from standard reconstruction techniques discussed in subsection 5.3.1.2. The pixel density of the edges, for the experimental images, are kept the same (30%) while performing reconstruction. The results are shown in Table 5.11. Table 5.12 shows the performance evaluation of the reconstructed images using PSNR and MSE metrics and Table 5.13 shows the performance of the reconstruction under different levels of input SNR using the same metrics.

Discussion

Visual quality of the reconstruction in Table 5.11, evaluated using SSIM, shows that R_{msm} outperforms the classical reconstruction algorithms in majority of the cases. Quantitative analysis of the results, shown in Table 5.12 (without noise) and Table 5.13 (with noise) also shows the superiority of R_{msm} over other reconstruction algorithms.

The ability to reconstruct an image from its edge representation lies in the efficiency of the edge detection algorithm as well as in the ability of the reconstruction algorithm to estimate an accurate approximation of the original image from the information coded in its edges. The efficiency of an edge detector lies not only in extracting features of real information from an image, but at the same time discarding redundant or perceptually irrelevant information. The R_{msm} permits a quantitative evaluation of the compactness

Table 5.11: Performance of different reconstruction algorithms. Row 1: Brick wall Row 2: House Row 3: *imk03322* Row 4: Aerial view of a truck Row 5: *Julia Roberts* Row 6: *SST* image.

Original	R _m sm	Poisson solver	Regularization	M-estimators	Diffusion
					
SSIM = 1	SSIM = 0.9922	SSIM = 0.9509	SSIM = 0.9182	SSIM = 0.9403	SSIM = 0.8895
					
SSIM = 1	SSIM = 0.9987	SSIM = 0.9954	SSIM = 0.9922	SSIM = 0.9951	SSIM = 0.9945
					
SSIM = 1	SSIM = 0.9986	SSIM = 0.9972	SSIM = 0.9964	SSIM = 0.9966	SSIM = 0.9962
					
SSIM = 1	SSIM = 0.9813	SSIM = 0.9519	SSIM = 0.9456	SSIM = 0.9530	SSIM = 0.9536
					
SSIM = 1	SSIM = 0.9901	SSIM = 0.9809	SSIM = 0.9707	SSIM = 0.9742	SSIM = 0.9783
					
SSIM = 1	SSIM = 0.9991	SSIM = 0.9989	SSIM = 0.9909	SSIM = 0.9990	SSIM = 0.9989

of a representation, leading to highly accurate approximation of an original image from its edge pixels.

Table 5.12: Quantitative analysis: *Evaluation of the reconstruction algorithms, corresponding to Table 5.11, in terms of PSNR (in dB) and MSE.*

Image		Rmsm	Poisson solver	Regularization	M-estimators	Diffusion
Brick wall	PSNR	24.33	16.84	14.39	15.98	12.67
	MSE	0.0909	0.5102	0.8975	0.6204	1.3284
House	PSNR	24.90	20.77	19.09	20.48	20.62
	MSE	0.0183	0.0478	0.0733	0.0543	0.0493
imk03322	PSNR	30.63	27.72	26.75	27.05	26.75
	MSE	0.0170	0.0329	0.0409	0.0382	0.0415
Aerial	PSNR	21.01	17.06	16.41	17.25	17.19
	MSE	0.2209	0.4948	0.5682	0.4780	0.4661
Julia	PSNR	18.31	15.47	13.64	14.33	14.79
	MSE	0.0934	0.1805	0.2758	0.2364	0.2068
SST	PSNR	25.10	24.82	16.25	24.61	24.58
	MSE	0.0088	0.0110	0.0820	0.0114	0.0121

Table 5.13: Quantitative analysis for noisy environment: *Evaluation of the reconstruction algorithms, in terms of PSNR and MSE, under different levels of noise.*

Image	Algorithm	SNR = 40 dB MSE, PSNR	SNR = 20 dB MSE, PSNR	SNR = 14 dB MSE, PSNR	SNR = 6 dB MSE, PSNR
Brick wall	R _{rmsm}	0.0912, 24.26	0.0952, 23.98	0.1180, 23.28	0.2357, 21.46
	Poisson solver	0.5119, 16.79	0.5187, 16.69	0.5264, 16.54	0.5952, 16.27
	Regularization	0.8978, 14.31	0.8992, 14.18	0.9556, 13.22	0.9891, 12.84
	M-estimator	0.6213, 15.92	0.6343, 15.76	0.6408, 15.70	0.8261, 14.91
	Diffusion	1.3296, 12.64	1.3342, 12.59	1.4321, 12.48	1.4565, 12.35
House	R _{rmsm}	0.0183, 24.88	0.0269, 23.37	0.0475, 21.33	0.1723, 18.16
	Poisson solver	0.0472, 21.20	0.0607, 19.88	0.0805, 19.41	0.2057, 16.87
	Regularization	0.0745, 18.91	0.0775, 18.88	0.0889, 18.26	0.2057, 16.92
	M-estimator	0.0548, 20.32	0.0629, 19.68	0.0820, 19.50	0.2009, 17.68
	Diffusion	0.0497, 20.40	0.0590, 20.15	0.1106, 18.34	0.4236, 14.34
imk03322	R _{rmsm}	0.0171, 30.59	0.0248, 28.69	0.0478, 25.60	0.1780, 20.93
	Poisson solver	0.0331, 27.67	0.0425, 26.40	0.0687, 23.65	0.2023, 18.76
	Regularization	0.0411, 26.72	0.0452, 26.32	0.0674, 24.14	0.1918, 19.12
	M-estimator	0.0386, 26.98	0.0449, 26.28	0.0638, 24.74	0.1972, 17.57
	Diffusion	0.0419, 26.63	0.0557, 25.47	0.0871, 23.18	0.3066, 15.93
Aerial	R _{rmsm}	0.2210, 21.00	0.2311, 20.67	0.2577, 20.02	0.3862, 18.87
	Poisson solver	0.4960, 17.03	0.4966, 16.61	0.5029, 16.52	0.6099, 14.71
	Regularization	0.5684, 16.39	0.6011, 16.11	0.6607, 16.06	0.7021, 14.63
	M-estimator	0.4783, 17.03	0.4854, 16.84	0.4993, 16.38	0.5889, 15.77
	Diffusion	0.4669, 17.08	0.5046, 16.79	0.6174, 15.66	0.8075, 14.00
Julia	R _{rmsm}	0.0936, 18.18	0.1343, 17.93	0.1699, 17.10	0.2412, 16.34
	Poisson solver	0.1776, 15.37	0.2098, 15.11	0.2393, 14.98	0.4882, 13.76
	Regularization	0.2736, 13.54	0.2812, 13.11	0.3119, 12.43	0.3908, 11.94
	M-estimator	0.2367, 14.26	0.2619, 13.99	0.3323, 13.98	0.4940, 13.51
	Diffusion	0.2256, 14.38	0.3718, 13.54	0.3864, 12.92	0.7331, 12.65
SST	R _{rmsm}	0.0091, 25.08	0.0169, 23.23	0.0384, 21.42	0.1699, 17.54
	Poisson solver	0.0112, 24.68	0.0182, 23.26	0.0386, 20.68	0.1874, 17.61
	Regularization	0.0853, 16.09	0.0889, 15.30	0.1756, 14.05	0.1820, 12.39
	M-estimator	0.0115, 24.55	0.0182, 23.14	0.0499, 20.13	0.1701, 17.40
	Diffusion	0.0118, 24.49	0.0216, 22.38	0.0489, 20.37	0.3598, 14.21

Experiment 3

In this experiment, we compare the performance of different reconstruction algorithms over different edge detection techniques and in the process check the best possible combination (edge detector + reconstructor) that gives the best results in terms of reconstruction. We choose R_{msm} and other reconstructors, already discussed in this chapter, for reconstructing test images from their edge pixels (obtained from different edge detection techniques). The pixel density of the edges, calculated using different edge detectors, are kept within a close range (between 25 – 35%), with the pixel density of MSM points kept minimum. The classical edge algorithms tested are Matlab[®] implementations. Results are shown in table 5.14 and table 5.15.

Discussion

















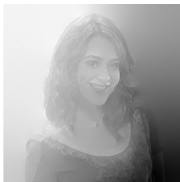













We have presented a quantitative analysis on the performance of different reconstruction algorithms over different edge detectors and have compared all possible combinations of them to verify the best performing duo (edge detector + reconstructor). It happens that, in majority of the cases, the combination of MSM and R_{msm} gives the best possible results. Infact, in table 5.14 we can see that the combination of the reconstructors with MSM gives the best results (data underlined) compared to any other edge detector. For certain edge detectors, the combination with Poisson solver gives better results: for example, Hibiscus (with Sobel edge detector) and Boat

Table 5.14: Quantitative analysis of the performance of different reconstruction algorithms over different edge detectors: *Data marked in blue indicates the reconstructor that performs the best, over other reconstruction techniques, for a particular edge detection algorithm. Data underlined indicates the edge detection algorithm that gives the best result, in terms of reconstruction, over all the other edge detectors, for a particular reconstructor.*

Image	Algorithm	R _{msm}	Poisson solver	Regularization	M-estimator	Diffusion
		MSE, PSNR	MSE, PSNR	MSE, PSNR	MSE, PSNR	MSE, PSNR
Hibiscus	MSM	<u>0.0906, 22.08</u>	<u>0.1042, 21.96</u>	<u>0.1530, 20.37</u>	<u>0.1163, 21.42</u>	<u>0.1168, 21.43</u>
	NLFS	0.0944, 21.92	1.4791, 10.41	1.3846, 10.75	1.2795, 11.12	1.4393, 10.46
	Canny	0.4005, 16.04	0.4889, 15.38	0.6270, 14.20	0.7614, 13.42	1.0162, 12.08
	LoG	0.2657, 17.76	1.6979, 9.83	1.6545, 10.08	1.5900, 10.09	1.7405, 9.76
	Sobel	0.1690, 17.72	0.1571, 20.19	0.2285, 18.56	0.1826, 19.52	0.5453, 14.79
	Prewitt	0.1622, 19.80	0.1443, 20.49	0.2270, 18.45	0.1795, 19.61	0.5062, 15.13
Car	MSM	<u>0.0794, 25.59</u>	<u>0.1033, 24.45</u>	<u>0.1617, 22.50</u>	<u>0.1242, 23.65</u>	<u>0.1095, 24.19</u>
	NLFS	0.1321, 23.37	0.2330, 20.91	0.2547, 20.52	0.2931, 19.92	0.4530, 18.03
	Canny	0.7350, 15.84	1.0848, 14.14	1.1642, 13.83	1.2375, 13.57	1.1917, 13.73
	LoG	0.4038, 18.53	1.5238, 12.75	1.5087, 12.80	1.4763, 12.89	1.5260, 12.76
	Sobel	0.2150, 21.26	0.7679, 15.73	0.8179, 15.46	0.4536, 18.02	0.6453, 16.49
	Prewitt	0.2262, 21.04	0.9510, 14.80	0.9629, 14.75	0.5347, 17.30	0.7295, 15.95
Boat	MSM	<u>0.0969, 18.71</u>	<u>0.1567, 16.62</u>	<u>0.1617, 22.50</u>	<u>0.1466, 16.91</u>	<u>0.1970, 15.63</u>
	NLFS	0.0997, 18.58	0.2271, 15.01	0.2547, 20.52	0.4923, 11.65	0.4648, 11.90
	Canny	0.9636, 8.72	0.7153, 10.01	1.1642, 13.83	0.9272, 8.88	0.93in67, 8.98
	LoG	0.4145, 12.40	1.2415, 7.64	1.5087, 12.80	1.2606, 7.57	1.3018, 7.43
	Sobel	0.3296, 13.39	0.7788, 9.66	0.8179, 15.46	0.8205, 9.44	0.4706, 11.85
	Prewitt	0.3708, 12.88	0.7365, 9.90	0.9629, 14.75	0.7814, 9.65	0.5439, 11.22
Camille	MSM	<u>0.0521, 15.60</u>	<u>0.0743, 14.06</u>	<u>0.0852, 13.47</u>	<u>0.0723, 14.18</u>	<u>0.0910, 13.18</u>
	NLFS	0.0529, 15.53	0.0792, 13.78	0.1412, 11.28	0.0834, 13.56	0.3865, 6.90
	Canny	0.3550, 7.26	0.3927, 6.82	0.4094, 6.64	0.4665, 6.07	0.5704, 5.19
	LoG	0.2639, 8.56	0.8539, 5.09	0.8301, 5.15	0.7235, 5.41	0.8237, 5.16
	Sobel	0.1114, 12.19	0.1808, 10.20	0.1771, 10.29	0.1432, 11.21	0.3831, 6.94
	Prewitt	0.1133, 12.23	0.2888, 8.16	0.2388, 9.09	0.1541, 10.89	0.4681, 6.07
imk03324	MSM	<u>0.0854, 23.08</u>	<u>0.1456, 20.76</u>	<u>0.1848, 19.72</u>	<u>0.2604, 18.24</u>	<u>0.5899, 14.69</u>
	NLFS	0.0960, 22.57	0.1887, 19.63	0.2285, 18.80	0.3536, 17.35	1.1471, 11.79
	Canny	0.7808, 13.42	1.4146, 10.85	1.4535, 10.72	1.4446, 10.75	1.5041, 10.58
	LoG	0.3168, 17.38	2.3025, 8.77	2.3019, 8.79	2.3256, 8.73	1.4650, 10.73
	Sobel	0.1634, 20.26	1.3966, 10.94	1.4782, 10.69	1.4603, 10.75	1.5532, 10.48
	Prewitt	0.1705, 20.07	1.4172, 10.88	1.4859, 10.67	1.4926, 10.65	1.4189, 10.87

(with Canny edge detector). However, they are always outperformed by the combination of MSM and R_{msm}.

Table 5.15: Performance of different reconstructors over different edge detectors. Each row indicates the performance of the reconstructors for a given edge detection algorithm. Every column shows the edge detection algorithm that gives the best result, in terms of reconstruction, for a particular reconstructor.

	R _m sm	Poisson solver	Regularization	M-estimator	Diffusion
MSM Density = 25.00%	 SSIM = 0.9942	 SSIM = 0.9935	 SSIM = 0.9904	 SSIM = 0.9936	 SSIM = 0.9908
NLFS [107] Density = 25.14%	 SSIM = 0.9938	 SSIM = 0.9915	 SSIM = 0.9863	 SSIM = 0.9921	 SSIM = 0.9577
Canny Density = 28.29%	 SSIM = 0.9638	 SSIM = 0.9578	 SSIM = 0.9567	 SSIM = 0.9526	 SSIM = 0.9445
LoG Density = 31.26%	 SSIM = 0.9750	 SSIM = 0.8121	 SSIM = 0.8134	 SSIM = 0.8182	 SSIM = 0.8093
Sobel Density = 25.31%	 SSIM = 0.9895	 SSIM = 0.9808	 SSIM = 0.9819	 SSIM = 0.9871	 SSIM = 0.9633
Prewitt Density = 25.29%	 SSIM = 0.9896	 SSIM = 0.9681	 SSIM = 0.9753	 SSIM = 0.9859	 SSIM = 0.9545

§ 5.4 CONCLUSION

In this chapter, we have discussed about the ability of the singularity exponents in capturing the important multiscale features of a signal. We have justified this claim, experimentally, by a two step procedure. In the first step, we have proved that edges obtained from singularity exponents better represent the transitions within a turbulent signal and are much more consistent across the scales of the signal. In the second step, we show that better reconstruction of the signal is achieved from the edges obtained through singularity analysis of the signal. Indeed, if edges encode the most important features of a signal, it should also be possible to reconstruct the signal from its edge representation. This argument is well justified in section 5.3.

Armed with the results of section 5.2 and section 5.3, and with an approximative version of the optimal wavelet for a turbulent phase signal, we move on to the next chapter of this thesis where we implement the idea of multiresolution analysis on the signal of the singularity exponents, for wavefront phase reconstruction in AO.

- CHAPTER 6 -

A MULTISCALE APPROACH TO PHASE RECONSTRUCTION FOR AO

Turbulence in the different layers of the Earth's atmosphere plays a fundamental role in limiting the resolution of ground-based instruments. These turbulent layers perturbate to a great extent incoming light from outer space, resulting in a phase distortion of the incoming planar wavefronts. AO is one of the best known method to overcome this hurdle [66, 67, 68, 137, 164]. In most AO systems, the perturbed phase is acquired through a specific WFS (wavefront sensor), in the form of slope measurement (or curvature measurement) of the wavefront phase. The WFS measures the distortions in the wavefront, which is then passed through a servo-loop to the DM (deformable mirror) which approximates its shape according to the shape of the wavefront, to reduce the wavefront phase residual error. One of the most commonly used wavefront sensor is the SH (Shack-Hartmann) sensor, which measures the local slope (gradients) of the wavefront. The reconstruction of the wavefront from the slope measurements of a SH sensor is generally seen as an inverse problem and can be expressed in a matrix-algebra framework [137, 164]. The commonly used techniques for estimating the phase are [98, 164]:

- the ML (maximum likelihood) technique, and
- the MAP (maximum *a posteriori*) technique.

The ML method yields to the generalized *least squares solution* [110, 164] which is the solution classically used for estimating the phase under real-time constraints.

In the case of long time exposures, the optical transfer function of the imaging instrument is multiplied by an atmospheric transfer function which is expressed using classical correlation functions and related to the Kolmogorov model of turbulence [164]. This suggests that an acquired image behaves like a complex signal having multiscale properties [180]. Consequently, recent advances in the framework of reconstructible systems for complex signals are likely to apply to the case of an acquired perturbed optical phase, and, in particular, other reconstruction techniques of the perturbed phase, based on the cascading properties of fully developed turbulence can be taken into consideration [203, 21]. The general organization of a multiscale structure in complex signals has been related to the existence of cascade processes. The MMF thereby proves to be a suitable approach for the study of multiscale properties in real signals which generalize previous approaches [202].

This chapter focusses on the use of the MMF scheme for wavefront phase reconstruction from the low-resolution slope measurement (gradients) of the perturbed phase. We also check the reconstruction performance after adding different proportions of Gaussian white noise to the gradients. Instead of using the conventional method of least squares estimation (or deconvolution [70, 138, 60, 168, 169] for image restoration), we try to obtain the phase from its low-resolution gradients by propagating the information of a turbulent phase along the scales, from low-resolution to high-resolution, using the multiresolution analysis and specific wavelet projections [126, 127, 157, 217]. We have shown, in the previous chapter, that the singularity exponents encode important multiscale features of the signal (well noticed in the MSM). We do a multiresolution analysis on the complete set of singularity exponents computed on a turbulent phase map (and not just the MSM), to infer information along the scales and then reconstruct with this information. This work, for the case of wavefront phase reconstruction, is new in comparison to classical reconstruction techniques in AO. Wavelets are used widely in astronomical imaging, now with the development of *X*-lets (i.e. curvelets etc.) [28, 27, 29, 30, 174, 188].

The chapter is organized as follows: In section 6.1, we describe the dataset we have used for our experimental work. In section 6.2 we explain our wavefront phase estimation algorithm. Results are shown in section 6.3. In section 6.4, we compare our algorithm with the classical least squares technique. Finally, we conclude in section 6.6.

§ 6.1 DESCRIPTION OF DATA

The datasets used in our work are of simulated turbulent optical phase provided by the French Aerospace Lab-ONERA. We have 1000 occurrences (slices) of turbulent phase and their associated PSF for our experimental purpose, with the following imaging characteristics:

- diameter of the telescope: 8 m,
- seeing at 5 microns: 0.85 arcseconds,
- Fried parameter r_0 at imaging wavelengths: 70 cm,
- wind speed: 12.5 m/s,
- acquisition frequency: 250 Hz.

The pupil is defined on 256×256 pixels. Data is generated in the FITS format [2]. For the statistical purpose of our experiment we need a set of appropriate sub-images. These sub-images must be as large as possible (for statistical confidence) and clean (without missing pixels). In addition, due to the requirements imposed by our wavelet analysis, we also require these sub-images to be square sampled with the sampling size being a power of 2. To avoid sub-reconstruction and Gibbs phenomena coming from the strong transition associated to the pupil's boundary, we take a sub-image made of 128×128 pixels centered in the middle of the pupil of the original phase data. An example of the experimental phase and its associated PSF is shown in Fig 6.1.

The low-resolution x and y components of the phase gradient are calculated as follows : From the given phase data, we compute the gradients of the phase and produce an averaged gradient over a window of size 8×8 pixels, normalized by the size of the window (64 square pixels) thus resulting

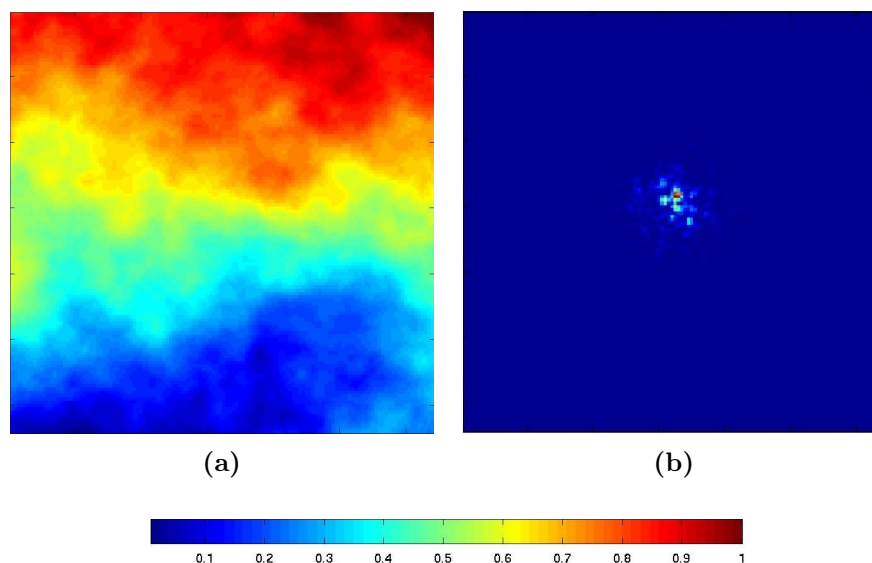


Figure 6.1: (a) Image of a simulated phase perturbed by atmospheric turbulence (see section 6.1 for imaging characteristics). The image corresponds to a 128×128 pixels sub-image extracted from an original 256×256 pixels image to avoid the pupil's boundary. (b) Point spread function (PSF) image associated to the image of the perturbed phase.

in a 16×16 sub-image corresponding to the x and y slope measurement of an SH WFS. For our experimental purpose, we have generated gradients of size 32×32 pixels and 64×64 pixels by the same procedure, normalized by their respective window size (i.e. 4×4 pixels and 2×2 pixels respectively).

§ 6.2 RECONSTRUCTION TECHNIQUE

From the results and discussions presented in chapter 5, we have shown that even if we are not able to compute directly an optimal wavelet, we can rely on the results which proves that the singularity exponents are candidates that carry the multiscale information of a turbulent signal. We can therefore replace a “real” optimal wavelet and its associated multiresolution analysis by a classical multiresolution analysis but performed on the signal of the

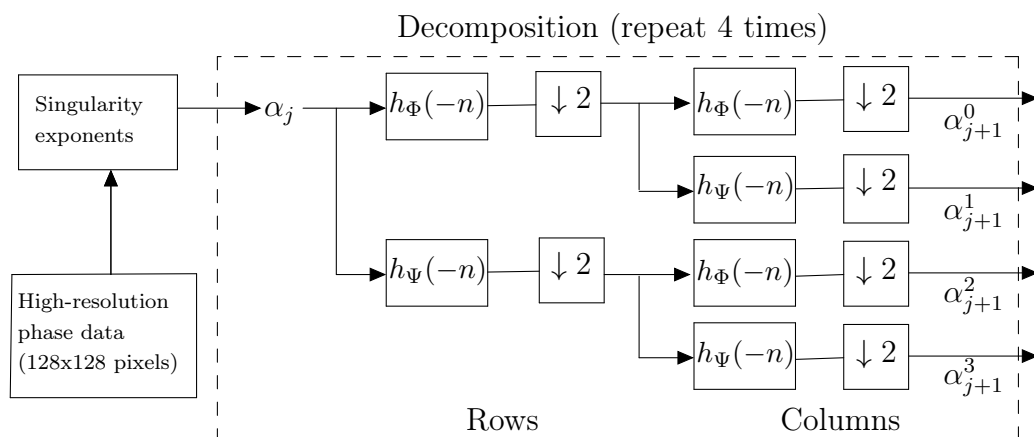


Figure 6.2: Representation of the analysis process. We take as input a high-resolution 128×128 pixels phase screen. We then compute the singularity exponents of this high-resolution phase screen and do a multiresolution analysis (MRA) over the exponents. The high-resolution phase screen can be the true phase itself, an average instance of the true phase over time or any random phase screen with Kolmogorov turbulence statistics. Here, α_j is the approximation of the initial image (i.e. the image of the singularity exponents) at the resolution j . Level 1 MRA results in a coarser approximation of α_j i.e. α_{j+1}^0 (size: 64×64 pixels) and the details α_{j+1}^1 , α_{j+1}^2 and α_{j+1}^3 . The process is repeated four times to get an approximation of size 16×16 pixels.

singularity exponents. This is why we have a two step reconstruction process: analysis consists in computing a multiresolution analysis on the signal of singularity exponents, with a third order Battle Lemarié (B-L) wavelet, and extract the details. Synthesis consists in using this details to obtain gradients at higher resolution, from which the phase is estimated.

We therefore formulate the process of reconstructing the phase from its gradient measurement accordingly. In the analysis part of the algorithm, we try to extract the wavelet coefficients from the signal of the singularity exponents (denoted by $s_h(n_1, n_2)$ of size $N_1 \times N_2$ computed on the phase

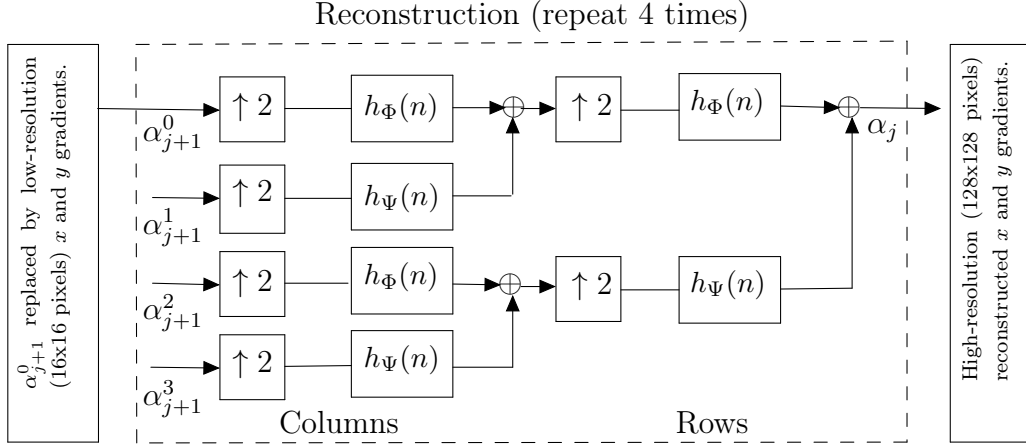


Figure 6.3: Representation of the synthesis process. Here the low-resolution 16×16 pixels approximation obtained from the analysis part are replaced with the low-resolution 16×16 pixels gradient of the phase. Then with the knowledge of the details at every level, the signal is reconstructed from 16×16 pixels to 32×32 pixels, then to 64×64 pixels (α_{j+1}^0) and finally to 128×128 pixels i.e. α_j . The process is repeated for both x and y gradients to obtain a high-resolution estimate of the phase gradients at 128×128 pixels.

data) by a multiresolution analysis with an approximate optimal wavelet Ψ (here B-L wavelet), following the equation:

$$\alpha_{j,k_1,k_2}^i = \frac{1}{\sqrt{N_1} \times \sqrt{N_2}} \sum_{n_1=0}^{N_1-1} \sum_{n_2=0}^{N_2-1} \Psi_{j,k_1,k_2}^i(n_1, n_2) s_h(n_1, n_2) \quad (6.1)$$

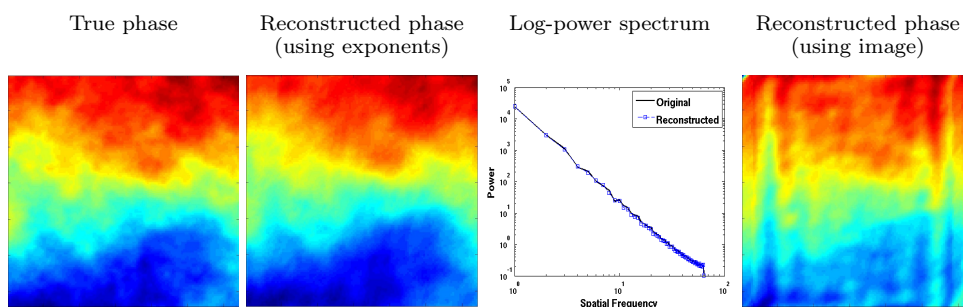
for all orientations i , scale j and positions k_1, k_2 (see section 5.1.1.3 for details). Then with the knowledge of the wavelet coefficients at the intermediate scales, we try to reconstruct the signal (high-resolution gradients in this case) by:

$$s(n_1, n_2) = \sum_{i=0,1,2,3} \sum_j \sum_{k_1,k_2} \alpha_{j,k_1,k_2}^i \Psi_{j,k_1,k_2}^i(n_1, n_2) \quad (6.2)$$

This is the second step of the approach and is known as the synthesis part of the algorithm. The process of reconstruction can be summarized accordingly:

- We first compute the third order B-L wavelet coefficients associated to the signal of the singularity exponents computed on the perturbed phase signal. Considering a given phase map as an approximation image at scale j , we compute the singularity exponents of this phase map using equation (5.40). We then consider the image corresponding to the singularity exponents (we consider all the exponents over the phase map without any thresholding) as the input image to the multiresolution analysis.
- A multiresolution analysis on the input image (i.e., the image of the singularity exponents) gives rise to an approximation image (α_{j+1}^0) and the details i.e. the wavelet coefficients (α_{j+1}^1 , α_{j+1}^2 and α_{j+1}^3 are the horizontal, vertical and diagonal details respectively) for the next coarser scale $j + 1$.
- Every level gives rise to an image fourth smaller than the previous one. We repeat the operation 4 times to an approximation of size 16×16 pixels. We store the details of the exponents obtained in the intermediate levels.
- This part of the operation is called the analysis part (decomposition), and is explained in Fig 6.2.
- The next part of the operation is called the synthesis part (reconstruction), and is shown in Fig 6.3.
- We replace the resultant approximation image (a coarser approximation of the singularity exponents, obtained from the analysis operation) with the low-resolution x and y gradient measurements (16×16 pixels sub-image, see section 6.1) of the phase data.
- For each component (x and y) of the phase gradient at low-resolution, we back project the component (using equation (6.2)) to high-resolution using the intermediate detail coefficients (i.e. details of the singularity exponents obtained from the analysis operation), to get a phase's gradient at higher spatial resolution of 128×128 pixels.

Table 6.1: Left to right : *True phase, reconstruction of the phase using signal of the singularity exponents as input to the multiresolution decomposition, comparison of the PSD between the true phase and the reconstructed phase, reconstruction of the phase using the true phase as input to the multiresolution decomposition.*



- The estimation of the phase from its high-resolution gradients is obtained by solving the discrete Poisson equation with Neumann boundary conditions. We use a fast Poisson solver for this purpose (see section 5.3.1.2).

§ 6.3 RESULTS

Results obtained show visual resemblance of the reconstructed signal with the original one. Performance of reconstruction using the singularity exponents and the image, as input to the analysis part of the algorithm, is shown in table 6.1. The results clearly shows the necessity of using the signal of the singularity exponents in the decomposition process. We also check the performance of our reconstruction technique after adding different proportions of Gaussian white noise to the gradients, results are shown in table 6.2. Quantitative analysis is presented in table 6.3. We also compute the PSF and the modulus of the OTF for the reconstructed phase, and compare them with that of the true phase. The results are shown in table 6.4 and table 6.5.

Table 6.2: Results of the reconstruction in a noisy environment. **Top row** : Reconstructed phase under different levels of SNR. **Bottom row** : Comparison of the PSD between the true phase and the reconstructed phase under different levels of SNR.

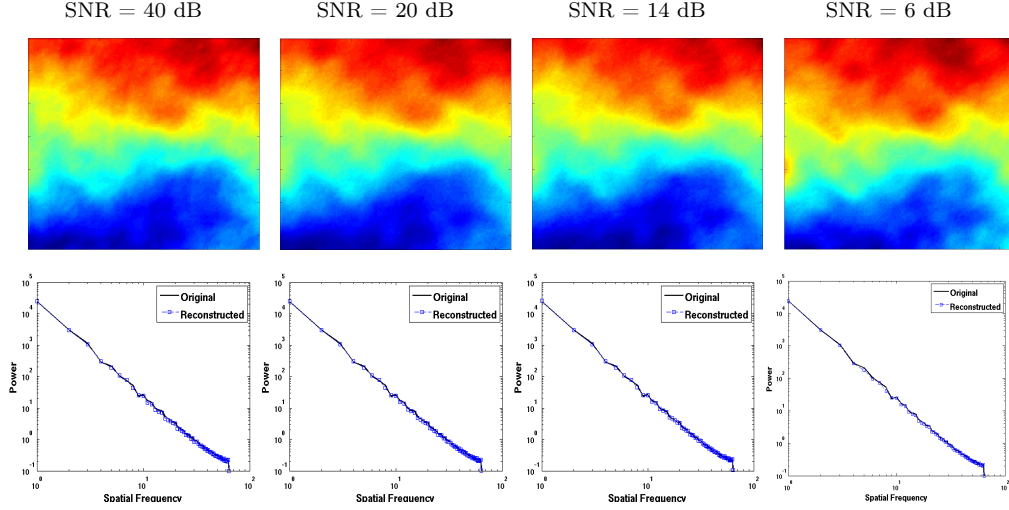


Table 6.3: Evaluation of the phase reconstruction of table 6.2 in terms of MSE and PSNR metrics.

Params	No noise	40 dB	20 dB	14 dB	6 dB
MSE	0.1978	0.2216	0.2253	0.2406	0.3125
PSNR (dB)	31.18	30.68	30.16	29.32	28.19

§ 6.4 RESIDUAL PHASE STATISTICS

As discussed in section 3.1.1, chapter 3, the principle of AO correction is to reduce the residual error in the equation:

$$\Delta\phi(r, \theta) = \phi_{turb}(r, \theta) - \phi_{cor}(r, \theta) \quad (6.3)$$

where $\Delta\phi(r, \theta)$ is the residual phase (tends to zero with the AO correction) and $\phi_{cor}(r, \theta)$ corresponds to the phase obtained by the mirror deformation

Table 6.4: Performance under noise - Point spread function (PSF). The X cut and Y cut of the PSF are displayed. The y-axis corresponds to the square of the normalized image plane irradiance and the x-axis corresponds to the angular distance in arcseconds.

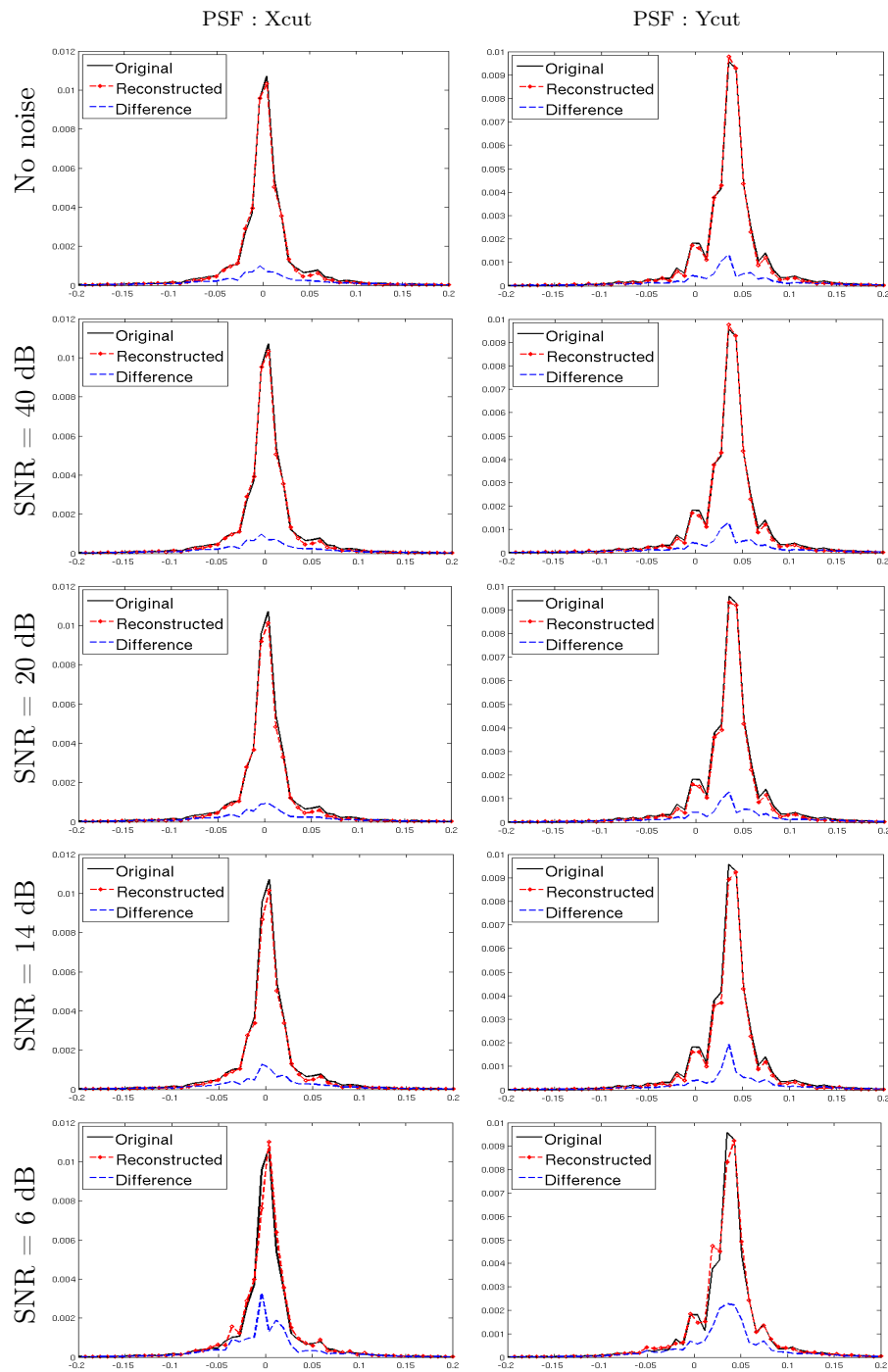
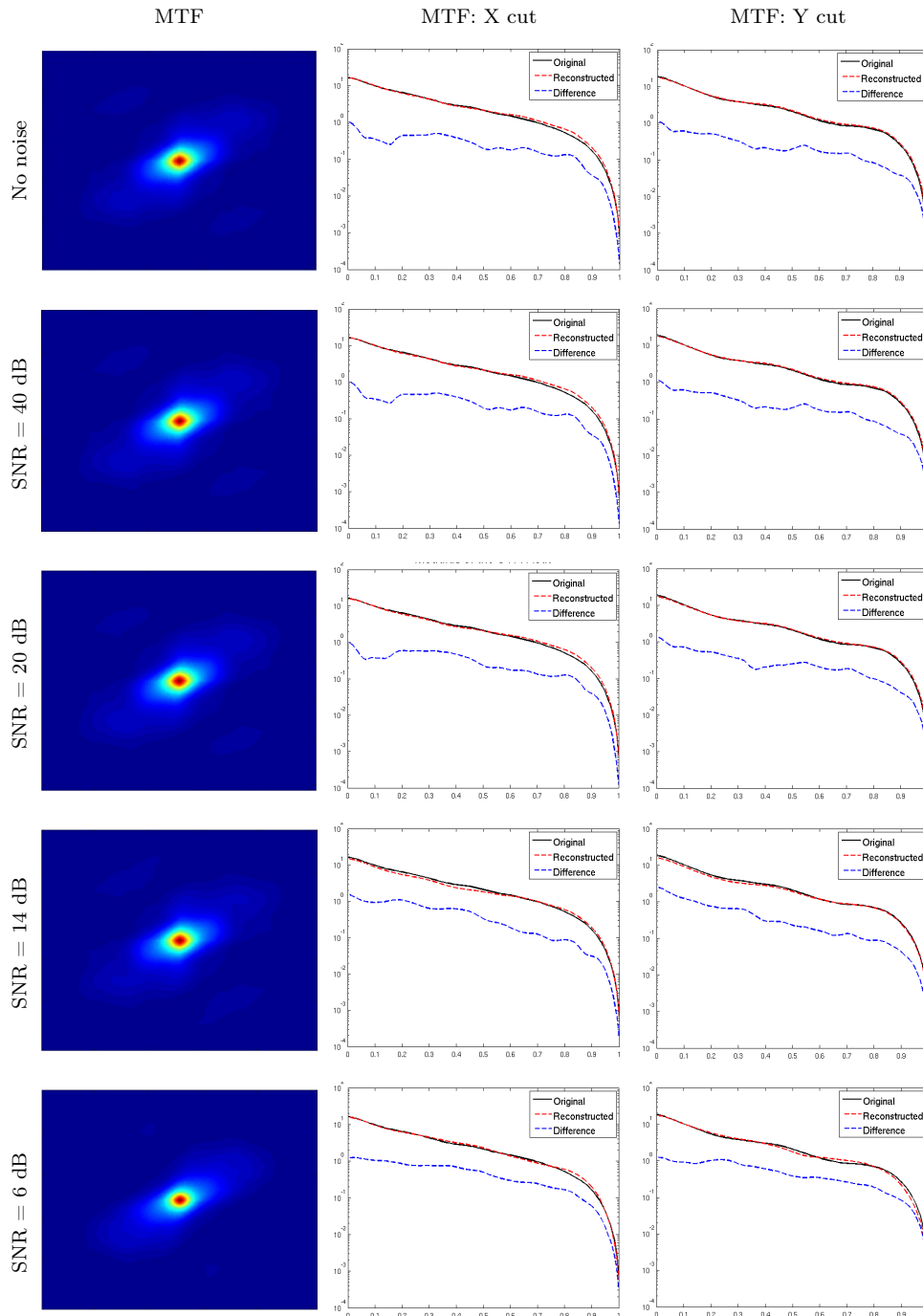


Table 6.5: Performance under noise - Modulus of OTF (MTF). *The X cut and Y cut of the MTF are displayed with a logarithmic scale. The y-axis corresponds to the logarithm of the MTF and the x-axis represents the normalized frequency in D/λ units.*



(correction by AO). We set up an experiment, in which we compare the PSD of $\Delta\phi$ when ϕ_{cor} is obtained using our technique and the classical least squares reconstruction technique (see section 3.2.4.3), which is the general solution to the inverse problem solution methods [110]. Multigrid solvers and precondition conjugate gradient solvers [75, 74, 18] are the most computationally efficient approaches in this regard. For comparing the reconstruction quality using our method and the least squares approach, we set-up the following experiment:

- We generate the estimated phase ϕ_{cor} with our method (derived from the framework of MMF) using the singularity exponents, computed on three different high-resolution phase screen, as input to the decomposition part of our algorithm (see section 6.2 and Fig 6.2).
- The three different high-resolution phase screens are: (a) the true phase, (b) an average phase obtained from the 10 previous and 10 post instances of the true phase and (c) a fixed FFT based phase screen obtained by McGlammery method [134] (see section 2.5.2) using the Kolmogorov power spectrum.
- For calculating the average phase instance of (b), we consider a total of 960 phase instances from the original 1000 instances (start with the 21st phase screen and end on the 980th phase screen).
- Given the estimated phase (ϕ_{cor}) and true phase (ϕ_{turb}), we calculate the residual phase $\Delta\phi$ by equation (6.3).
- We calculate the residual phase for all 960 instances of the phase ($N = 960$), using our technique (for all the three different high-resolution inputs) and the least squares technique.
- ϕ_{cor} is of size 128×128 pixels. Reconstruction is repeated for three different size of the gradients: 64×64 pixels, 32×32 pixels and 16×16 pixels.
- The least squares reconstructed phases are oversampled to 128×128 pixels resolution from their respective gradient resolution using bicubic interpolation.

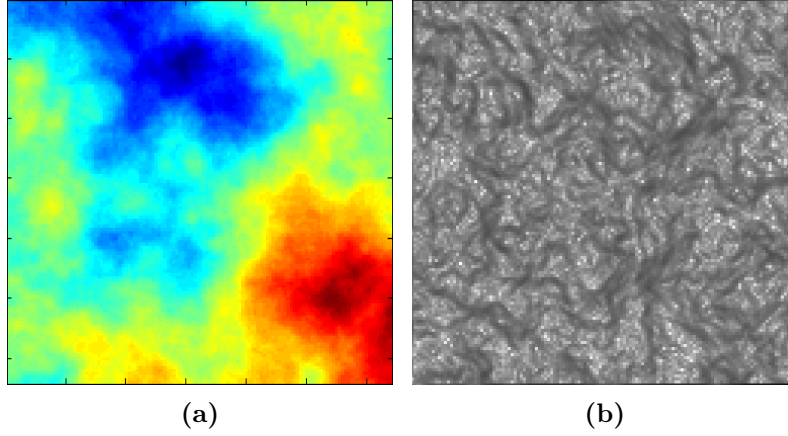


Figure 6.4: (a) Image of a simulated turbulent phase screen generated by the FFT based method [134] using a Kolmogorov power spectrum. (b) Singularity exponents computed on the phase data.

- The average residual phase PSD, for all the 960 instances are then calculated, as $\frac{1}{N} \sum_{i=1}^N |\mathcal{F}(\Delta\phi)|^2$, where \mathcal{F} is the Fourier transform.
- We then plot the PSD against spatial frequency, for our technique and least squares technique, and compare.

In table 6.6, we show the results of the residual phase PSD, with the true phase as input high-resolution phase for our algorithm. Table 6.7 and Table 6.8 shows the same results like table 6.6, but using an average phase instance and a Kolmogorov phase screen (shown in Fig 6.4), respectively, (instead of the true phase) as input high-resolution phase for our algorithm.

§ 6.5 RESULTS AND DISCUSSION

We have shown the quality of our reconstruction algorithm, in comparison to least squares technique (commonly used in AO for phase estimation) in section 6.4. We have used three types of high-resolution phase screen as inputs, in the analysis part of our algorithm, and computed the singularity exponents on them. We have first tested our approach using the true phase

Table 6.6: Comparison of the residual phase statistics with classical operators under different levels of SNR. To estimate ϕ_{cor} using the MMF technique, we use the singularity exponents computed over the true phase as input high-resolution phase in the decomposition process of our algorithm.

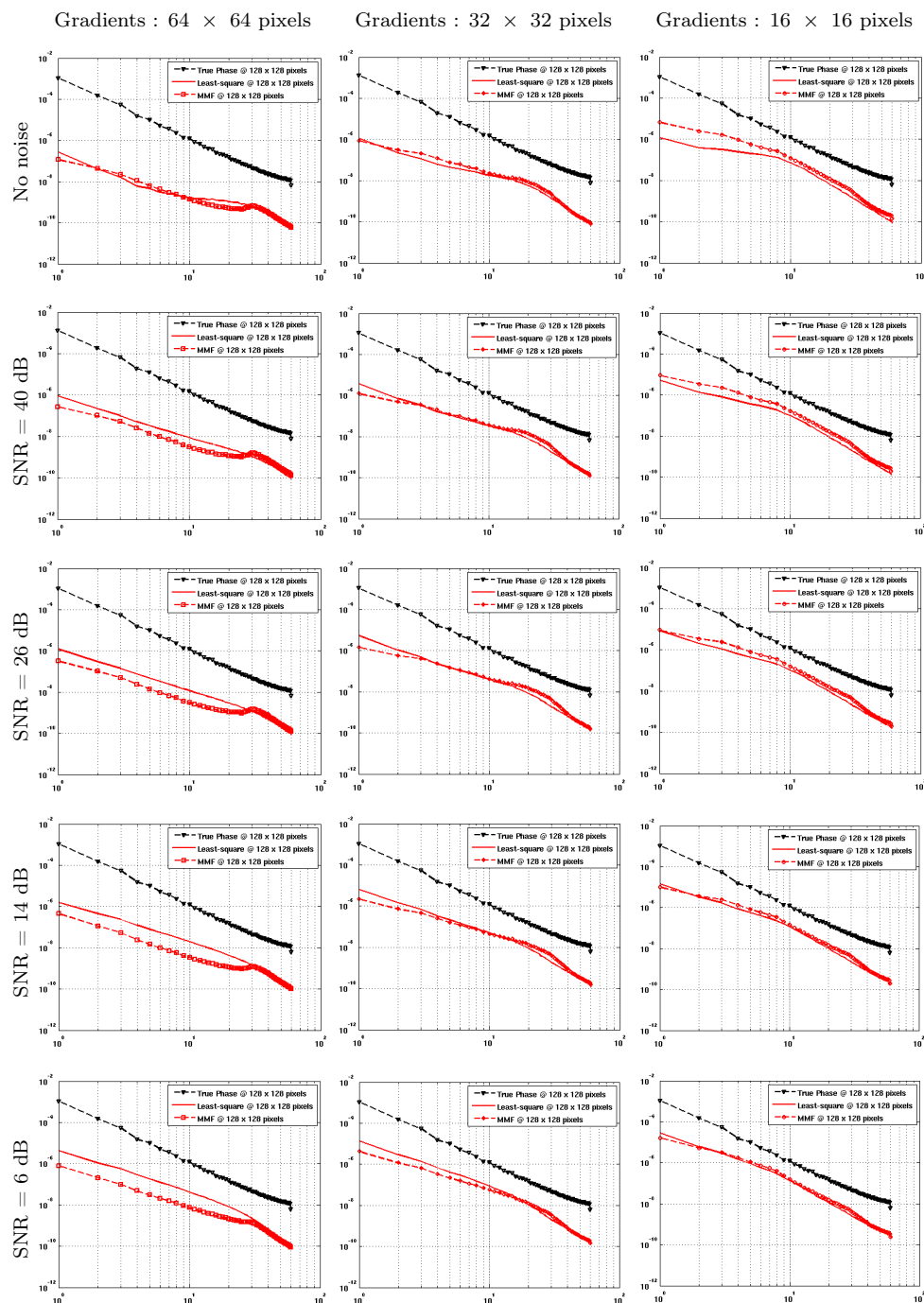


Table 6.7: Comparison of the residual phase statistics with classical operators under different levels of SNR. To estimate ϕ_{cor} using the MMF technique, we use the singularity exponents computed over the average phase instance (obtained by averaging the 10 previous and 10 post instances of the true phase) as input high-resolution phase in the decomposition process of our algorithm.

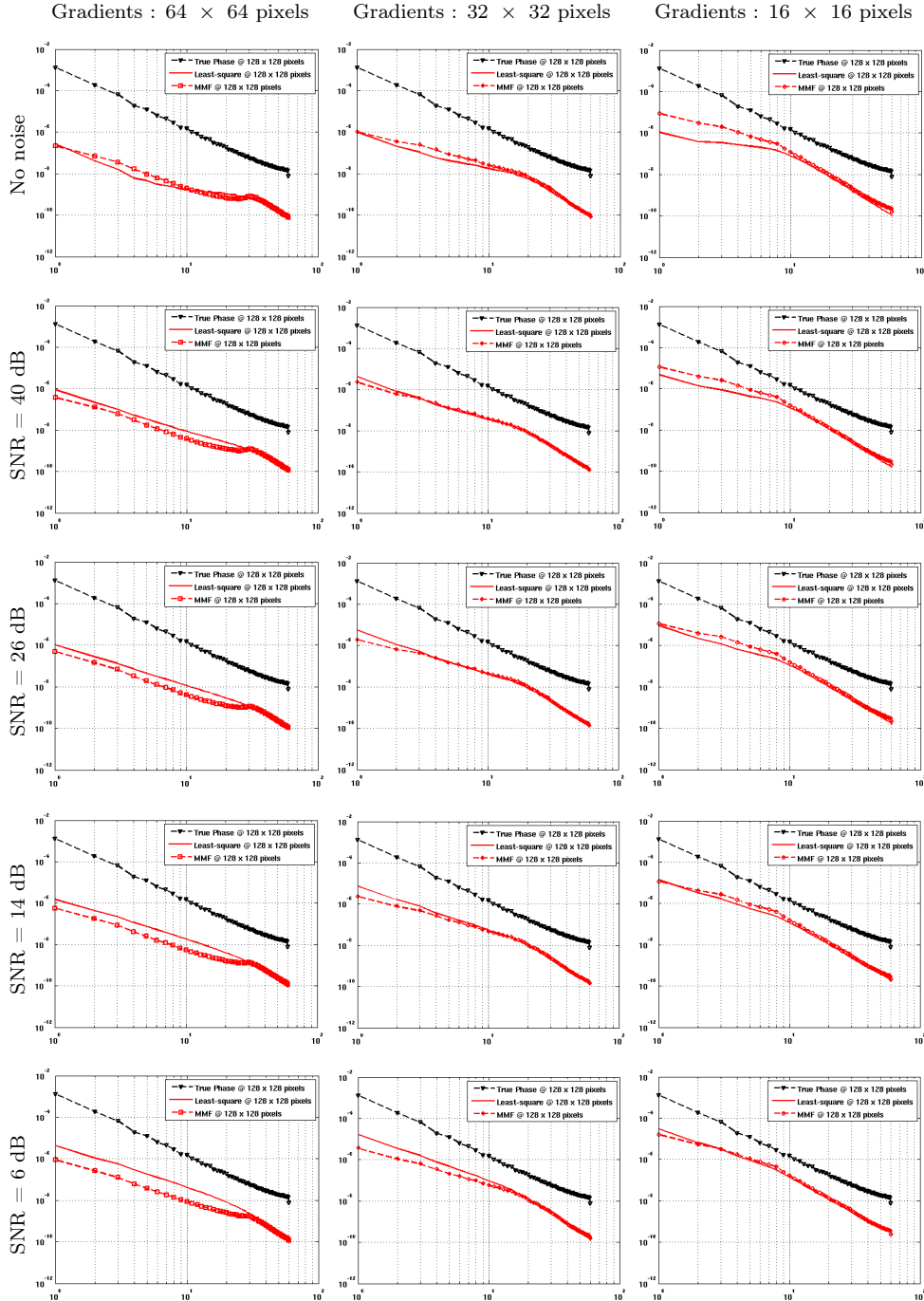
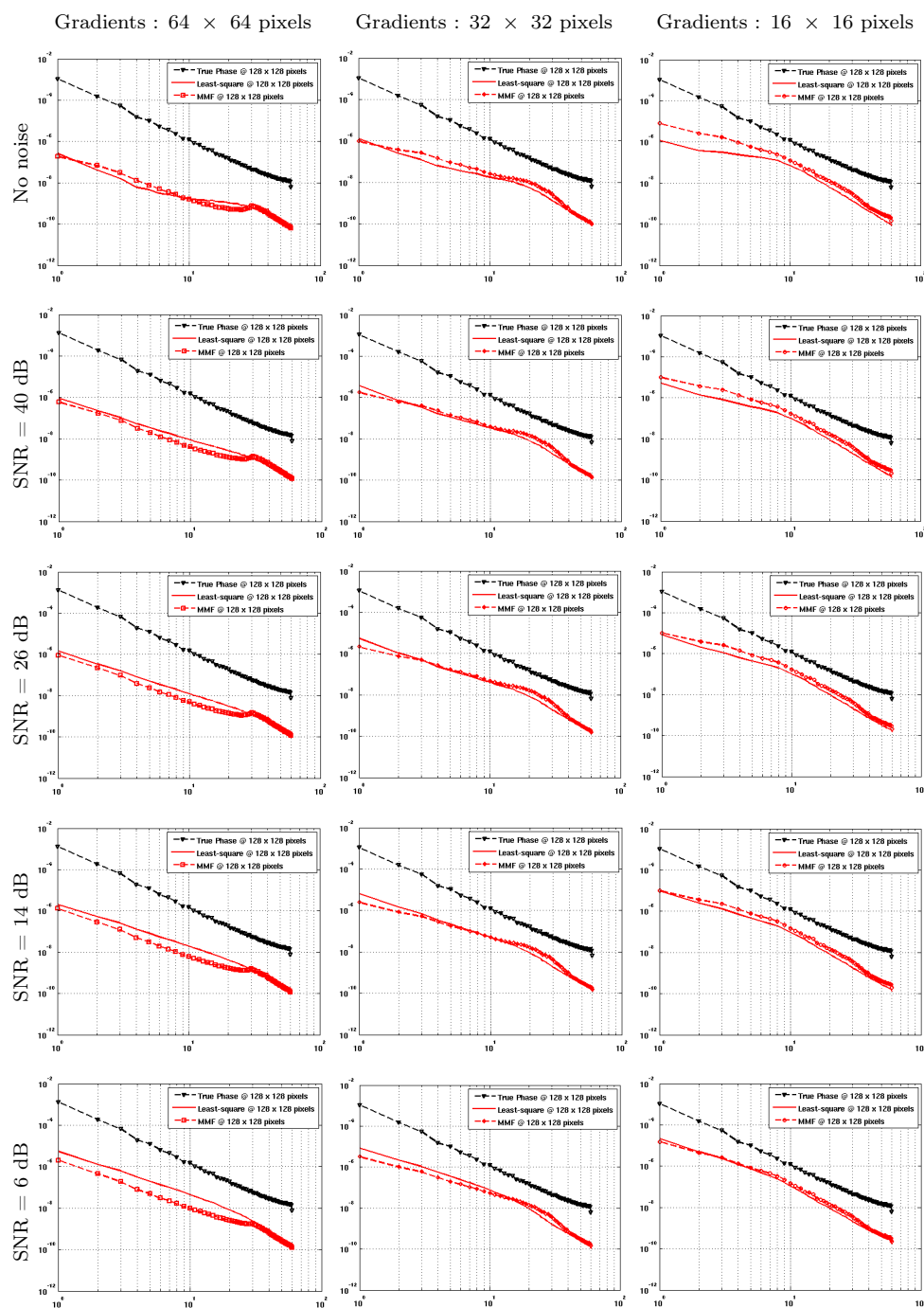


Table 6.8: Comparison of the residual phase statistics with the least squares operator under different levels of SNR. To estimate ϕ_{cor} using the MMF technique, we use the singularity exponents computed over a fixed FFT based Kolmogorov phase screen (see Fig 6.4) as input high-resolution phase in the decomposition process of our algorithm.



as an input (which is the ideal case) to verify the potential of our algorithm in estimating the phase. We then replaced the true phase with an average instance of the true phase (obtained by averaging the 10 previous and 10 post instances of the true phase) and with a fixed FFT based Kolmogorov phase screen (see Fig 6.4), and performed reconstruction. For all the three different high-resolution inputs, the results obtained shows superior performance under different levels of SNR (see table 6.6, table 6.7 and table 6.8) when compared with the classical least squares technique. It is seen that for the case when reconstruction is made over gradients of size 16×16 pixels, our method has reduced performance compared to least squares method. The performance however improves considerably, in comparison with the least squares method, as the level of SNR increases. It should be noted here that we have tested the performance of our algorithm in the case of Gaussian noise only. One important aspect will be to test the robustness of our algorithm in the case of sensor noise (photon noise + measurement noise), which is our future objective.

§ 6.6 CONCLUSION

In this chapter we have introduced a wavelet-based new method for the reconstruction of a high-resolution phase from its low-resolution gradients, by propagating the information of a turbulent phase along the scales, from low-resolution to high-resolution. We have proposed an alternate technique for estimating the wavefront phase instead of using the conventional methods of least squares solution [164]. The idea is the use of an optimal wavelet, which provides a close approximation of the multiscale energy cascade through wavelet decomposition. Since the deduction of an optimal wavelet remains an unsolved problem, we determine the quality of reconstruction by a classical multiresolution analysis on the signal of the singularity exponents, which we have proved in the previous chapter are the ideal candidates that retain the multiscale features of a signal. The results clearly state the fact that singularity exponents are the ideal candidates in capturing the turbulent information of the phase, and through the use of a proper wavelet (a third order

B-L wavelet in our case) the turbulent features of the signal are extracted along the scales, which is then used to reconstruct high-resolution gradients from its low-resolution measurements. The phase is then estimated from the high-resolution reconstructed gradients.

- CHAPTER 7 -

CONCLUSION

In this thesis, we have presented a novel approach to wavefront phase reconstruction in Adaptive Optics (AO) through the framework of MMF (Micro-canonical Multiscale Formalism). We have presented a detailed explanation of the MMF framework through its various applications on image processing and have successfully applied this framework, together with the multiresolution analysis scheme associated to wavelet transform, in the wavefront phase estimation problem for AO. The idea is the use of an optimal wavelet in multiresolution analysis, by which optimal inference along the scales of a signal is possible. But, due to the lack of proper computation techniques, we are limited to work only with an approximative version of the optimal wavelet. This limitation has inspired us to define, in this thesis, an alternate technique by which maximum inference along the scales is possible. We have shown that singularity exponents, associated to a turbulent phase acquisition, are ideal candidates for inferring information along the scales of a signal and can be used in a multiresolution analysis approach (associated to a wavelet transform) for reconstructing a turbulent phase from its low-resolution gradients. The justification of this idea, which forms of the heart of this thesis, has been done in two steps.

In the first step, we have studied the multiscale behaviour of a complex signal, better understood from its complex arrangement of geometrical structures (that are related to the cascading properties of physical variables [203]).

Transitions within these signals, can be well-defined by a subset of points that are related to the concept of edges in natural images. This is a fundamental topic as edges are usually considered as important multiscale features in a signal (in our case images) and better characterization of edges in complex signals can unfold its geometrical structure, which is our preliminary objective. From the concept of Statistical Physics, we see that systems with high order transitions commonly reflect a power-law behaviour in their thermodynamical variables [203, 202]. The exponents of this power-law, if determined correctly, can give tremendous insight into the underlying dynamics of such systems. The MMF provides a suitable approach in the determination of these critical exponents, the so-called *singularity exponents*, that has led to a sensible improvement in the numerical techniques for the determination of multiscale characteristics in real signals. In particular, the singularity exponents give access to a subset of points, called the Most Singular Manifold (the MSM) whose structure is related to *edges* or contours in natural images [197]. We see (in section 5.2, for the case of 2D signals) that this subset of points are much better candidates for the characterization of transitions in complex signals : they outperform the classical *linear filtering* approach of the state-of-the-art edge detectors in terms of consistency across the scales. Edges detected by singularity analysis are able to retain their structure across the scales. The results of section 5.2, therefore helps us in concluding that the singularity exponents are able to retain the important multiscale features of a signal along the scales.

After studying this important property of the singularity exponents, we move on to the second step of justification i.e., being able to reconstruct the signal from the basic information of its multiscale structure contained in the edges of the signal. Indeed, if edges encode the most important features of a signal, it should also be possible to reconstruct the whole signal from its edge representation. We therefore study the performance of reconstructible systems both with transitions associated to singularity exponents and the edge pixels provided by standard edge detection techniques. Examples are chosen among the most difficult natural signals: acquisition of turbulent phenomena (perturbated optical phase and ocean dynamics acquired from space). The results of section 5.3 clearly shows the superiority of the reconstruction, ob-

tained from the MSM points than over edges from classical edge detectors. By the application of different techniques for reconstructing an image from its edges, we see that the overall assumption of better reconstruction from MSM remains unchanged. The results allow us to draw another important conclusion : the singularity exponents not only retain the multiscale features of a signal, but it is also possible to reconstruct the signal from a subset of its most informative points.

After validating the idea of using the singularity exponents for optimal inference in multiresolution analysis, we demonstrate the potential of this idea, in chapter 6, for wavefront phase reconstruction. We study a multiresolution analysis scheme associated to the signal of singularity exponents through the approximation of an optimal wavelet. Three types of phase screens are used as high-resolution inputs to the multiresolution analysis part of our algorithm. The primary objective was to first validate the performance of our algorithm, for phase reconstruction, using the ground truth (i.e. the true phase) as input to the analysis part of the algorithm. The results encouraged the use of a non-perfect high resolution phase screen and verify the performance of reconstruction. We therefore took two examples of a non-perfect high-resolution phase as input to the analysis part: an average instance of the true phase (obtained by averaging the 10 previous and 10 post instances of the true phase) and a fixed Fourier series based atmospheric phase screen with Kolmogorov power spectrum. The results obtained, when compared with the classical least squares technique, clearly shows the potential of our approach in wavefront phase estimation, specially in the case of noise, where the performance of MMF is better than the least squares method.

§ 7.1 FUTURE PERSPECTIVES

The research reported in this thesis has opened a new direction to the problem of wavefront phase reconstruction in AO. Simulations clearly suggest the potential of this approach, as a new technique, superior or equal to classical solutions (with marked superiority in the case of noise, at least for the type of noise considered in this thesis).

- The future goal is, therefore, to implement our reconstruction algorithm in an AO system and see its performance in real-time. In fact, the singularity exponents, which are the basic ingredients used in our reconstruction technique, can be computed in real-time with minimum utilization of resources.
- The reconstruction technique that we have proposed in this thesis is general enough to suit the case of acquisitions of general complex systems. Therefore, the methodology is likely to be applicable to cases that fits the problem.

All these future extensions to the present work, may further justify the establishment of the MMF framework as a powerful tool in the analysis of multiscale features in complex signals. In fact, the potential of MMF is now being tested on many signal processing applications in a quite diverse set of scientific disciplines ranging from stock market series [151], phytoplankton distribution in ocean [157], ocean dynamics [217], satellite imaging [78, 77, 216], speech signal analysis [101, 100, 102], computer graphics [14] to natural image processing [197, 201].

§ 7.2 PUBLICATIONS

• Journal Publications

- S. K. Maji, H. Yahia and H. Badri: Reconstructing an image from its edge representation, **Digital Signal Processing, Elsevier**, 23 (6): 1867-1876, 2013.
- S. K. Maji and H. Yahia: Edges, Transitions and Criticality, **Pattern Recognition, Elsevier**, Accepted, 2013.

• Peer-reviewed conferences/proceedings

- S. K. Maji, O. Pont, H. Yahia and J. Sudre: Inferring Information across Scales in Acquired Complex Signals, **European Conf. Complex Systems**, Brussels, 2012.
- S. K. Maji, H. Yahia, O. Pont, J. Sudre, T. Fusco and V. Michau: Towards Multiscale Reconstruction of Perturbated Phase from Hartmann-Shack Acquisitions, **IEEE AHS**, Nuremberg, 2012.
- S. K. Maji, H. Yahia, O. Pont, T. Fusco, V. Michau and J. Sudre: A multiscale approach to phase reconstruction for Adaptive Optics, **IEEE ECMS**, Liberec, Czech Republic, 2011.

• Working papers

- S. K. Maji, H. Yahia, T. Fusco and H. Badri: A multifractal based wavefront phase estimation technique in ground based astronomy, in preparation for **IEEE Transactions on Aerospace and Electronic Systems**.
- H. Badri, H. Yahia, S. K. Maji and D. Aboutajdine: Edge-Based Sparse Coding of Color Images, in preparation for **IEEE ICIP 2014**.

BIBLIOGRAPHY

- [1] Carnegie mellon image database. <http://vasc.ri.cmu.edu/idb/>. 90
- [2] The fits format. <http://fits.gsfc.nasa.gov/>. 107
- [3] USC-SIPI image database. <http://sipi.usc.edu/database/>, 1981. xx, 77, 79, 90
- [4] A. Agrawal, R. Raskar, and R. Chellappa. What is the range of surface reconstructions from a gradient field ? *European Conf. Comp. Vision*, 2006. 84, 85, 86, 87, 88
- [5] N. Ahuja. A transform for multiscale image segmentation by integrated edge and region detection. *IEEE Trans. Pattern Anal. and Mach. Intelligence*, 18(12):1211–1235, 1996. 69
- [6] L. C. Andrews and R. L. Phillips. *Laser Beam Propagation through Random Media*. SPIE Press, Bellingham, WA, 2005. 10, 11
- [7] A. Arenodo, F. Argoul, E. Bacry, J. Elezgaray, and J. Muzy. *Ondelettes, Multifractales et Turbulence*. Diderot Editeur, Paris, 1995. 3, 4, 41, 47
- [8] R. Arsenault, R. Biasi, D. Gallieni, A. Riccardi, N. Hubin, E. Fedrigo, R. Donaldson, S. Oberti, and S. Stroebele. A deformable secondary mirror for the vlt. *Advances in Adaptive Optics II, Proc. of SPIE*, 6272:[6272–29], 2006. 27

-
- [9] F. Assémat, R. Wilson, and E. Gendron. Method for simulating infinitely long and non stationary phase screens with optimized memory storage. *Opt. Expr.*, 14:988–999, 2006. [20](#), [22](#)
- [10] J. J. Atick. Could information theory provide an ecological theory of sensory processing ? *Network: Comput. Neural Syst.*, 3:213–251, 1992. [69](#)
- [11] M. Azouit and J. Vernin. Optical turbulence profiling with balloons relevant to astronomy and atmospheric physics. *Publications of the Astronomical Society of the Pacific*, 117:536–543, 2005. [12](#)
- [12] H. W. Babcock. The possibility of compensating astronomical seeing. *Publications of the Astronomical Society of the Pacific*, 65:229, 1953. [2](#)
- [13] L. Baboulaz and P. L. Dragotti. Exact feature extraction using finite rate of innovation principles with an application to image super-resolution. *IEEE Trans. Image Process.*, 18:281–298, 2009. [1](#)
- [14] H. Badri. Computer graphics effects from the framework of reconstructible systems. *Master's thesis, Rabat faculty of science & INRIA Bordeaux Sud-Ouest*, 2012. [126](#)
- [15] R. G. Baraniuk, E. Candes, M. Elad, and Y. Ma. Applications of sparse representation and compressive sensing [scanning the issue]. *Proceedings of the IEEE*, 98:906–909, 2010. [7](#), [69](#)
- [16] R. G. Baraniuk, E. Candes, R. Nowak, and M. Vetterli. Compressive sampling. *IEEE Signal Processing Magazine*, 25:12–13, 2008. [7](#), [69](#)
- [17] R. G. Baraniuk, V. Cevher, M. F. Duarte, and C. Hegde. Model-based compressive sensing. *IEEE Transactions on Information Theory*, 56:1982–2001, 2010. [7](#), [69](#)
- [18] J. M. Bardsley. Wavefront reconstruction methods for adaptive optics systems on ground-based telescopes. *SIAM J. Matrix Analysis Applications*, 30:67–83, 2008. [16](#), [32](#), [36](#), [37](#), [116](#)
- [19] M. F. Barnsley. *Fractals Everywhere*. Academic Press, 1993. [43](#)

-
- [20] J. M. Beckers. Increasing the size of the isoplanatic patch with multi-conjugate adaptive optics. *Very Large Telescopes and their Instrumentation, ESO Conference and Workshop Proceedings*, 30:693–703, 1988. [2](#)
- [21] A. Beghi, A. Cenedese, and A. Masiero. Multiscale stochastic approach for phase screens synthesis. *Applied Optics*, 50:4124–4133, 2011. [106](#)
- [22] A. J. Bell and T. J. Sejnowski. The independent components of natural scenes are edge filters. *Vision Research*, 37:3327–3338, 1997. [69](#)
- [23] M. Le Bellac. Des phénomènes critiques aux champs de jauge, une introduction aux méthodes et aux applications de la théorie quantique des champs. *InterEditions/Editions du CNRS, collection Savoirs Actuels*, 1988. ISBN: 2-222-04026-4. [4](#)
- [24] R. Benzi, L. Biferale, A. Crisanti, G. Paladin, M. Vergassola, and A. Vulpiani. A random process for the construction of multi-affine fields. *Physica D: Nonlinear Phenomena*, 65, 1993. [xv](#), [65](#), [66](#)
- [25] C. R. Berger, S. Zhou, W. Chen, and P. Willett. Sparse channel estimation for ofdm: Over-complete dictionaries and super-resolution methods. *IEEE Intl. Workshop on Signal Process. Advances in Wireless Comm., Perugia, Italy*, 2009. [1](#)
- [26] F. Bergholm. Edge focusing. *IEEE Trans. Pattern Anal. and Mach. Intelligence*, 9(6):726–741, 1987. [70](#)
- [27] A. Bijaoui. Wavelets and astrophysical applications. *Wavelets in Physics*, 1999. [106](#)
- [28] A. Bijaoui. The wavelet transform: a digital eyepiece to improve our sky vision. *Observations & Travaux*, 70:5–13, 2008. [106](#)
- [29] A. Bijaoui, F. Rué, E. Slezak, and B. Vandame. A multiscale vision model and its applications to astronomical image analysis. *Astrophysics and Algorithms: a DIMACS workshop on Massive Astronomical Data Sets*, 1998. [106](#)

-
- [30] A. Bijaoui, E. Slezak, F. Rué, and E. Lega. Wavelets and the study of the distant universe. *Proceedings of The IEEE - PIEEE*, 84:670–679, 1996. 106
- [31] G. Boffetta, M. Cencini, M. Falcioni, and A. Vulpiani. Predictability: a way to characterize complexity, 2001. *Physics Reports* 356. 75
- [32] G. Boffetta, M. Cencini, M. Falcioni, and et al. Predictability: a way to characterize complexity. *Physics Reports*, 356:367–474, 2002. 4, 40
- [33] P. Bouthemy. A maximum likelihood framework for determining moving edges. *IEEE Trans. Pattern Anal. and Mach. Intelligence*, 11(5):499–511, 1989. 69
- [34] C. Boyer, V. Michau, and G. Rousset. Adaptive optics: interaction matrix measurements and real-time control algorithms for the come-on project. *Amplitude and Intensity Spatial Interferometry*, 406, 1990. 30
- [35] Ronald Newbold Bracewell and R. N. Bracewell. *The Fourier transform and its applications*. New York: McGraw-Hill, 1986. 35
- [36] Ronald Newbold Bracewell and A. Riddle. Inversion of fan-beam scans in radio astronomy. *The Astrophysical Journal*, 150:427, 1967. 35
- [37] J. Canny. A computational approach to edge detection. *IEEE Trans. Pattern Anal. and Mach. Intelligence*, 8(6):679–698, 1986. 69
- [38] S. Carlsson. Sketch based image coding. *In Proc. of Premier Colloque Image, Biarritz, France*, pages 71–77, 1984. 83
- [39] S. Carlsson. Sketch based coding of grey level images. *Signal Processing*, 15:57–83, 1988. 83
- [40] D. C. Chen, S. M. Jones, D. A. Silva, and S. S. Olivier. High-resolution adaptive optics scanning laser ophthalmoscope with dual deformable mirrors. *J. Opt. Soc. Am. A.*, 24:1305–1312, 2007. 2
- [41] J. J. Clark. Singularity theory and phantom edges in scale space. *IEEE Trans. Pattern Anal. and Mach. Intelligence*, 10(5):720–727, 1988. 70

-
- [42] W. Cochran, R. Plemmons, and T. Torgersen. Exploiting toeplitz structure in atmospheric image restoration. *Contemporary Mathematics*, 280, 2001. 15
- [43] S. Curtis, S. Shitz, and A. Oppenheim. Reconstruction of nonperiodic two-dimensional signals from zero crossings. *IEEE Trans. Acoust., Speech, Signal Process.*, 35:890–893, 1987. 83
- [44] G. M. Dai. Wavefront simulation for atmospheric turbulence. *Image Reconstruction and Restoration*, 62, 1994. 22
- [45] J. M. Delgado. Filtro optimo para imágenes naturales, aplicación al sistema visual. *PhD thesis, Universidad Autonoma de Madrid*, 2007. 53
- [46] M. Demerlé, P. Y. Madec, and G. Rousset. Servo-loop analysis for adaptive optics. *Adaptive Optics for Astronomy*, 73, 1994. 30
- [47] C. Denker, A. Tritschler, and M. Lofdahl. Image reconstruction. *Encyclopedia of Optical Engineering, R. Barry Johnson and Ronald G. Driggers (eds.), Marcel Dekker Inc., New York*, 2004. 15, 16
- [48] R. H. Dicke. Phase-contrast detection of telescope seeing errors and their correction. *Astrophysical Journal*, 198:605–615, 1975. 2
- [49] N. Doble. High-resolution, in vivo retinal imaging using adaptive optics and its future role in ophthalmology. *Expert Rev. Med. Devices*, 2:205–216, 2005. 2
- [50] J. H. Elder. Are edges incomplete? *Int. J. Comput. Vis.*, 34(2/3):97–122, 1999. 69, 82, 83, 84
- [51] J. H. Elder and S. W. Zucker. Local scale control for edge detection and blur estimation. *In: Proc. European Conf. Computer Vision*, pages 57–69, 1996. 82
- [52] J. H. Elder and S. W. Zucker. Local scale control for edge detection and blur estimation. *IEEE Trans. Pattern Anal. and Mach. Intelligence*, 20(7):699–716, 1998. 70, 82

-
- [53] B. L. Ellerbroek. First-order performance evaluation of adaptive-optics systems for atmospheric-turbulence compensation in extended-field-of-view astronomical telescopes. *J. Opt. Soc. Am. A.*, 11:783–805, 1994. [30](#)
- [54] B. L. Ellerbroek. Efficient computation of minimum-variance wave-front reconstructors with sparse matrix techniques. *J. Opt. Soc. Am. A*, 19, 2002. [37](#)
- [55] K. Falconer. *Fractal Geometry - Mathematical Foundations and Applications*. John Wiley & Sons, Chichester, 1990. [42](#), [43](#)
- [56] A. Fannjiang. Exact localization and superresolution with noisy data and random illumination. *arXiv:1008.3146*. [1](#)
- [57] O. Faugeras. *Three-dimensional computer vision:a geometric viewpoint*. MIT Press, 1993. ISBN: 0-262-06158-9. [69](#)
- [58] P. W. Fieguth and A. S. Willsky. Fractal estimation using models on multiscale trees. *IEEE Transactions on Signal Processing*, 44:1297–1300, 1996. [5](#)
- [59] J. C. Fontanella. Analyse de surface d’onde, déconvolution et optique adaptative. *J. Opt. (Paris)*, 16:257–268, 1985. [17](#)
- [60] D. Fraix-Burnet, J.-L. Nieto, and S. Roques. Image deconvolution applied to the 3c 273 jet. *Astronomy & Astrophysics*, 217:387–390, 1989. [106](#)
- [61] D. L. Fried. Optical resolution through a randomly inhomogeneous medium for very long and very short exposures. *J. Opt. Soc. Am. A*, 56:1372–1379, 1966. [12](#)
- [62] D. L. Fried. Least-square fitting a wave-front distortion estimate to an array of phase-difference measurements. *J. Opt. Soc. Am. A*, 67:370–375, 1977. [33](#)
- [63] D. L. Fried. Atmospheric turbulence optical effects: understanding the adaptive optics implications. pages 25–57, 1993. [36](#)

-
- [64] U. Frisch. *Turbulence*. Cambridge Univ. Press, Cambridge MA, 1995. [3](#), [43](#), [44](#), [51](#), [70](#), [76](#), [77](#), [79](#)
- [65] T. Fusco. Correction partielle et anisoplanétisme en optique adaptative: Traitements a posteriori et optique adaptative multiconjuguée. *PhD thesis, Université de Nice Sophia-Antipolis*, 2000. [9](#), [11](#), [12](#), [14](#), [15](#), [16](#), [17](#), [19](#), [20](#), [26](#), [28](#), [30](#), [32](#), [33](#), [34](#), [36](#)
- [66] T. Fusco, J. M. Conan, V. Michau, L. M. Mugnier, and G. Rousset. Efficient phase estimation for large-field-of-view adaptive optics. *Optics Letters*, 24:1472–1474, 1999. [105](#)
- [67] T. Fusco, J. M. Conan, V. Michau, G. Rousset, and F. Assemat. Multi-conjugate adaptive optics: Comparison of phase reconstruction approaches for large field of view. *Atmospheric Propagation, Proc. of SPIE*, 4167:168–179, 2000. [2](#), [105](#)
- [68] T. Fusco, J. M. Conan, G. Rousset, L. M. Mugnier, and V. Michau. Optimal wave-front reconstruction strategies for multiconjugate adaptive optics. *J. Opt. Soc. Am. A.*, 18:2527–2538, 2001. [105](#)
- [69] T. Fusco, C. Petit, G. Rousset, K. Dohlen, J. Chatron, P. Rabou, P. Feautrier, P. Baudoz, J. Beuzit, D. Mouillet, P. Puget, M. E. Kasper, M. D. Downing, E. Fedrigo, N. Hubin, and F. P. Wildi. Design of the extreme ao system for the planet finder instrument on the vlt. *Advances in Adaptive Optics II, Proc. of SPIE*, pages 6272–19, 2006. [2](#)
- [70] T. Fusco, J.-P. Véran, J. M. Conan, and L. M. Mugnier. Myopic deconvolution method for adaptive optics images of stellar fields. *Astron. Astrophys. Suppl. Ser.*, 134:193–200, 1999. [106](#)
- [71] D. Galun, M. Basri, and A. Brandt. Multiscale edge detection and fiber enhancement using differences of oriented means, 2007. International Conference on Computer Vision (ICCV). [70](#)
- [72] S. Geman and D. Geman. Stochastic relaxation, gibbs distribution and the bayesian restoration of images. *IEEE Trans. Pattern Anal. and Mach. Intelligence*, 6(6):721–741, 1984. [71](#)

-
- [73] A. S. Georghiades, P. N. Belhumeur, and D. J. Kriegman. From few to many: Illumination cone models for face recognition under variable lighting and pose. *IEEE Trans. Pattern Anal. and Mach. Intelligence*, 23:643–660, 2001. 84, 85
- [74] L. Gilles. Order-n sparse minimum-variance open-loop reconstructor for extreme adaptive optics. *Optics Letters*, 28:1927–1929, 2003. 37, 116
- [75] L. Gilles, C. R. Vogel, and B. L. Ellerbroek. A multigrid preconditioned conjugate gradient method for large scale wavefront reconstruction. *J. Opt. Soc. Am. A*, 19:1817–1822, 2002. 37, 116
- [76] P. Grattoni and A. Guiducci. Contour coding for image description. *Pattern Recognition Letters*, 11:95–105, 1990. 84
- [77] J. Grazzini, A. Turiel, and H. Yahia. Multifractal formalism for remote sensing: A contribution to the description and the understanding of meteorological phenomena in satellite images. *Complexus Mundi. Emergent Patterns in Nature*, pages 247–256, 2006. 126
- [78] J. Grazzini, A. Turiel, H. Yahia, and I. Herlin. Edge-preserving smoothing of high-resolution images with a partial multifractal reconstruction scheme. *International Society for Photogrammetry and Remote Sensing (ISPRS)*, 2004. 126
- [79] W. E. L. Grimson. From images to surfaces: A computational study of the human early visual system. *The MIT Press, Cambridge, Massachusetts*, 1981. 84
- [80] A. Habib, J. Vernin, and Z. Benkhaldoun. Atmospheric-turbulence characterization by single-star scintillation analysis. *Comptes Rendus Physique*, 6:385–392, 2005. 12
- [81] F. R. Hampel, E. M. Ronchetti, P. J. Rousseeuw, and W. A. Stahel. *Robust statistics: the approach based on influence functions*. Wiley.com, 2011. 86

-
- [82] R. M. Haralick. Digital step edges from zero crossing of second directional derivatives. *IEEE Trans. Pattern Anal. and Mach. Intelligence*, 6(1):58–68, 1984. 69
- [83] C. M. Harding, R. A. Johnston, and R. G. Lane. Fast simulation of a kolmogorov phase screen. *Applied Optics*, 38:2161–2170, 1999. 20
- [84] J. W. Hardy. *Adaptive optics for astronomical telescopes*. Adaptive optics for astronomical telescopes, 1998. 12
- [85] J. Hartmann. Bemerkungen über den bau und die justirung von spektrographen. *Zt. Instrumentenk.*, 29, 1990. 27
- [86] J. Herrmann. Least-squares wave front errors of minimum norm. *J. Optical Society of America*, 70:28–35, 1980. 34
- [87] E. Hildreth. Implementation of a theory of edge detection, 1980. Massachusetts Inst. Technol., Cambridge, A. 1. Memo 579. 69
- [88] R. H. Hudgin. Wave-front reconstruction for compensated imaging. *J. Opt. Soc. Am. A*, 67, 1977. 33
- [89] R. Hummel and R. Moniot. Reconstructions from zero crossings in scale space. *IEEE Trans. Acoust., Speech, Signal Process.*, 37(12):2111–2130, 1989. 83, 84
- [90] W. Mc Ilhagga. The canny edge detector revisited. *Int. J. Comput. Vis.*, 91:251–261, 2011. DOI 10.1007/s11263-010-0392-0. 69
- [91] W. W. Irving, P. W. Fieguth, and A. S. Willsky. An overlapping tree approach to multiscale stochastic modeling and estimation. *IEEE Trans. on Image Process.*, 6:1517–1529, 1997. 5
- [92] W. W. Irving, L. M. Novak, and A. S. Willsky. A multiresolution approach to discrimination in sar imagery. *IEEE Transactions on Aerospace and Electronic Systems*, 33:1157–1169, 1997. 5
- [93] A. Ishimaru. *Wavefront Propagation and Scattering in Random Media*. Academic, New York, 1978. 10

-
- [94] G. Rousset J. Primot and J. C. Fontanella. Deconvolution from wave front sensing: a new technique for compensating turbulence-degraded images. *J. Opt. Soc. Am. A*, 7:1598–1608, 1990. 17
- [95] P. Jeong and C. I. Kim. Adaptive determination of filter scales for edge detection. *IEEE Trans. Pattern Anal. and Mach. Intelligence*, 14(15):579–585, 1992. 70
- [96] M. E. Jernigan and R. W. Wardell. Does the eye contain optimal edge detection mechanisms ? *IEEE Trans. Syst., Man, Cybern.*, SMC-11:441–444, 1981. 69
- [97] M. Kasper, D. P. Looze, S. Hippler, T. Herbst, A. Glindemann, T. Ott, and A. Wirth. Alfa: Adaptive optics for the calar alto observatory optics, control systems, and performance. *Experimental Astronomy*, 10:49–73, 2000. 27
- [98] A. K. Katsaggelos. Digital image restoration. *Springer Series in Information Information Sciences*, Springer-Verlag, Berlin, 1991. 34, 105
- [99] V. Khanagha. Novel multiscale methods for nonlinear speech analysis. *PhD thesis, Université de Bordeaux 1*, 2013. 46
- [100] V. Khanagha and K. Daoudi. Efficient multipulse approximation of speech excitation using the most singular manifold. *IEEE Interspeech*, 2012. 6, 126
- [101] V. Khanagha, K. Daoudi, O. Pont, H. Yahia, and A. Turiel. Improving text-independent phonetic segmentation based on the microcanonical multiscale formalism. *Proceedings of the International Conference on Acoustics, Speech, and Signal Processing (ICASSP)*, 2011. 126
- [102] V. Khanagha, K. Daoudi, O. Pont, H. Yahia, and A. Turiel. Non-linear speech representation based on local predictability exponents. *Neurocomputing Journal*, 2013. 126
- [103] R. Kimmel and A. M. Bruckstein. Regularized laplacian zero crossings as optimal edge integrators. *Int. J. Comput. Vis.*, 53(3):225–243, 2003. 69

-
- [104] V. A. Korhikoski. Improving the performance of adaptive optics systems with optimized control methods. *PhD thesis, Helsinki University of Technology*, 2008. 2
- [105] P. Kovess. Image features from phase congruency. *Journal of Computer Vision Research*, 1999. 71
- [106] A. Labeyrie. Attainment of diffraction limited resolution in large telescopes by fourier analysing speckle patterns in star images. *Astronomy and Astrophysics*, 6:85, 1970. 18
- [107] O. Laligant and F. Truchetet. A nonlinear derivative scheme applied to edge detection. *IEEE Trans. Pattern Anal. and Mach. Intelligence*, 32(2):242–257, 2010. xvi, 69, 76, 94, 102
- [108] R. G. Lane, A. Glindemann, and J. C. Dainty. Simulation of a kolmogorov phase screen. *Waves in Random Media*, 2:209–224, 1992. 20, 22
- [109] A. Lesne. *Méthodes de renormalisation*. Eyrolles Science, 1995. ISBN: 2-212-05830-6. 4, 70
- [110] W. Y. V. Leung. Inverse problems in astronomical and general imaging. *PhD thesis, University of Canterbury*, 2002. 35, 106, 116
- [111] F. Levet and X. Granier. Improved skeleton extraction and surface generation for sketch-based modeling. *Proceedings of Graphics Interface*, 2007. 69
- [112] S. Z. Li. Close-form solution and parameter selection for convex minimization-based edge-preserving smoothing. *IEEE Trans. Pattern Anal. and Mach. Intelligence*, 20(9):916–932, 1998. 71
- [113] P. Liang and Y. W. Wang. Local scaled controlled anisotropic diffusion with local noise estimate for image smoothing and edge detection, 1998. Sixth International Conference on Computer Vision (ICCV), Narosa Publishing House. 70

-
- [114] T. Lindeberg. *Scale-Space Theory in Computer Vision*. Kluwer Academic Publishers, 1994. ISBN: 0-7923-9418-6. 70
- [115] T. Lindeberg. Edge detection and ridge detection with automatic scale selection. *Int'l J. Comput. Vis.*, 30:117–154, 1998. xx, 77, 80, 81, 94
- [116] T. Lindeberg and ter Haar Romeny. *Linear scale-space: (I) Basic theory and (II) Early visual operations*, Geometry-Driven Diffusion. Kluwer Academic Publishers/Springer, Dordrecht, Netherlands, 1994. 77
- [117] H. K. Liu. Two- and three-dimensional boundary detection. *Comput. Graphics Image Processing*, 6:123–134, 1977. 69
- [118] B. F. Logan. Information in the zero-crossings of bandpass signals. *Bell Syst. Tech. J.*, 56:487–510. 83
- [119] S. Lovejoy and D. Schertzer. Multifractals, universality classes, satellite and radar measurements of clouds and rain. *Journal of Geophysical Research*, 95:2021–2034, 1990. 40
- [120] W. H. H. J. Lunscher. The asymptotic optimal frequency domain filter for edge detection. *IEEE Trans. Pattern Anal. and Mach. Intelligence*, 5(6):678–680, 1983. 69
- [121] W. H. H. J. Lunscher and M. P. Beddoes. Optimal edge detector design i: Parameter selection and noise effects. *IEEE Trans. Pattern Anal. and Mach. Intelligence*, 8(2):164–177, 1986. 69
- [122] P. Y. Madec. *Control techniques, in Adaptive Optics in Astronomy*, F. Roddier, ed. Cambridge University Press, Cambridge, U.K, 1999. 30
- [123] P. Y. Maeda. Zernike polynomials and their use in describing the wavefront aberrations of the human eye. <http://scien.stanford.edu/pages/labsite/2003/psych221/projects/03/pmaeda/index.html>. 18

-
- [124] S. K. Maji, O. Pont, H. Yahia, and J. Sudre. Inferring information across scales in acquired complex signals. *European Conf. Complex Systems, Brussels*, 2012. 3, 6
- [125] S. K. Maji, H. Yahia, and H. Badri. Reconstructing an image from its edge representation. *Digital Signal Processing, Elsevier*, 2013. In Press. 5, 6, 54
- [126] S. K. Maji, H. Yahia, O. Pont, T. Fusco, V. Michau, and J. Sudre. A multiscale approach to phase reconstruction for adaptive optics. *IEEE ECMS, Liberec, Czech Republic*, 2011. 106
- [127] S. K. Maji, H. Yahia, O. Pont, J. Sudre, T. Fusco, and V. Michau. Towards multiscale reconstruction of perturbed phase from hartmann-shack acquisitions. *IEEE AHS, Nuremberg*, 2012. 106
- [128] S. Mallat. *A wavelet tour of signal processing*. Academic Press, 1999. 56, 58, 59, 70, 77
- [129] S. Mallat and W. L. Hwang. Singularity detection and processing with wavelets. *IEEE Transactions on Information Theory*, 38:617–643, 1992. 70, 80
- [130] S. Mallat and S. Zhong. Characterization of signals from multiscale edges. *IEEE Trans. Pattern Anal. and Mach. Intelligence*, 14(7):710–732, 1992. xix, 70, 78, 80, 84
- [131] B. B. Mandelbrot. *The Fractal Geometry of Nature*. New York: W. H. Freeman and Co., 1982. ISBN 0-7167-1186-9. 41
- [132] D. H. Marimont and Y. Rubner. A probabilistic framework for edge detection and scale selection, 1998. Sixth International Conference on Computer Vision (ICCV), Narosa Publishing House. 70
- [133] D. Marr and E. Hildreth. Theory of edge detection. *Proc. Royal Soc. London B*, 207:187–217, 1980. 69, 83

- [134] B. L. McGlamery. Computer simulation studies of compensation of turbulence degraded images. *in Image Processing*, 74:225–223, 1976. xvii, 20, 22, 116, 117
- [135] D. G. Morgenthaler and A. Rosenfeld. Multidimensional edge detection by hypersurface fitting. *IEEE Trans. Pattern Anal. and Mach. Intelligence*, 3(4):482–486, 1981. 69
- [136] M. C. Morrone and D. C. Burr. Feature detection in human vision: A phase-dependent energy model. *Proc. Royal Soc. London B*, 1988. 71
- [137] L. Mugnier, G. Le Besnerais, and S. Meimon. *Inversion in optical imaging through atmospheric turbulence in Bayesian approach to inverse problems*. Jérôme Idier ed., ISTE, John Wiley & Sons Inc., 2008. ISBN: 878-1-84821-032-5. 3, 28, 34, 35, 105
- [138] L. M. Mugnier, C. Robert, J.-M. Conan, V. Michau, and S. Salem. Myopic deconvolution from wavefront sensing. *J. Optical Society of America*. 17, 106
- [139] L. M. Mugnier, C. Robert, J.-M. Conan, V. Michau, and S. Salem. Regularized multiframe myopic deconvolution from wavefront sensing, 1999. Proc. SPIE 3763, Propagation and Imaging through the Atmosphere III. 17
- [140] S. Muraki, N. Yokoya, and K. Yamamoto. Surface reconstruction from a contour line image by regularization. *Systems and Computers in Japan*, 23(2):81–91, 1992. 84
- [141] T. Nakajima. Signal-to-noise ratio of the bispectral analysis of speckle interferometry. *J. Opt. Soc. Am. A*, 5:1477–1491, 1988. 22
- [142] V. S. Nalwa and T. O. Binford. On detecting edges. *IEEE Trans. Pattern Anal. and Mach. Intelligence*, 8(6):699–714, 1986. 69
- [143] R. J. Noll. Zernike polynomials and atmospheric turbulence. *J. Optical Society of America*, 66:207–211, 1976. 14, 18, 19, 21

-
- [144] R. J. Noll. Phase estimates from slope-type wave-front sensors. *J. Optical Society of America*, 68:139–140, 1978. [34](#)
- [145] A. M. Obukhov. The structure of the temperature field in a turbulent flow. *Izv. Akad. Nauk. SSSR, Ser. Geogr. and Geophys.*, 13:58–69, 1949. [11](#)
- [146] R. Pacanowski, X. Granier, C. Schlick, and P. Poulin. Sketch and paint-based interface for highlight modeling. *Eurographics Workshop on Sketch-Based Interfaces and Modeling*, 2008. [69](#)
- [147] G. Parisi and U. Frisch. On the singularity structure of fully developed turbulence turbulence and predictability in geophysical fluid dynamics. *Proc. Intl School of Physics E. Fermi ed*, pages 84–7, 1985. [40](#), [47](#), [51](#)
- [148] P. Perona and J. Malik. Scale-space and edge detection using anisotropic diffusion. *IEEE Trans. Pattern Anal. and Mach. Intelligence*, 12(7):629–639, 1990. [70](#), [85](#), [87](#)
- [149] J. A. Perreault, T. G. Bifano, B. M. Levine, and M. N. Horenstein. Adaptive optic correction using microelectromechanical deformable mirrors. *Optical Engineering*, 41:561–566, 2002. [27](#)
- [150] I. Pitas and A. N. Venetsalopoulos. Edge detectors based on nonlinear filters. *IEEE Trans. Pattern Anal. and Mach. Intelligence*, 8(4):538–550, 1986. [69](#)
- [151] O. Pont. Universality in multiscale, turbulent-like self-organization: from algal blooms to heartbeat to stock market dynamics. *IFISC*, 2008. [41](#), [126](#)
- [152] O. Pont, A. Turiel, and C. Perez-Vicente. On optimal wavelet bases for the realization of microcanonical cascade processes. *International Journal of Wavelets Multiresolution and Information Processing*, 9:35–61, 2011. [5](#), [53](#)
- [153] O. Pont, A. Turiel, and C. J. Pérez-Vicente. Application of the microcanonical multifractal formalism to monofractal systems. *Physical Review E*, 74:061110–061123, 2006. [75](#)

- [154] O. Pont, A. Turiel, and C. J. Pérez-Vicente. Empirical evidences of a common multifractal signature in economic, biological and physical systems. *Physica A*, 388:2025–2035, 2009. doi:10.1016/j.physa.2009.01.041. 4, 41, 43, 45
- [155] O. Pont, A. Turiel, and H. Yahia. An optimized algorithm for the evaluation of local singularity exponents in digital signals, 2011. 14th International Workshop on Combinatorial Image Analysis (IWCIA 2011), LNCS 6636. 4, 49, 75
- [156] C. Pottier. Combinaison multi-capteurs de données de couleur de l'eau : Application en océanographie opérationnelle. *PhD thesis, Université Toulouse III*, 2006. 5
- [157] C. Pottier, A. Turiel, and V. Garçon. Inferring missing data in satellite chlorophyll maps using turbulent cascading. *Remote Sensing of Environment*, 112:4242–4260, 2008. 62, 66, 106, 126
- [158] F. Quiros-Pacheco. Reconstruction and control laws for multi-conjugate adaptive optics in astronomy. *PhD thesis, Imperial College London*, 2007. 2, 16, 26, 27
- [159] A. Riccardi, G. Brusa, M. Xompero, D. Zannotti, C. Del Vecchio, P. Salinari, P. Ranfagni, D. Gallieni, M. Andrihattoni, S. Miller, and P. Mantegazza. The adaptive secondary mirrors for the large binocular telescope: a progress report. *Advancements in Adaptive Optics, Proc. of SPIE*, 5490:1564–1571, 2004. 27
- [160] F. Rigaut. Ground conjugate wide field adaptive optics for the elts. *ESO Conf. Beyond conventional adaptive optics*, 58:11–16, 2002. 2
- [161] F. Rigaut, G. Rousset, P. Kern, J. C. Fontanella, J. P. Gaffard, F. Merkle, and P. Lena. Adaptive optics on a 3.6-m telescope - results and performance. *Astronomy and Astrophysics*, 250:280–290, 1991. 27
- [162] F. Roddier. The effects of atmospheric turbulence in optical astronomy. *Progress in Optics*, pages 283–376, 1981. 14, 16

-
- [163] F. Roddier. Curvature sensing and compensation - a new concept in adaptive optics. *Applied Optics*, 27:1223–1225, 1988. [3](#), [27](#)
- [164] F. Roddier. *Adaptive optics in astronomy*. Cambridge University Press, Cambridge, U.K, 1999. [2](#), [3](#), [18](#), [26](#), [27](#), [28](#), [30](#), [31](#), [32](#), [33](#), [34](#), [35](#), [36](#), [105](#), [106](#), [121](#)
- [165] N. Roddier. Atmospheric wave-front simulation using zernike polynomials. *Opt. Eng.*, 29:1174–1180, 1990. [21](#)
- [166] G. Rodrigues. Adaptive optics with segmented deformable bimorph mirrors. *PhD thesis, Université Libre de Bruxelles*, 2010. [30](#), [33](#)
- [167] M. C. Roggemann and B. M. Welsh. *Imaging Through Turbulence*. CRC Press, Inc., New York, NY, 1996. [11](#), [15](#), [19](#), [22](#)
- [168] S. Roques, F. Bourzeix, and K. Bouyoucef. Soft-thresholding technique and restoration of 3c273 jet. *Astrophysics and Space Science*, 239:297–304, 1996. [106](#)
- [169] S. Roques, B. Serre, and N. Dolez. Band-limited interpolation applied to the time series of rapidly oscillating stars. *Monthly Notices of The Royal Astronomical Society*, 308:876–886, 1999. [17](#), [106](#)
- [170] G. Rousset. *Wave-front sensing, in Adaptive Optics in Astronomy, F. Roddier, ed.* Cambridge University Press, Cambridge, U.K, 1999. [2](#), [3](#), [28](#), [29](#)
- [171] G. Rousset and J.-L. Beuzit. *The COME-ONE/ADONIS systems, in Adaptive Optics in Astronomy, F. Roddier, ed.* Cambridge University Press, Cambridge, U.K, 1999. [2](#)
- [172] G. Rousset, J. C. Fontanella, P. Kern, P. Gigan, F. Rigaut, P. Lena, C. Boyer, P. Jagourel, J. P. Gaffard, and F. Merkle. 1st diffraction-limited astronomical images with adaptive optics. *Astronomy and Astrophysics*, 230:L29–L32, 1990. [2](#)
- [173] G. Rousset, F. Lacombe, P. Puget, N. Hubin, E. Gendron, J.-M. Conan, P. Kern, P.-Y. Madec, D. Rabaud, D. Mouillet, A.-M. Lagrange, and

- F. Rigaut. Design of the nasmyth adaptive optics system (naos) of the vlt, astronomical telescopes and instrumentation. *Proc. Soc. Photo-Opt. Instrum. Eng.*, 3353, 1998. 28
- [174] F. Rué and A. Bijaoui. Pyramidal vision model applied to astronomical images. *Wavelet Applications in Signal and Image Processing IV, Proc. SPIE*, 2825:373–383, 1996. 106
- [175] R. A. Salinas, C. Richardson, M. A. Abidi, and R. C. Gonzalez. Data fusion: Color edge detection and surface reconstruction through regularization. *IEEE Transactions on Industrial Electronics*, 43(3):355–363, 1996. 84
- [176] P. Sarkar and K. L. Boyer. On optimal infinite impulse response edge detection filters. *IEEE Trans. Pattern Anal. and Mach. Intelligence*, 13(11):1154–1171, 1991. 69
- [177] R. J. Sasiela and J. G. Mooney. An optical phase reconstructor based on using a multiplier, accumulator approach. *Proc. SPIE*, 55:170–176, 1985. 35, 36
- [178] D. Schleicher. Hausdorff dimension, its properties, and its surprises. *American Mathematical Monthly*, 114:509–528, 2007. 42
- [179] J. D. Schmidt. Free-space optical communications performance enhancement by use of a single adaptive optics correcting element. *Ph.D. thesis, University of Dayton*, 2006. 10
- [180] C. Schwartz, G. Baum, and E. N. Ribak. Turbulence-degraded wave fronts as fractal surfaces. *J. Opt. Soc. Am. A.*, 11:444–451, 1994. 106
- [181] M. Séchaud. *Wave-front compensation devices, in Adaptive Optics in Astronomy*, F. Roddier, ed. Cambridge University Press, Cambridge, U.K, 1999. 27
- [182] G. Sedmak. Implementation of fast-fourier-transform-based simulations of extra-large atmospheric phase and scintillation screens. *Appl. Opt.*, 43:4527–4538, 2004. 20, 22

-
- [183] R. Shack. Production and use of a lenticular hartmann screen. *J. Opt. Soc. Am. A*, 61, 1971. 27
- [184] K. S. Shanmugham, F. M. Dickey, and J. A. Green. An optimal frequency domain filter for edge detection in digital pictures. *IEEE Trans. Pattern Anal. and Mach. Intelligence*, 1(1):37–49, 1979. 69
- [185] Z. S. She and E. Leveque. Universal scaling laws in fully developed turbulence. *Phys. Rev. Lett.*, 72:336–9, 1994. 3, 40
- [186] W. H. Southwell. Wave-front estimation from wave-front slope measurements. *J. Optical Society of America*, 70:998–1006, 1980. 32
- [187] H. E. Stanley. *Introduction to Phase Transitions and Critical Phenomena*. Oxford Science Publications, 1971. ISBN: 0-19-505316-8. 4
- [188] J.-L. Starck, F. Murthag, and J. M. Fadili. *Sparse Image and Signal Processing: wavelets, curvelets, morphological diversity*. Cambridge University Press, 2010. 70, 106
- [189] K. Suzuki, I. Oriba, and N. Sugie. Neural edge enhancer for supervised edge enhancement from noisy images. *IEEE Trans. Pattern Anal. and Mach. Intelligence*, 25(12):1582–1596, 2003. 71
- [190] A. J. Tabatabai and R. Mitchell. Edge location to subpixel values in digital imagery. *IEEE Trans. Pattern Anal. and Mach. Intelligence*, 6(2):188–201, 1984. 69
- [191] V. Y. F. Tan, A. Anandkumar, L. Tong, and A. S. Willsky. A large-deviation analysis for the maximum-likelihood learning of markov tree structures. *IEEE Transactions on Information Theory*, 57:1714–1735, 2011. 5
- [192] H. Tennekes and J. L. Lumley. A first course in turbulence. *M.I.T. Press, Cambridge [Mass.] and London*, 1972. 9
- [193] A. Tokovinin. Cfio overview of adaptive optics. <http://www.ctio.noao.edu/~atokovin/tutorial/intro.html>. 14, 16, 28, 32

-
- [194] A. Tokovinin. Seeing improvement with ground-layer adaptive optics. *Publications of the Astronomical Society of the Pacific*, 116:941–951, 2004. [12](#)
- [195] V. Torre and T. A. Poggio. On edge detection. *IEEE Trans. Pattern Anal. and Mach. Intelligence*, 8(2):147–163, 1986. [69](#), [70](#)
- [196] Y. Traonmilin, S. Ladjal, and A. Almansa. Quantification de la robustesse de la super-résolution par minimisation l1. *GRETSI, Brest, France*, 2013. [1](#)
- [197] A. Turiel and A. del. Pozo. Reconstructing images from their most singular fractal manifold. *IEEE Trans. Image Process.*, 11:345–350, 2002. [7](#), [39](#), [48](#), [73](#), [84](#), [87](#), [88](#), [124](#), [126](#)
- [198] A. Turiel, J. M. Delgado, and N. Parga. Learning efficient internal representations from natural image collections. *Neurocomputing*, 58-60:915–921, 2004. [5](#), [62](#)
- [199] A. Turiel, G. Mato, N. Parga, and J. P. Nadal. The self-similarity properties of natural images resemble those of turbulent flows. *Physical Review Letters*, 80:1098–1101, 1998. [5](#), [62](#)
- [200] A. Turiel, J.-P. Nadal, and N. Parga. Orientational minimal redundancy wavelets: from edge detection to perception. *Vision Research*, 43:1061–1079, 2003. [53](#)
- [201] A. Turiel and N. Parga. The multifractal structure of contrast changes in natural images: From sharp edges to textures. *Neural Computation*, 12:763–793, 2000. [40](#), [50](#), [54](#), [69](#), [77](#), [126](#)
- [202] A. Turiel, C. J. Pérez-Vicente, and J. Grazzini. Numerical methods for the estimation of multifractal singularity spectra on sampled data: A comparative study. *Journal of Computational Physics*, 216:362–390, 2006. [3](#), [4](#), [41](#), [44](#), [45](#), [47](#), [49](#), [70](#), [73](#), [74](#), [106](#), [124](#)
- [203] A. Turiel, H. Yahia, and C. J. Pérez-Vicente. Microcanonical multifractal formalism -a geometrical approach to multifractal systems: Part i.

- singularity analysis. *J. Phys. A: Math. Theor.*, 41(015501), 2008. [4](#), [7](#), [39](#), [43](#), [44](#), [45](#), [46](#), [47](#), [48](#), [50](#), [72](#), [73](#), [84](#), [88](#), [106](#), [123](#), [124](#)
- [204] J. Vallerga, J. McPhate, A. Tremsin, O. Siegmund, B. Mikulec, and A. Clark. Optically sensitive medipix2 detector for adaptive optics wavefront sensing. *Nuclear Instruments and Methods in Physics Research Section A: Accelerators, Spectrometers, Detectors and Associated Equipment*, 546:263–269, 2005. [xiii](#), [26](#)
- [205] J. H. van Hateren. Theoretical predictions of spatiotemporal receptive fields of fly lmc8, and experimental validation. *J. Comp. Physiology A*, 171:157–170, 1992. [69](#)
- [206] J. H. van Hateren and A. van der Schaaf. Independent component filters of natural images compared with simple cells in primary visual cortex, 1998. *Proc.R. Soc. Lond.*, B265. [69](#), [75](#), [90](#)
- [207] J. Vernin, R. Barletti, G. Ceppatelli, L. Paterno, A. Righini, and N. Speroni. Optical remote sensing of atmospheric turbulence: a comparison with simultaneous thermal measurements. *Applied Optics*, 18:243–247, 1979. [12](#)
- [208] S. J. Wang and T. O. Binford. Generic, model-based estimation and detection of discontinuities in image surfaces. *Proceedings of 1994 ARPA Image Understanding Workshop*, pages 1443–1449, 1994. [84](#)
- [209] X. Wang. Laplacian operator-based edge detectors. *IEEE Trans. Pattern Anal. and Mach. Intelligence*, 29(15):886–890, 2007. [69](#)
- [210] Z. Wang, A. C. Bovik, H. R. Sheikh, and E. P. Simoncelli. Image quality assessment: From error visibility to structural similarity. *IEEE Trans. Image Process.*, 13(4):600–612, 2004. [90](#), [93](#)
- [211] Z. Wang and E. P. Simoncelli. Local phase coherence and the perception of blur. *Adv. Neural Inf. Process. Syst.*, 16, 2004. [71](#)
- [212] J. Weickert. Anisotropic diffusion in image processing. *PhD thesis, University of Kaiserslautern, Germany*, 2006. [84](#), [87](#)

-
- [213] H. Wendt and P. Abry. Multifractality tests using bootstrapped wavelet leaders. *IEEE Transactions on Signal Processing*, 55(10), 2007. [4](#)
- [214] R. W. Wilson. Slodar: measuring optical turbulence altitude with a shack-hartmann wavefront sensor. *MNRAS*, 337:103–108, 2002. [12](#)
- [215] A. Witkin. Scale-space filtering, 1983. Proc. IJCAI, Karlsruhe, West Germany. [70](#)
- [216] H. Yahia, J. Sudre, V. Garçon, and C. Pottier. High-resolution ocean dynamics from microcanonical formulations in non linear complex signal analysis. *AGU FALL MEETING, San Francisco*, 2011. [126](#)
- [217] H. Yahia, J. Sudre, C. Pottier, and V. Garçon. Motion analysis in oceanographic satellite images using multiscale methods and the energy cascade. *Pattern Recognition*, 43(10):3591–3604, 2010. [3](#), [55](#), [62](#), [70](#), [71](#), [106](#), [126](#)
- [218] A. Yuille and T. Poggio. Fingerprints theorems for zero crossings. *J. Opt. Soc. Am. A*, 2(5):683–692, 1985. [83](#)
- [219] A. L. Yuille and T. A. Poggio. Scaling theorems for zero crossings. *IEEE Trans. Pattern Anal. and Mach. Intelligence*, 8(1):15–25, 1986. [69](#)
- [220] F. Zamkotsian, H. Camon, N. Fabre, V. Conedera, and G. Moreaux. Micro-deformable mirror for next generation adaptive optical systems. *Adaptive Optical System Technologies II, Proc. of SPIE*, 4839:711–720, 2003. [27](#)
- [221] Y. Zeevi and D. Rotem. Image reconstruction from zero crossings. *IEEE Trans. Acoust., Speech, Signal Processing*, 34:1269–1277, 1986. [83](#)
- [222] X. X. Zhu and R. Bamler. Super-resolution for 4-d sar tomography via compressive sensing. *8th European Conference on Synthetic Aperture Radar, Aachen, Germany (EUSAR)*, 2010. [1](#)

-
- [223] S. W. Zucker and R. A. Hummel. A three-dimensional edge operator. *IEEE Trans. Pattern Anal. and Mach. Intelligence*, 3(3):324–331, 1981.